AN IMAGE-BASED ANALYSIS OF STRATIFIED NATURAL GAS COMBUSTION IN A CONSTANT VOLUME BOMB

by

ANDREW MEZO

B.A.Sc., The University of British Columbia, 2006

A THESIS SUBMITTED IN PARTIAL FULFILLMENT OF
THE REQUIREMENTS FOR THE DEGREE OF

MASTER OF APPLIED SCIENCE

in

THE FACULTY OF GRADUATE STUDIES

(Mechanical Engineering)

THE UNIVERSITY OF BRITISH COLUMBIA

(Vancouver)

September 2008

ABSTRACT

Current stoichiometric spark-ignited engine technologies require costly catalytic converters for reductions in tailpipe emissions. Load control is achieved by using a throttle, which is a leading contributor to reductions in efficiency. Spark-ignited lean burn natural gas engines have been proven to be more efficient and emit fewer pollutants than their stoichiometric counterparts. Load reduction in these engines can be achieved by regulating the air/fuel ratio of the intake charge thereby reducing the efficiency penalties inherent to throttling.

Partially stratified charge (PSC) can provide further reductions in emissions and improvements in efficiency by extending the lean limit of operation. PSC is achieved by the ignition of a small quantity of natural gas in the vicinity of the spark plug. This creates an easily ignitable mixture at the spark plug electrodes, thereby providing a high energy ignition source for the ultra-lean bulk charge.

Stratified charge engine operation using direct injection (DI) has been proposed as a method of bridging the throttleless load reduction gap between idle and ultra-lean conditions. A previous study was conducted to determine if PSC can provide a high-energy ignition source in a direct injected stratified charge engine. Difficulties with igniting the PSC injections in an air-only bulk charge were encountered.

This study focuses on a fundamental Schlieren image-based analysis of PSC combustion. Natural gas was injected through a modified spark plug located in an optically accessible combustion bomb. The relationships between PSC injection timing, fuel supply pressure and spark timing were investigated. Spark timing is defined as the duration between commanded start of injection and the time of spark. As the fuel supply pressure was increased, the minimum spark timing that lead to successful combustion also increased. The largest spark timing window that led to successful combustion was determined to be 80 ms wide at an injection fuel supply pressure of 300 psi. The amount of unburned natural gas increased with increasing spark timing.

A cold flow study of the PSC injection system was also conducted. The PSC injection solenoid was found to have a consistent average injection delay of 1.95 ms. The slope of the linear response region of observed injection duration to commanded injection duration was 8.4. Due to plenum effects, the average observed injection duration of the entire PSC system was an order of magnitude longer than the commanded injection duration and was found to vary significantly with fuel supply pressure.

TABLE OF CONTENTS

LIST OF TABLES

LIST OF FIGURES

NOMENCLATURE

SYMBOLS

P_{RATIO}	Injection Pressure Ratio
$\%P_{MPI}$	Percent of Mean Post Injection Pressure
B	Uncertainty Due to Instrumentation Error
$CI_{95\%}$	95% Confidence Interval
c	Speed of Light in Vacuum (3.0×10^8 m/s)
c_0	Speed of Light in a Medium of Interest
i_{dur}	Injection Duration
i_{end}	Injection End
i_{start}	Injection Start
k	Gladstone-Dale Coefficient
m_{NG}	mass of injected natural gas
m_{NG}	Mass of Natural Gas Injected
n	Refractive Index
P	Uncertainty Due to Averaging of Individual Realizations
p	Instantaneous Pressure
P_{air}	Pressure of Air
P_{NG}	Pressure of Natural Gas
Q_{hr}	Gross Heat Release
Q_{ht}	Transferred Heat
Q_{net}	Net Heat Release
R_{NG}	Gas Constant for Natural Gas
S_x	Standard Deviation
T	Temperature
$t_{0.25, n-1}$	Two-tailed 95% Confidence Interval Parameter in Student's t-table
t_{comb}	Combustion Duration
t_{ign}	Ignition Delay
T_S	Spark Timing
v	Instantaneous Volume
V_{bomb}	Volume of Combustion Bomb
$\overline{X}$	Average
w_i	Combined Uncertainty for Measured Parameters
W_R	Overall Uncertainty for Calculated Parameter
Z	Mass Fraction
η_{th}	Thermal Efficiency

Φ	Equivalence Ratio
γ	Ratio of Specific Heats
ρ	Density
ζ	Mixture Fraction

ABBREVIATIONS

BC	British Columbia
BTDC	Before Top Dead Centre
CAD	Crank Angle Degrees
CID	Commanded Injection Duration
CSOI	Commanded Start of Injection
FFT	Fast Fourier Transform
GDI	Gasoline Direct Injection
HC	Homogeneous Charge
HHR	Heat Release Rate
ICE	Internal Combustion Engine
IHR	Integrated Heat Release
$IHR_{95\%}$	Combustion Duration
LLC	Lean Limit of Combustion
NG	Natural Gas
OSID	Observed Solenoid Injection Duration
PIV	Particle Image Velocimetry
PLIF	Planar Laser Induced Fluorescence
PSC	Partially Stratified Charge
RAFR	Relative Air-Fuel Ratio
RON	Research Octane Number
UBC	The University of British Columbia

ACKNOWLEDGEMENTS

I would like to thank my supervisors, Dr. Bob Evans and Dr. Martin Davy for the guidance and support they have given me during my studies at UBC. I am thankful to David Gorby for his mentorship during my first weeks at CERC and for the valuable information he has given me even after his departure.

I am grateful to Malcolm Shield for the insightful research conversations during work and play, to James Saunders for being a great neighbour and Ed Chan for all the helpful bits of information and code.

I thank the people and staff at UBC Mechanical Engineering for their help and contributions. I would like to recognize Glen Jolly for sharing his vast electronics and controls knowledge with me.

I'd also like to thank all my colleagues at Coanda for the support and warm wishes all throughout my graduate school.

I am grateful to my parents, who have encouraged me to take this path and have offered their continuous support throughout.

Lastly, I would like to thank my girlfriend Julie, who has stood by me and encouraged me throughout my studies here.

1. INTRODUCTION

The internal combustion engine (ICE), which dates back to the late 19th century, is still the prime mover in today's transportation industry. Over the course of its lifetime, the ICE has had numerous improvements in every aspect ranging from size, durability, control, and tailpipe emissions. In the last 50 years of operation, some great strides have been made in the field of engine control and management, which have made the internal combustion engine cleaner and more efficient. Also, alternative fuels such as natural gas have become more popular due to their abundance and clean burning nature.

1.1 BACKGROUND

The recent introduction of carbon taxation, increases in the price of oil, as well as continuously tightening emissions regulations, have motivated further research into clean burning, efficient engine technologies. Spark ignited engine research at the University of British Columbia (UBC) is primarily focused on natural gas (NG) fuelling. NG is an abundant fuel source in BC, consisting mainly of methane (>90% CH_4) [Terasen 2008]. The application of natural gas in a spark ignited ICE is attractive due to its high hydrogen to carbon ratio, as well as its relatively high research octane number (RON > 130) compared to gasoline. The increased H/C ratio helps reduce CO_2 emissions by as much as 30% in comparison to long chain hydrocarbon liquid fuels such as Diesel and gasoline [Pischinger 2003]. The increased RON of NG over that of gasoline reduces engine knock, and allows engine operation at higher compression ratios in homogeneous charge fuelling. The price of natural gas is also advantageous over that of gasoline, equalling about half the cost of gasoline on a kilowatt-hour basis [Pischinger 2003].

The majority of today's spark ignited engines used for transport operate on stoichiometric, homogeneous air-fuel mixtures. Stoichiometric engines require three way catalytic converters to reduce emissions

levels below those imposed by legislation. Since three way catalytic converters require stoichiometric combustion for efficient operation, air/fuel charge throttling must be used for load control. Pumping losses inherent to throttling are a major contributor to the decreased brake thermal efficiency (η_{th}) of spark ignited engines at part load [Heywood, 1988].

The lean burn approach has been shown as an effective method of load control and NO_X emissions reduction [Reynolds, 2001]. There are several other advantages inherent to lean burn operation, which include increased thermal efficiency and reduction in emissions of hydrocarbons (HC), and carbon monoxide (CO). The work of Reynolds demonstrates that load reduction can be easily achieved in the upper load range by leaning the overall air/fuel ratio rather than throttling. Reynolds demonstrated that further load control is possible by using a partially stratified charge (PSC) [Evans 2000] to extend the lean operating envelope of a single cylinder engine (UBC Ricardo Hydra). Reynolds extended the Ricardo Hydra load range an additional 10% beyond that attainable by conventional lean operation. PSC extends the lean limit of operation by injecting a small quantity of fuel in the vicinity of the spark plug electrodes, thereby ensuring that there is a near-stoichiometric air-fuel ratio near the electrodes at the time of spark. This is assumed to provide a high-energy ignition source for the ultra-lean bulk charge which is otherwise not ignitable by conventional spark. Although a step in the right direction, a throttleless load reduction gap still exists between ultra-lean and idle conditions, thus further load control using overall air/fuel ratio is desired.

Previous research efforts on the development of a throttleless natural gas engine by Kubesh (2001), developed a prechamber engine design that successfully extended the lean limit of operation to near-idling conditions. Although Kubesh showed increases in thermal efficiency compared to the stoichiometric homogeneous charge engine, the increases were minimal due to the large heat and combustion losses inherent to prechamber design engines. Kubesh also attempted to use a direct injected, split bowl-in-piston combustion chamber configuration as an alternative to the prechamber design. The

split bowl-in-piston design had poor operating and emissions characteristics and was deemed unfeasible with the gaseous direct injector technology of that time.

The introduction of a more robust and faster acting series of direct injectors by Westport Innovations allowed Gorby (2007) to implement direct injection of NG in the UBC Ricardo Hydra engine. The work conducted by Gorby was focused on extending the lean operating envelope of the Ricardo Hydra to near-idle conditions, by using direct injection in conjunction with PSC. Although PSC operation was shown to be effective in ultra-lean air fuel ratio environments, Gorby found the PSC plume difficult to ignite in an air only background. Without ignition of the PSC pilot charge, the main fuel jet provided by the Westport injector did not ignite either. An air only background is necessary for a fully stratified charge operation capable of near-idle throttleless operation. The equivalence ratios ($\Phi = 1/\lambda$) required for throttleless operation of the 8.1 L CNG engine used by Kubesh, are shown in **Figure 1**. For a torque output of less

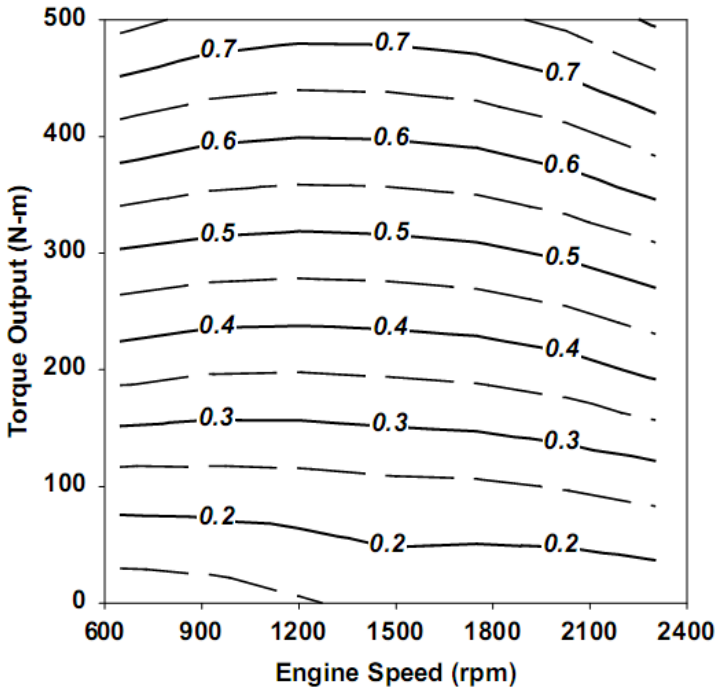

Figure 1 - Fuel-Air Equivalence Ratios Required for Throttleless Operation from [Kubesh, 2001]

than 50 N-m (<10% max torque), an equivalence ratio of less than 0.1 ($\lambda > 10$) is required. The lean limit of operation for a homogeneous charge natural gas engine was shown to be around $\Phi = 0.60$ ($\lambda = 1.66$).

Gorby's inability to ignite the PSC pilot charge in an air only environment suggested that a better understanding of the PSC injection system timing and flow characteristics was necessary before moving forward with further engine testing. To this end, a study of gaseous reacting jets is essential to elucidate the limits of the PSC ignition, and design viable control schemes to operate low-NO_X lean burn NG spark ignition engines using PSC and direct fuel injection.

1.2 TURBULENT TRANSIENT JETS

The injection of the PSC fuel charge is assumed to be turbulent, based on findings presented by Hill and Oulette (1999) on transient turbulent gaseous jets. There are several fundamental characteristics which make the spark ignition of turbulent jets very difficult. Turbulent jet imaging performed by Lahbabi (1993) indicates that the instantaneous jet profile is very different from the averaged one. This finding was also discussed by Oulette (1996), who researched direct injections of natural gas for Diesel engine fuelling. Studies conducted by the present author also show the transient turbulent jet to vary significantly in profile from an individual realization to a run-averaged result. **Figure 2** demonstrates the difference between the instantaneous jet profile and a three run averaged profile for a water jet of Reynolds number of 110,000.

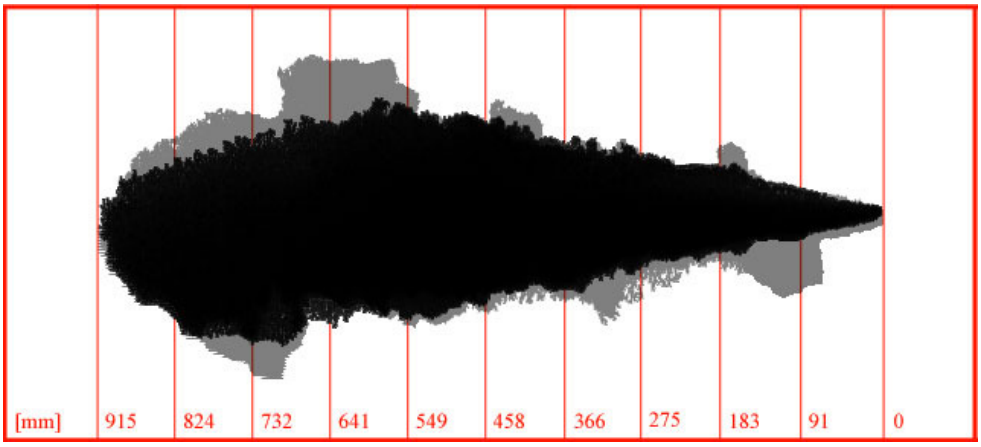

Figure 2 - Individual Realization Overlapped with Three Run Average for Turbulent Transient Jet

Research performed by Dahm and Dimotakis (1988) on turbulent transient jet mixing has shown that concentration gradients also vary between individual realizations and run-averages. Dahm and Dimotakis found the concentration gradients of the instantaneous profile to be very large, while those of the averaged jet were found to be well approximated by a smooth probability density function. Since the concentration gradients of the instantaneous transient jet are very steep, and vary with each individual realization, spark ignition at the correct air-fuel ratio can be very challenging.

The design of the jet exit nozzle was found by Mi *et al.* (2001) to greatly influence the mixing rate of the fuel with the surrounding air. Mi *et al.* determined that the mixing entrained by an orifice type jet to be superior to that of pipe and smooth contraction jets. Dahm and Dimotakis found the external fluid entrainment to also be highly Reynolds number dependent. In the case of the PSC injector, Reynolds number varies with pressure ratio. Thus, any fluctuations in pressure upstream of the metering solenoid can dramatically alter the flammability of the PSC charge.

1.3 SCHLIEREN VISUALIZATION

A method of visualizing the PSC plume was deemed necessary in order to gain a better understanding of the flow characteristics at several pressure ratios. The Schlieren visualization technique was chosen for viewing the PSC fuel injections due to its simplicity of operation and availability within the department. An optically accessible combustion bomb was outfitted with the PSC injection system, where the other instrumentation described in detail in the next chapter.

Schlieren visualization works on the basic principle that the refractive index (n) of gases is dependent on their molecular composition and density. The refractive index of a medium is defined as the ratio of the speed of light through that medium (c_0) to the speed of light in vacuum (c). As the speed of light in vacuum is constant (3.0×10^8 m/s), the refractive index of a gas is directly proportional to the speed of light within this gas. Thus, the refractive index of a gas is proportional to its density according to Equation 1.1, where k is the Gladstone-Dale coefficient which is gas specific, and ρ is the gas density.

$$n - 1 = k\rho \qquad \text{(Eq. 1.1)}$$

The value of k varies according to the molecular composition of the gas, and the wavelength of the Schlieren light source. Since the value of k decreases with increasing light wavelength, a mercury vapour Schlieren light source was selected due to the strong bias towards the ultraviolet range of the mercury emission spectrum [Settles, 2001]. It is important to note that gas composition inhomogeneities bend the light in proportion to the gradient of the refractive index; thus, only sections of the bomb with varying air-fuel composition or varying density will be visible. Equation 1.2 taken from Settles (2001), gives the angular ray deflection in the x-y plane along the direction of the optical axis, z. Therefore, according to Equation 1.2, the luminosity of a Schlieren image corresponds to the first spatial derivative of the refractive index.

$$\varepsilon_x = \frac{1}{n}\int \frac{\partial n}{\partial x}\partial z, \qquad \varepsilon_y = \frac{1}{n}\int \frac{\partial n}{\partial y}\partial z \qquad \text{(Eq. 1.2)}$$

Schlieren images can be generated using various configurations of mirrors, lenses or combinations of the two. Regardless of the selected arrangement, a knife edge is required at the point where the light is focused into the camera. The knife edge is needed in order to block some of the refracted rays from entering the camera and obscuring the density gradients. By blocking half the refracted light rays, the first order spatial derivatives of the refractive index become visible. This behaviour is demonstrated in the simplified diagram shown in **Figure 3**.

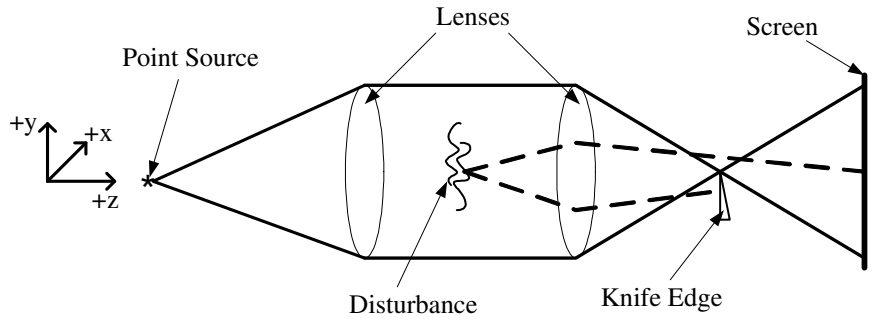

Figure 3 - Simple Schlieren System Diagram, Adapted from Settles (2001)

Omitting to use the knife edge shown, all the refracted rays are displayed on the screen and the first order spatial derivative in refractive index becomes invisible. The visualization method that does not use a knife edge is called Shadowgraphy, and it is only capable of displaying second order spatial derivatives in refractive index.

The Schlieren configuration used in these experiments is a Z-Type Herschellian system consisting of a condenser lens and two parabolic mirrors. This setup if further discussed in Section 2.1.

1.4 RESEARCH OBJECTIVES

The objectives of the research presented in this thesis are to determine the range of pressure ratios and spark timings that lead to successful combustion of the PSC fuel charge in an air only environment. The experiments are conducted in a fully instrumented optically accessible combustion bomb.

The Schlieren photographs collected are used to explain variations in combustion success between experimental runs, as well as to determine the PSC system injection timing parameters. The pressure data acquired is processed to give a comparison of combustion parameters between experimental runs. These combustion parameters are used to compare the combustion quality of runs at each pressure ratio and spark timing selected.

2. EXPERIMENTAL SETUP

The experimental work was conducted at the Clean Energy Research Centre at The University of British Columbia. The Schlieren optical apparatus was assembled in the UBC Ricardo Hydra single cylinder research engine test cell. The Ricardo Hydra PSC injection system was used for this study. The experimental apparatus consisted of five major components: the Schlieren optics, the high speed camera (used to capture the Schlieren images), the combustion bomb assembly, the PSC injection system and the data acquisition and triggering hardware. Each major component is described in detail in the following sections.

2.1 SCHLIEREN OPTICAL APPARATUS

The Schlieren apparatus is made up of two concave mirrors with a focal length of 8 feet, a convex lens, a mercury vapour compact arc lamp and a power supply for the lamp. Mercury vapour arc illumination was selected since it provides a luminous existence of 10-100 times that of a tungsten filament bulb and it is more sensitive to the changes in the light refraction index [Settles, 2001]. The mercury emission spectrum is biased towards the blue-green side with significant emissions proportions in the ultraviolet range. The incoherent light emitted by the mercury arc is focused by the convex lens at the focal point of the first concave mirror. This mirror collimates the light, which is then passed through the combustion bomb test section and is collected by the second concave mirror. The second mirror focuses the light back to a point, which is then projected into a 300 mm Nikkor lens mounted to the high speed camera. A sketch of the light path and Schlieren setup is shown in **Figure 4**.

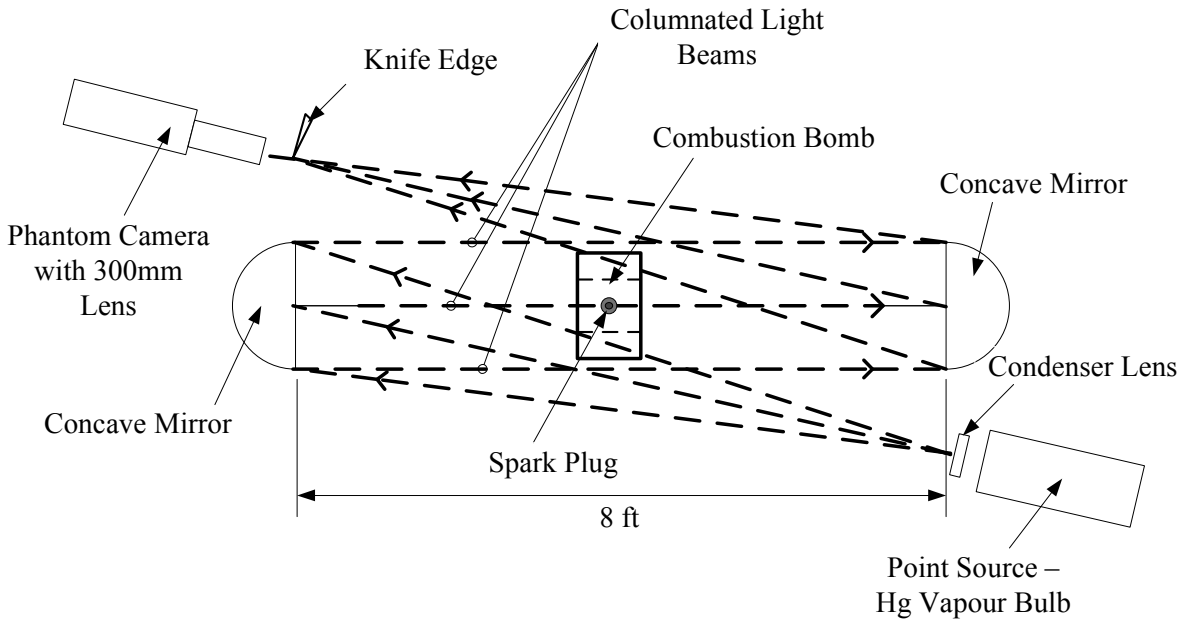

Figure 4 - Schlieren Optical Apparatus

2.2 HIGH SPEED CAMERA

The camera used to capture the Schlieren images is a 12 bit gray scale digital CCD Phantom v. 7.1, manufactured by Vision Research. Images were taken at a resolution of 480 by 480 pixels through a 300 mm Nikkor f-ratio 4.0 AF-S fixed focal length lens. At this resolution, the camera is capable of a sample rate of 9302 frames/s, with the ability to buffer 3021 images, resulting in a capture time window of 324.7 ms. The image exposure time was maintained constant at 102 μs. **Figure 5** shows a raw sample image captured with the aforementioned settings prior to any processing algorithms.

Figure 5 - Sample Raw Image Captured with Phantom Camera

2.3 COMBUSTION BOMB ASSEMBLY

The optically accessible combustion bomb is made up of a stainless steel cylinder with an 80 mm bore, sealed at each end by a disc shaped quartz viewing window 25.4 mm thick. The distance between the quartz windows is 46 mm. The measured sealed volume of the combustion bomb is 231.1 cubic centimetres. The bomb is instrumented with an Omega K-type thermocouple, an MSI calibration pressure transducer and a high speed piezoelectric transducer with a charge sensitivity of 1.083 pC/psi. An illustration of the combustion bomb assembly is shown in **Figure 6**.

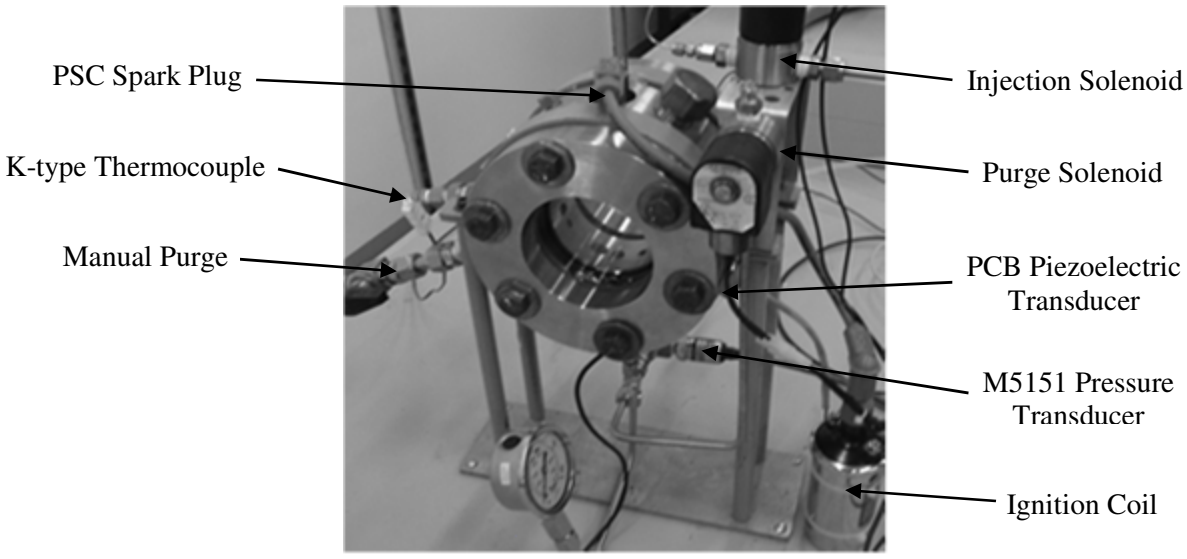

Figure 6 – Combustion Bomb Assembly

2.4 PSC INJECTION SYSTEM

The PSC concept tested in the UBC Ricardo Hydra research engine by Reynolds (2001), Brown (2003) and Gorby (2007) has been unchanged for the purposes of this study. It is intended for use in spark ignited internal combustion engines operating in a partially or fully stratified charge mode. The system consists of a modified Bosch XR2CS spark plug, an injection solenoid that meters the fuel, and a driver box to control the solenoid. The spark plug modifications necessary to achieve stratified charge are shown in **Figure 7**. A 320 mm long capillary tube with a 0.47 mm ID is connected to the outlet of the injection solenoid. High pressure natural gas is injected through the capillary tube, down the milled channel in the spark plug threads and exits through the 0.3 mm radial hole into the vicinity of the spark plug electrodes. The PSC system layout, along with tubing dimensions is shown in

Figure 8.

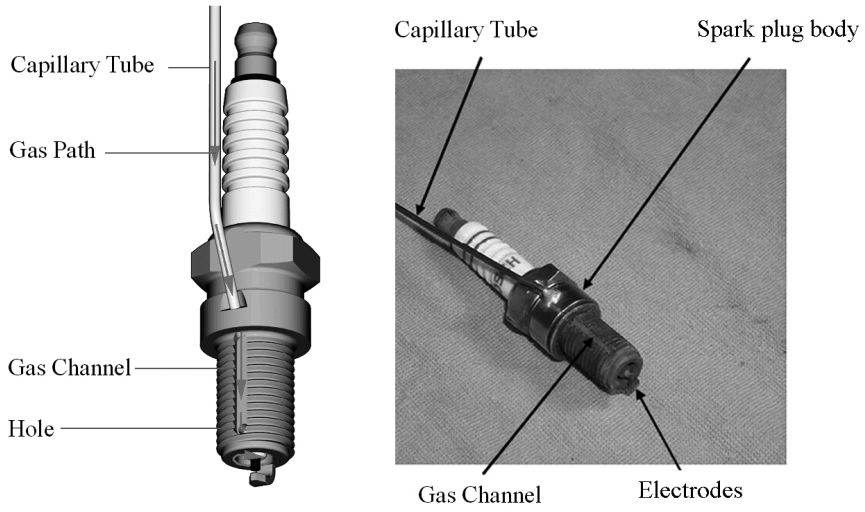

Figure 7 - Bosch XR2CS Spark Plug Modified for PSC Injection, Illustration on Left by Gorby (2007)

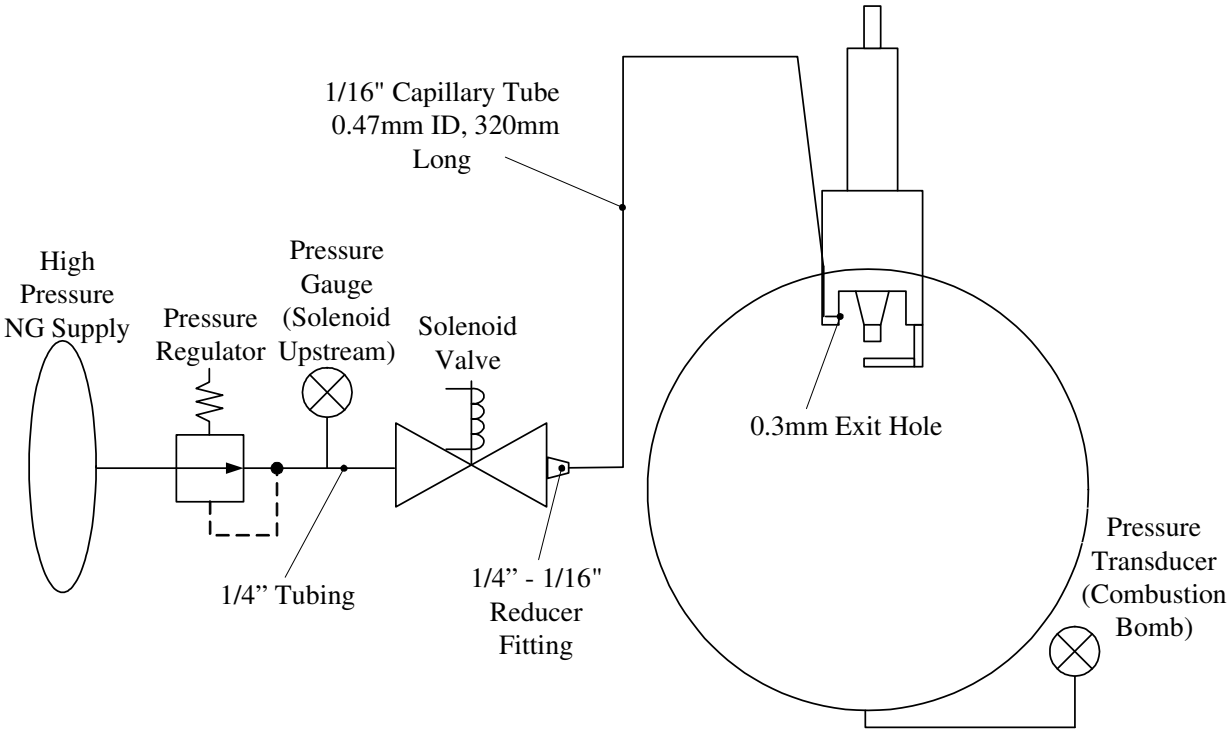

Figure 8 - PSC System Details

For the purpose of these experiments, the injection pressure ratio (P_{RATIO}) is defined as the ratio of the pressure upstream of the injection solenoid to the pressure inside the combustion bomb prior to the injection event. The pressure measurement locations are detailed in **Figure 8**. Calculations based on the theory of compressible flow in constant-area ducts with friction [Shapiro] suggest that the PSC flow remains subsonic and therefore unchoked at all pressure ratios attempted. The calculations, along with the critical capillary tube lengths required for a sonic exit condition are shown in Appendix E.

The combustion bomb was pressurized and depressurized with air five times before the start of each experiment. This procedure was followed in order to purge the natural gas remaining in the capillary tube, downstream of the injection solenoid and thus maintain consistency between runs.

2.5 DATA AQUISITION AND TRIGGERING

The data acquisition and triggering hardware was linked to a computer running NI LabView software V.7.0. The hardware used for triggering the high speed camera, injector driver box and spark discharge was a 47 channel PCI National Instruments data acquisition card. An NI PCI-6601 20 MHz timer card was used to for the high speed timing required in these experiments. High speed pressure data was collected at a frequency of 50 kHz with an NI USB-9211 data acquisition card. Temperature data was collected with an NI USB-9215 thermocouple card. A separate voltage channel was used in the high speed data acquisition hardware to synchronize the triggering hardware.

The LabView software collected pressure and temperature data as tab separated text. This data was pegged, zeroed and analysed with Mathworks Matlab. The high speed image data from the Phantom camera was downloaded from the camera buffer and saved in raw video format. These videos were later

converted to 16 bit grayscale TIFF images which were further processed with Matlab. A screen shot of the LabView control interface is included in **Figure 9**.

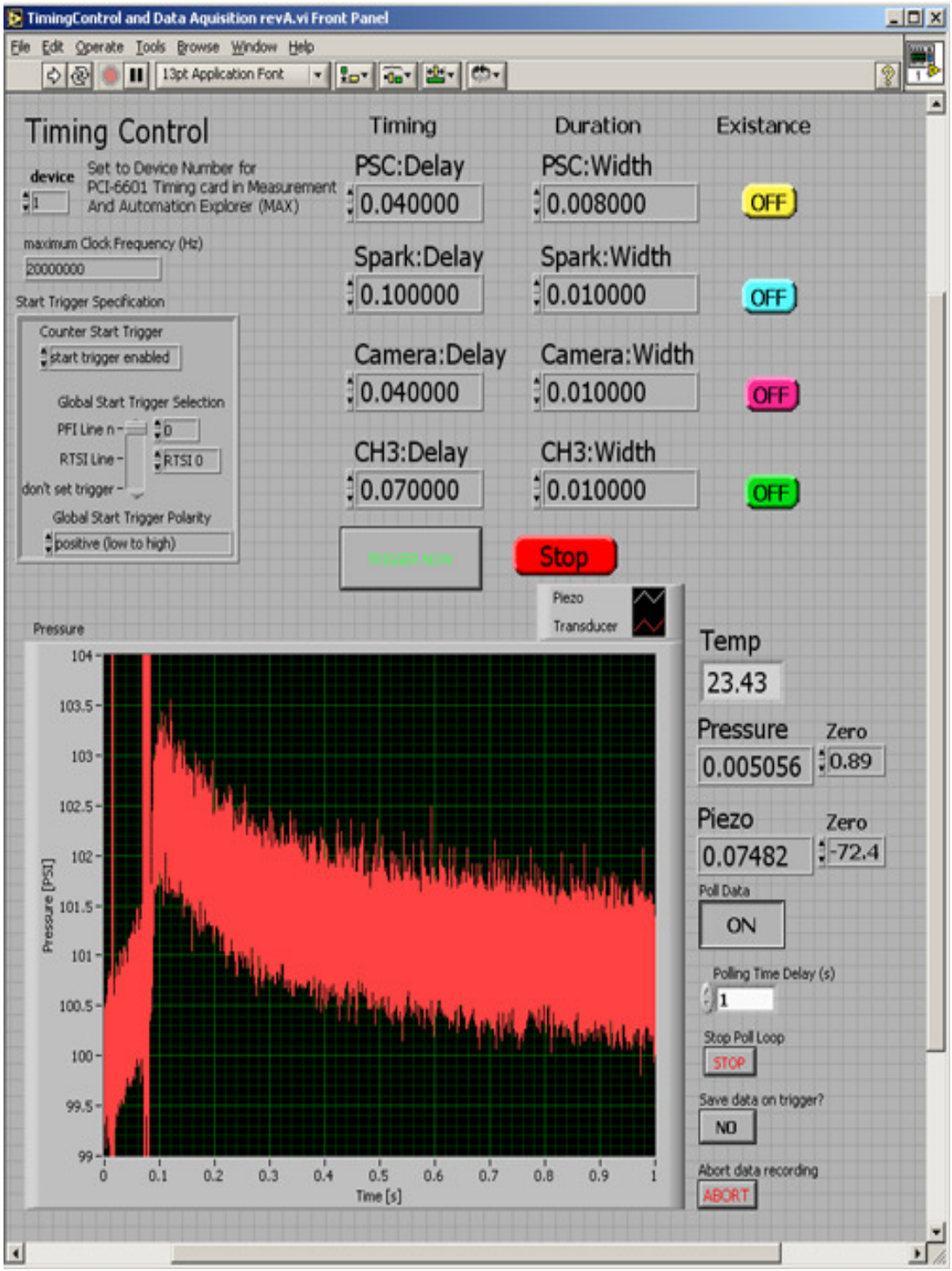

Figure 9 - LabView Virtual Interface (.vi) Control Software Screen Output

2.6 INJECTION SOLENOID DELAY STUDY

In order to determine the injection timing characteristics of the PSC system, an injection solenoid timing study was necessary to characterize the PSC solenoid on a stand-alone basis. The PSC capillary tube was disconnected from the solenoid body, thus leaving the 0.25" port hole exposed to the atmosphere. By using high-speed Schlieren photography, the natural gas transient jet was visualized exiting the solenoid body at a frame rate of 4700 frames/s.

This study was performed under atmospheric conditions, at constant regulator pressure and with several commanded injection duration (CID) values. In each of the 24 runs conducted, a transient gaseous jet as defined by Hill and Ouellette (1999) is clearly observed at the solenoid exit. Injection solenoid delay is defined as the duration between the commanded start of injection (CSOI) and the first instance natural gas is observed exiting the solenoid. The observed end of injection is defined as the duration between the CSOI and the time at which the transient jet plume detaches from the solenoid exit. The duration between the observed start and observed end of injection is defined as the observed solenoid injection duration (OSID).

An example of the start, development, and end of the transient jet is shown in **Figure 10**. The 1.819 ms slide depicts the observed start of injection while the 14.584 ms slide shows the observed end of injection.

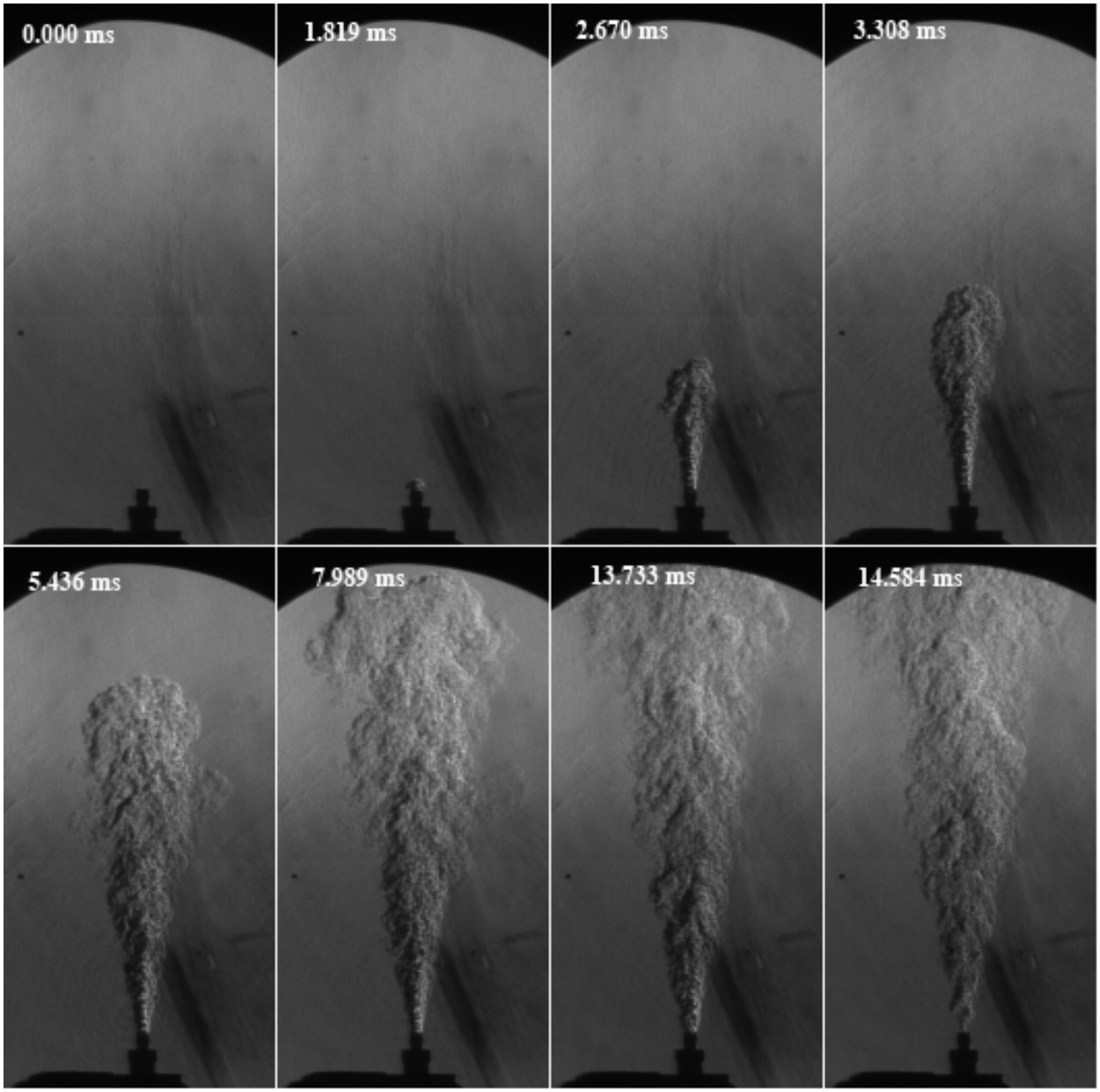

Figure 10 - Image Compilation, Solenoid Timing Study, 21.312 ms Commanded Pulse Width

The commanded injection pulse width was varied between 0.666 ms and 21.312 ms. These pulse width values correspond to 8 crank angle degrees (CAD) and 256 CAD respectively, in an ICE operating at 2000 rpm. The injection pressure was maintained at a constant 29 bar (420 psi). **Figure 11** shows the injection solenoid delay as a function of commanded injection duration. The error bars specify a 95% confidence interval (defined in Section 3.4), which indicate that all values are within experimental error

and average a jet plume start delay of 1.95 ms (23.5 CAD at 2000 rpm). The start delay is concluded to be independent of commanded injection duration.

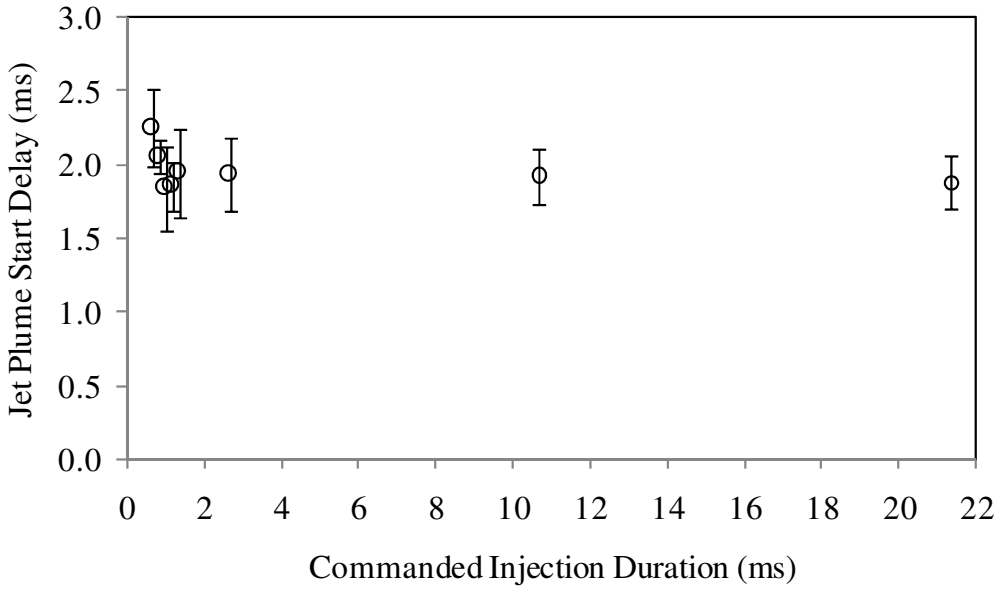

Figure 11 – Injection Solenoid Delay for Various Commanded Pulse Width

The observed solenoid injection duration is plotted against commanded injection duration in **Figure 12**. The response of the OSID is linear with CID for CID values up to ~ 2.7 ms. For CID values higher than 2.7 ms, the observed solenoid injection duration becomes constant within experimental error (12.5 ms). Since the observed solenoid injection duration is expected to increase linearly with commanded injection duration, a deviation from this behaviour could mean that the control system is not allowing for CID values higher than 2.7 ms.

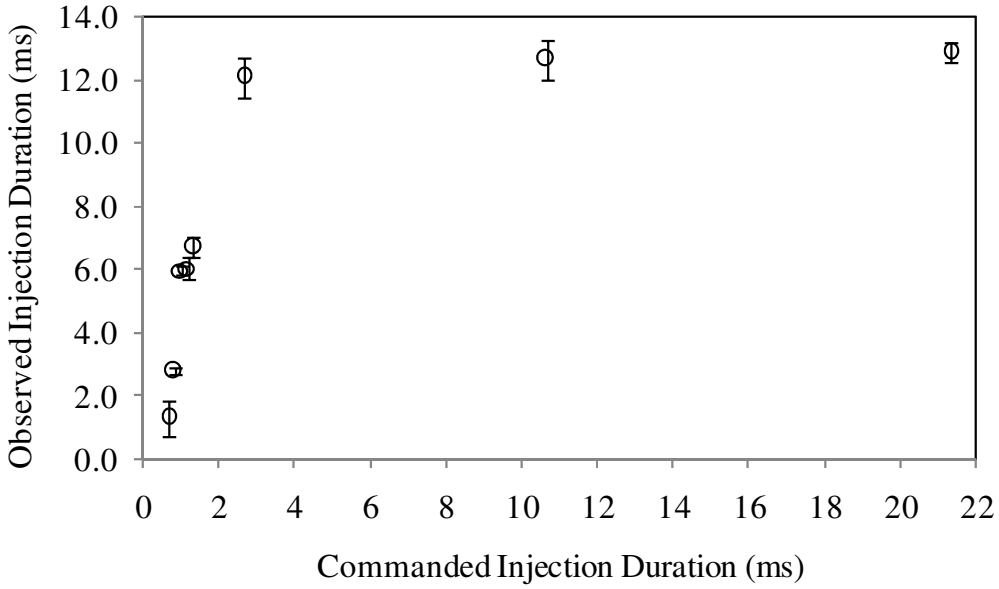

Figure 12 - Observed Solenoid Injection Duration vs. Commanded Injection Duration

The linear region of **Figure 12** is re-plotted in **Figure 13** with trendline and R^2 values shown. The intercept of the trendline suggests that CID values less than ~ 0.46 ms result in no observed injection at

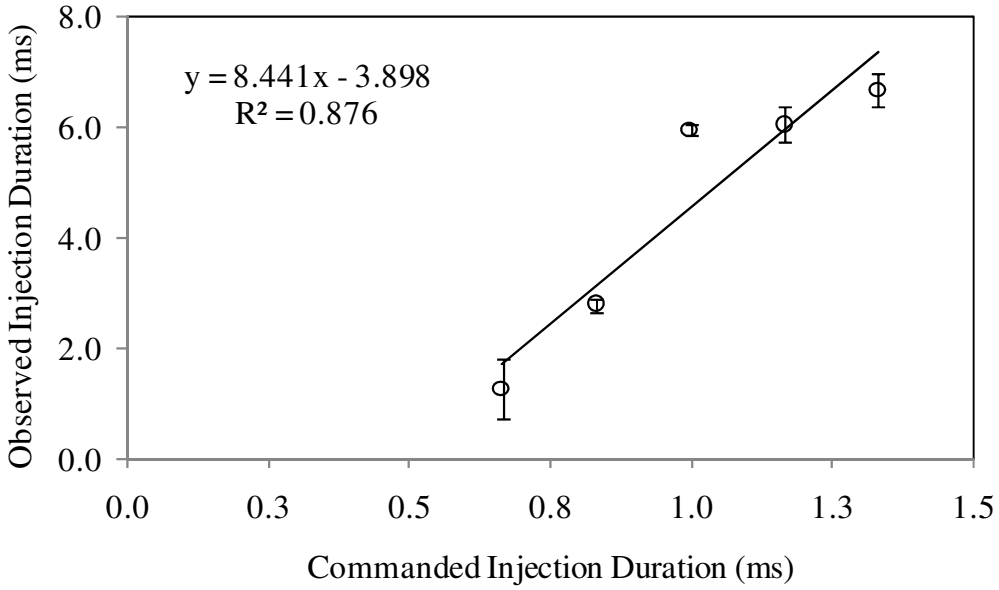

Figure 13 - Linear Region of OSID vs. CID Plot

all. The trendline slope indicates that observed injection durations are significantly longer than commanded injection durations. Both the trendline slope, which is much greater than one and the CID axis intercept indicate that the solenoid valve has significant delays due to inertial forces. This is a strong sign that observed PSC system injection durations will likely be much longer than the commanded injection durations. Also, as the capillary tube is connected for the PSC injections, plenum effects due to the pressurized system volume downstream of the solenoid exit will likely extend the observed injection duration even further.

Evidence of solenoid chatter was observed for three commanded injection duration timings. At CID values of 1.000, 1.167, and 1.332 ms a secondary jet pulse is observed following the main jet pulse. The secondary pulse observed is shorter in duration and smaller in size. An example of this behaviour at CID = 1.00 ms is shown in **Figure 14**, where the progression of the secondary jet pulse is clearly seen following the end of the primary jet pulse. Since this chatter could introduce additional uncertainties in the PSC injection system, CID timings that cause solenoid chatter were avoided in later studies.

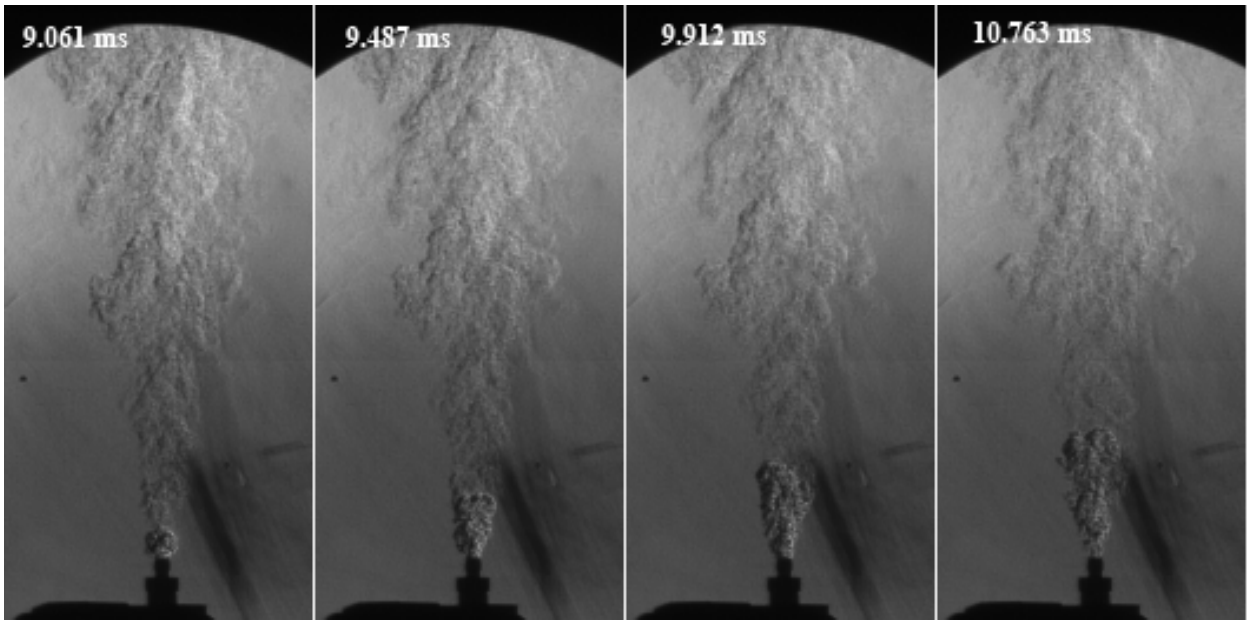

Figure 14 - Solenoid Chatter Depicted by Secondary Jet Pulse, CID = 1.00 ms

3. METHODOLOGY

An investigation into the flammability of the PSC pilot charge in an air only environment was performed using a Schlieren image analysis technique for qualitative combustion observation. For cases where combustion was present, visualization helped to determine the combustion quality by the amount of unburned gases remaining post-combustion. The Schlieren images gave significant insight into the amount of mixture present near the spark plug electrodes at the time of spark. The high speed images were also useful in determining the PSC system delays and injection durations at the pressure ratios studied.

High speed pressure data was used to determine combustion parameters such as ignition delay, combustion duration, rate of heat release and total heat release for all combusting cases. Cold flow pressure data was used to establish the amount of natural gas injected at each pressure ratio. Pressure data was also used to validate the findings and conclusions derived from the Schlieren images.

3.1 EXPERIMENTAL MATRIX

Previous studies of the PSC system conducted by Reynolds (2001) suggest that spark timing with respect to injection is a critical variable when tuning the PSC system for optimal operation. Spark timing with respect to the commanded start of injection was also shown to affect parameters such as combustion duration, ignition delay and amount of heat released [Huang *et al.*, 2003]. For the purposes of this study, spark timing (T_S) is defined as the duration between the commanded start of injection (CSOI) and the commanded time of spark. Work performed on stratified methane mixtures in a constant volume combustion bomb by Kitagawa *et al.* (2002) demonstrates a significant influence of spark timing on maximum combustion pressure and mass fraction of fuel burned. Kitagawa *et al.* have also shown the rate of pressure rise to be greatly affected by spark timing.

Mass of fuel injected, exit momentum flux and the Reynolds number of transient jets are all very much dependent on injection pressure ratio (P_{RATIO}) [Hill, 1999]. These transient jet characteristics were shown to greatly influence entrainment velocities and concentration gradients by Dahm and Dimotakis (1990). Pressure ratio is defined as the ratio of the injection pressure upstream of the solenoid to the initial pressure in the combustion bomb. Although the injection pressure ratio was held constant in the studies performed by Reynolds, Brown and Gorby, it was deemed critical to learn how the injection pressure ratio affects the combustion quality and stability of the PSC charge.

The previous section suggests that commanded injection duration timings greater than 2.7 ms result in constant OSID values. Also, at commanded injection durations less than 1.3 ms solenoid chatter was observed. Thus, for the purpose of these experiments, the commanded injection duration was maintained at a constant value of 8.0 ms.

As described previously, Reynolds (2001) and Brown (2003) have shown successful application of PSC to an ICE operating in a partially stratified mode with bulk charge relative air fuel ratios of 1.3 to 1.7. Gorby (2007) attempted to operate the Ricardo Hydra in a fully stratified mode, with a bulk charge of pure air. He was unsuccessful and did not manage to ignite the pilot PSC charge. There is much interest in the application of the PSC system to a fully stratified charge engine. Consequently, all tests conducted for this study were performed with an air only bulk charge. The charge pressure was determined to replicate that of the Ricardo Hydra engine at 30 degrees before top dead centre (BTDC). A summary of the experimental matrix conducted is shown in **Table 1**. A minimum of three repeats were performed for each table entry. The list of the experimental numbers and order of execution is given in Appendix A.

Table 1 - Experimental Matrix

Injection Pressure Ratio (P_{RATIO})	Spark Timing, (T_S) [ms]												
2	10	20	30	40	50	60	70	80	90	100	-	-	-
3	10	20	30	40	50	60	70	80	90	100	120	140	160
4	10	20	30	40	50	60	70	80	90	100	120	140	160

Constants:
Charge pressure: 100 psi (6.89) bar
Commanded injection duration: 8.000 ms

3.2 PRESSURE DATA ANALYSIS

Raw pressure data was collected at a frequency of 50 kHz for 500 ms per experiment. Since the piezoelectric pressure transducer is dynamic, a secondary pressure transducer was used to peg the piezoelectric pressure signal to the correct initial value. The pressure data timing was zeroed and synchronized according to the input trigger signal of the camera.

A fast Fourier transform (FFT) algorithm was applied to the raw pressure signal to remove high frequency noise. The pressure signal was then differentiated and heat release rate (HRR) was calculated according to Equation 3.1 [Heywood].

$$\frac{dQ}{dt} = \frac{\gamma}{\gamma - 1} P \frac{dV}{dt} + \frac{1}{\gamma - 1} V \frac{dP}{dt} \qquad \text{(Eq. 3.1)}$$

Since the overall relative air-fuel ratios in the combustion bomb were ultra-lean (λ = 5.2 – 15.2) the specific heat ratio of air (γ = 1.4) was used for all combustion calculations. Net integrated heat release (IHR) values were calculated by integrating Equation 3.1. Other parameters such as ignition delay and

combustion duration were calculated from the integrated heat release data and compared for each experiment. Ignition delay (t_{ign}) is defined as the duration between the commanded time of spark and 5% IHR. Combustion duration (t_{comb}) is defined as the duration between t_{ign} and 95% IHR.

Calculations for overall relative air/fuel ratio were performed based on the partial pressures of natural gas and air. There were a total of eight cold flow natural gas injections performed for each pressure ratio. Cold flow data was used to determine the average amount of gas injected for each pressure ratio, as well as the 95% confidence interval of the pressure rise. The average cold flow pressure data of each pressure ratio was subtracted from the pressure data of the combusting experiments to determine the pressure change due solely to combustion. The NG composition used for all calculations is shown in **Table 2**. This table represents a 2005 measurement of BC gas at a nearby location (Westport Innovations), which is assumed to have a very similar composition to the UBC facilities.

Table 2 - Natural Gas Composition

Name	Species	Mole %	Mole Fraction	Molecular Mass [kg/kmol]	Lower Heating Value [KJ/kg]
Ethane	C_2H_6	6.60	0.0660	30.070	47511
Propane	C_3H_8	0.32	0.0032	44.097	46333
Methane	CH_4	91.59	0.9159	16.043	50030
Carbon Dioxide	CO_2	0.40	0.0040	44.010	0
Nitrogen	N_2	1.09	0.0109	28.013	0

Based on GC measurement, Westport Innovations, Oct 2005

3.3 IMAGE ANALYSIS

An average background image was calculated for each experiment by taking the mean of the first 50 images prior to the start of injection. The only inconsistency observed in the images used for background averaging was a very faint but noticeable light intensity variation, which can be explained by the

behaviour of the Schlieren light power source. Once an average background image was obtained, the remaining frames were then divided by the average background image to obtain a clean, noise free representation. A sample raw image and its background divided counterpart are shown in **Figure 15**.

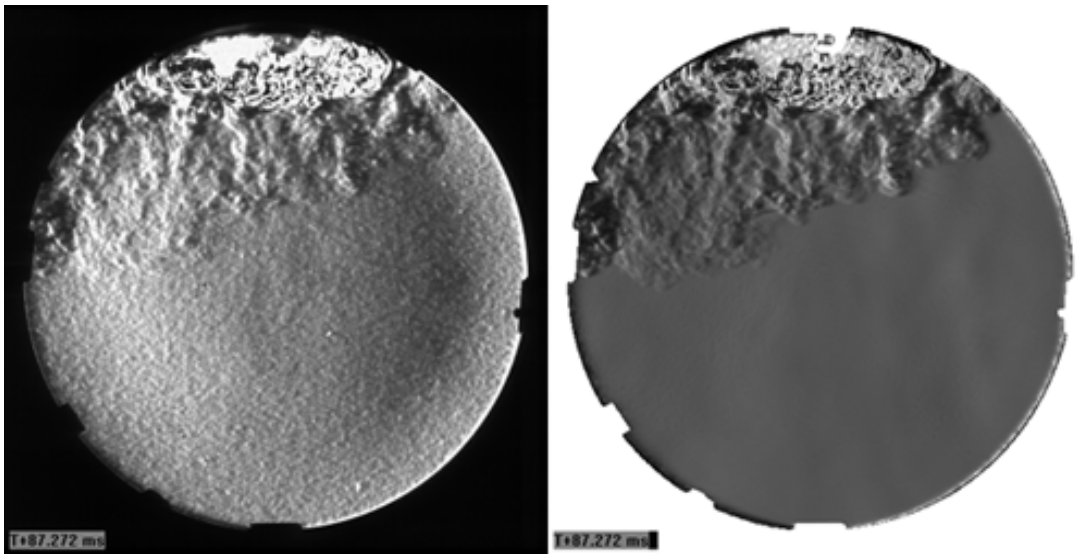

Figure 15 - Example of Raw Image and Image with Background Divided

Image binarization was required in order to perform jet and flame area calculations. An algorithm was developed to eliminate the gray background from the images represented in **Figure 15**, which is further explained in Section 4.2.5. The resulting image is shown on the left of **Figure 16**. Pixels with values below a threshold of "5000" were then assigned a value of "65535" (white) while pixels above the threshold were assigned o value of "0" (black). The binarized image is shown on the right of **Figure 16**. The threshold value of "5000" was selected after conducting a threshold sensitivity analysis outlined in Section 4.2.5. This analysis yielded consistent results in the time domain, and consistent trends in pixel area growth. Variation of the threshold value resulted in slight changes to the jet areas reported, however, trends such as jet expansion rates, injection start time, injection duration and injection finish time were all found to be consistent.

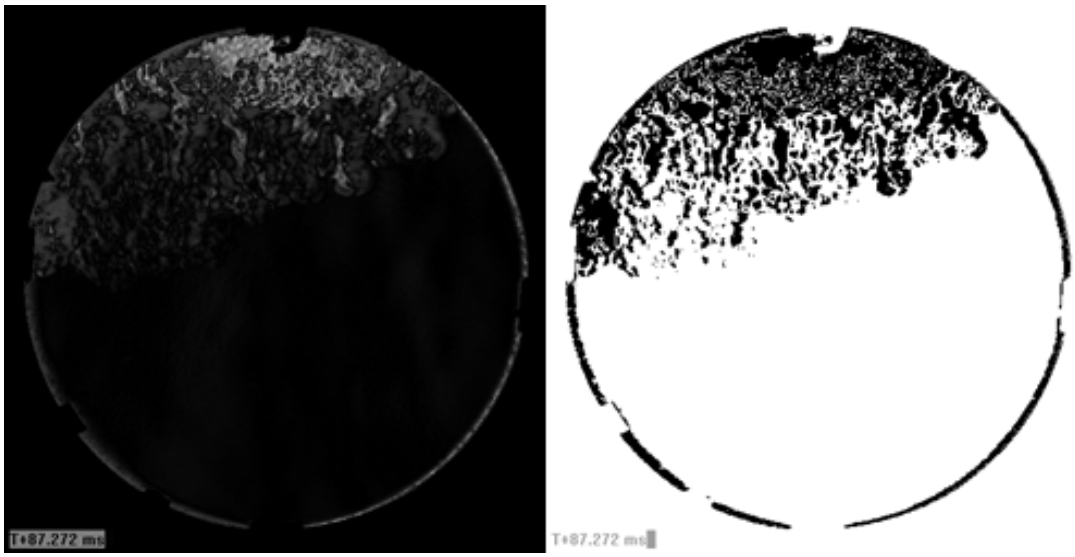

Figure 16 - Example of Background Subtraction and Binarization

3.4 UNCERTAINTY ANALYSIS

Experimental uncertainties resulting from repeats of individual realizations were calculated using a 95% confidence interval ($CI_{95\%}$) according to Equation 3.2. S_x is the standard deviation, $\overline{X}$ is the average and n the number of repeats. The corresponding value for $t_{0.25,\,n-1}$ is found in the Student's t-table.

$$CI_{95\%} = \overline{X} \pm t_{0.025,n-1}\frac{S_x}{\sqrt{n}} \qquad \text{(Eq. 3.2)}$$

Uncertainties related to instrumentation (B) were also included in the calculations, which resulted in a combined uncertainty, w_i, where w_i is specific to any measured parameter. Equation 3.3 demonstrates the calculation of w_i, which is a function of uncertainty due to instrument error and the uncertainty arising from the 95% confidence interval (P). Instrument specific error values are reported in **Table 3**.

$$w_i = \sqrt{B^2 + P^2} \qquad \text{(Eq. 3.3)}$$

Table 3 - Instrumentation Description and Uncertainty

Description	Model # / Serial #	Range	Uncertainty
MSI Pressure Transducer	M5151-000005-500PG	0 - 500 PSIG	± 0.1% FS (± 0.5 PSI)
PCB Piezoelectric Transducer	112B11 / 20877	0 - 5000 PSIG	± 0.01 PSI
Omega K-Type Thermocouple	KQXL-18	-260 - 1360 °C	2.2 °C

For a parameter of interest R, which is a function of several measured parameters (x_i) the overall uncertainty W_R is represented by Equation 3.4. W_R is a function of the combined measured parameter uncertainty (w_i) and the partial derivative of R to that of each measured parameter used.

$$W_R = \sqrt{\left(\frac{\partial R}{\partial x_1} w_1\right)^2 + \left(\frac{\partial R}{\partial x_2} w_2\right)^2 + \cdots + \left(\frac{\partial R}{\partial x_i} w_i\right)^2} \qquad \text{(Eq. 3.4)}$$

To put things into perspective, it is useful to look at an example. The mass of natural gas injected was determined based on an 8 run average for each pressure ratio, and was calculated using the ideal gas equation (Eq. 3.5).

$$m_{NG} = \frac{P_{NG} V_{bomb}}{R_{NG} T} \qquad \text{(Eq. 3.5)}$$

The uncertainty of the pressure measurement ($w_{P,NG}$) is calculated according to Equation 3.6, where $w_{ins,NG}$ is the uncertainty of the pressure transducer and $w_{exp,NG}$ is the uncertainty resulting from the 8 run 95% confidence interval.

$$w_{P,NG} = \sqrt{{w_{ins,NG}}^2 + {w_{exp,NG}}^2} \qquad \text{(Eq. 3.6)}$$

Similarly, the uncertainty of the temperature measurement (w_T) is a function of the thermocouple instrument error ($w_{ins,T}$) and the $CI_{95\%}$ uncertainty ($w_{exp,T}$) shown in Equation 3.7.

$$w_T = \sqrt{w_{ins,T}{}^2 + w_{exp,T}{}^2} \qquad \text{(Eq. 3.7)}$$

The combustion bomb volume was determined by filling with water from a burette, which has an uncertainty of w_V = 0.5 mL. Finally, the overall uncertainty for the mass of natural gas calculation is given by Equation 3.8.

$$W_{m,NG} = \sqrt{\left(\frac{V_{bomb}}{R_{NG}T} w_P\right)^2 + \left(-\frac{P_{NG}V_{bomb}}{R_{NG}T^2} w_T\right)^2 + \left(\frac{P_{NG}}{R_{NG}T} w_V\right)^2} \qquad \text{(Eq. 3.8)}$$

4. RESULTS AND DISCUSSION

The primary research objective was to determine the range of injection pressure ratios and spark timings that lead to successful combustion of stratified natural gas injections in an air-only environment. The overall air-fuel ratio for all tests was well beyond the lean limit of flammability for premixed natural gas in air. Test cases at spark timings of less than 30 ms after commanded injection were not ignitable for any pressure ratio. Test cases at spark timings above 30 ms were ignitable for some cases, where the highest frequency of successful ignition occurred at a pressure ratio of 3.

4.1 COLD FLOW INJECTION DATA

A cold flow injection study was performed with eight repeats for each pressure ratio. The commanded injection duration was the same as for the combusting experiments (8.0 ms). Pressure data acquired from this testing was used to determine the injection repeatability of the PSC system. Average overall relative air-fuel ratio (RAFR) and mass of natural gas injected (m_{NG}) were determined from this study and are reported in **Table 4**. An injection timing study was also performed based on the cold flow pressure data and is discussed in the next section. The cold flow pressure plots shown in **Figure 17** were subtracted from the pressure plots of the combusting cases, in order to determine the pressure change due solely to combustion. A value of zero in the time domain represents the start of the commanded injection (CI).

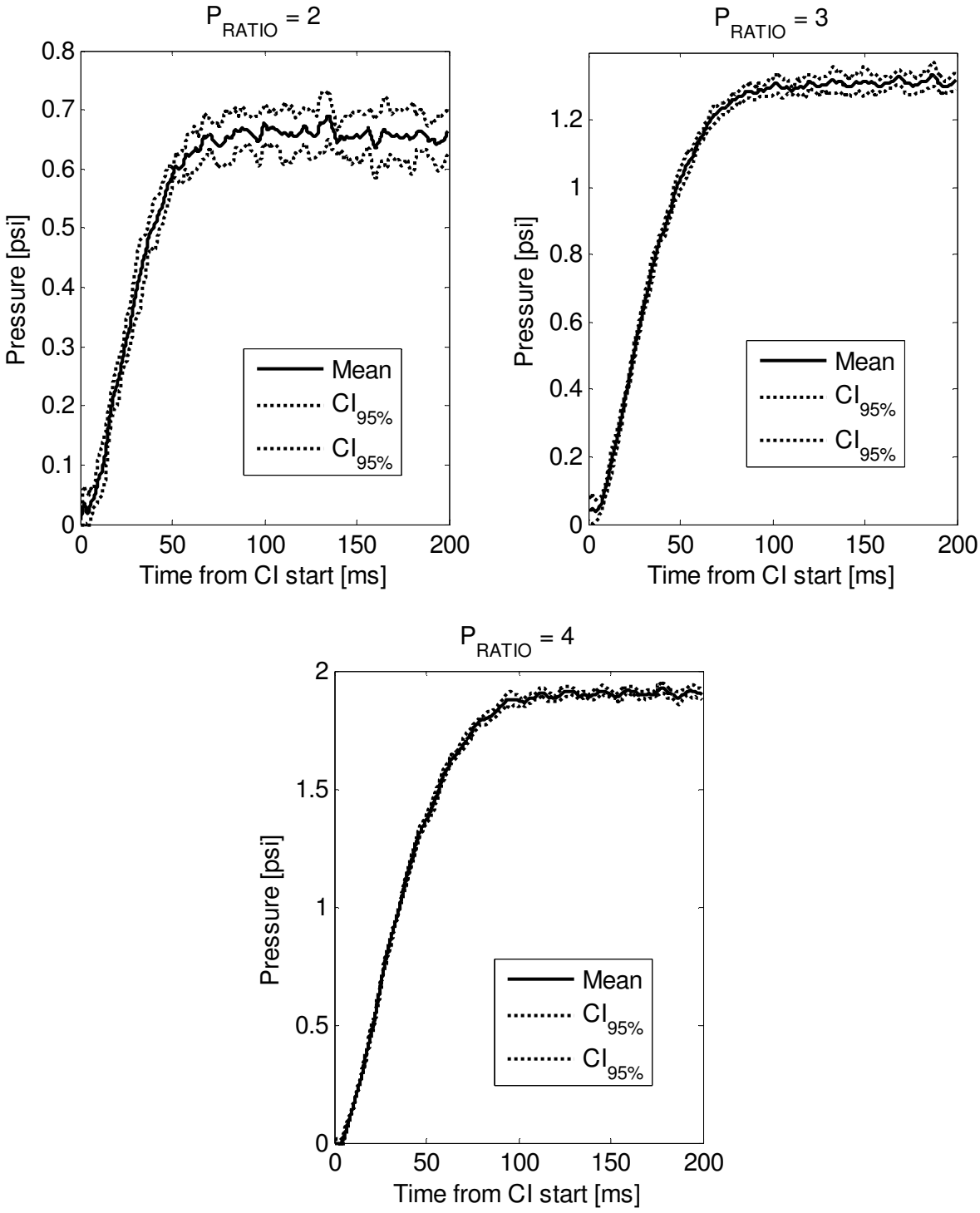

Figure 17 - Cold Flow Injection Plots, Pressure Ratios 2, 3, 4

4.1.1 PSC Injection Mass Flux

The data presented in **Table 4** shows parameter averages and confidence intervals based on eight runs for each pressure ratio. In order to account for pressure regulator error due to the manual pressure changes required, the runs were fully randomized using the random number generator built into MS Excel v. 2007.

Table 4 - Injected NG Mass and RAFR Data at Each Pressure Ratio

Injection pressure ratio, P_R	Main Charge Pressure [psi]	Average Pressure Rise [psi]	Standard Deviation in Pressure Rise [psi]	Mass of NG injected (95% CI) [mg]	Overall RAFR, λ (95% CI)
2	100.0	0.65	0.042	7.53 ± 0.42	15.2 ± 0.80
3	100.0	1.30	0.024	14.8 ± 0.26	7.65 ± 0.12
4	100.0	1.87	0.025	21.3 ± 0.49	5.31 ± 0.06

Table 4 shows the mass of natural gas injected to be repeatable within a maximum of 1 mg for all three pressure ratios. The largest error occurs at a pressure ratio of 2 where the $CI_{95\%}$ interval of 0.82 mg is about 11% of the average value of 7.53 mg. For pressure ratios of 3 and 4 the $CI_{95\%}$ interval becomes even smaller with 3.5% and 4.6% of the average respective values. Thus, for experiments at pressure ratios of 2, the author is 95% confident that the mass of NG injected is within 11% of the average value, while for pressure ratios of 3 and 4 m_{NG} is within 5% of the average value.

4.1.2 PSC Injection Timing

Although the commanded injection duration was maintained at 8.0 ms for all experiments, the actual observed injection duration was significantly longer and also varied with pressure ratio. An end of injection (EOI) timing study was performed based on the pressure data acquired in the cold flow study. First, the pressure data was FFT filtered to remove the high frequency noise over 2 kHz. Next, a mean

post injection pressure value was calculated. Finally, the end of injection time was defined as the time required for the pressure to reach a certain percentage of the mean post injection pressure ($\%P_{MPI}$). **Figure 18** shows two plots of the eight pressure data sets collected at an injection pressure ratio of 4. The circles on the left plot indicate the $95\%P_{MPI}$, while those on the right indicate the $99\%P_{MPI}$ for each of the eight pressure data sets sampled. The circle scatter observed in the time domain had an increasing trend as the percentage of mean pressure defining EOI was increased.

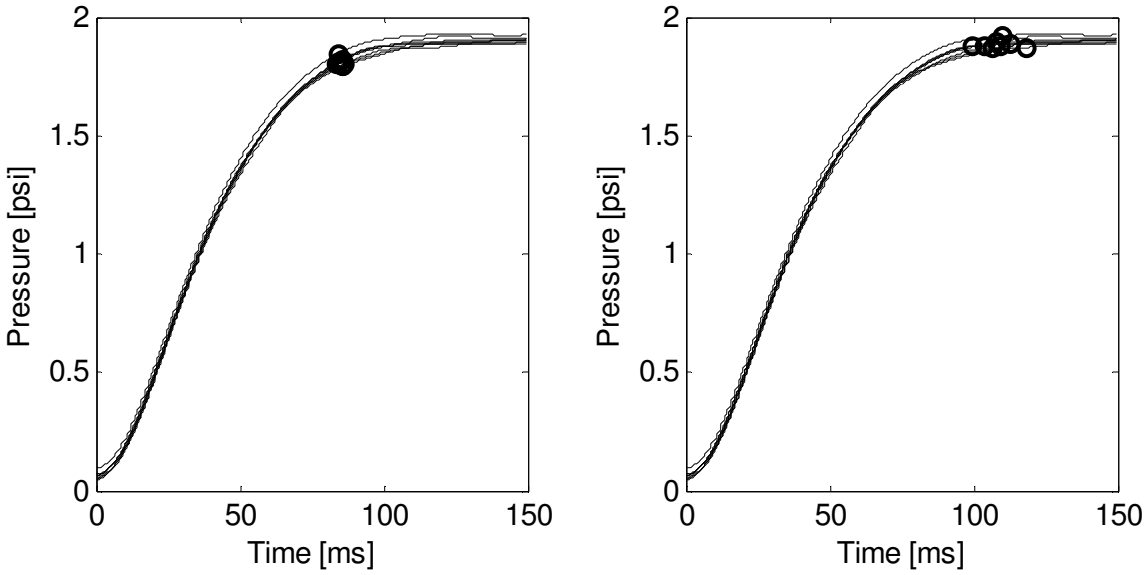

Figure 18 - Cold Flow Pressure Curves for $P_{RATIO} = 4$, $95\%P_{MPI}$ Left, $99\%P_{MPI}$ Right

The increasing scatter with increasing $\%P_{MPI}$ behaviour is also shown in **Figure 19**, where the error bars indicate the 95% confidence intervals. $\%P_{MPI}$ values up to 97.5% exhibited EOI times that were statistically different for each pressure ratio. $\%P_{MPI}$ values of 98% and higher displayed overlapping error bars for pressure ratios of three and four and thus, the EOI times were not statistically different. The higher level of uncertainty for $\%P_{MPI}$ values approaching 100% is explained by the asymptotic pressure curves, where a small change in pressure near the asymptote causes a very large change in the time

domain. It was therefore deemed that a $\%P_{MPI}$ value of 97.5% should be used to define the end of injection.

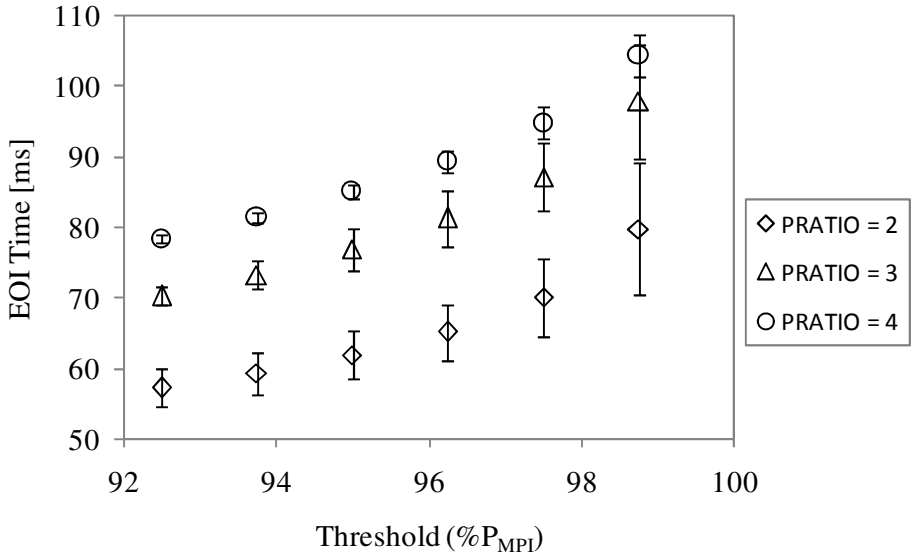

Figure 19 - End of Injection Time as a Function of Percent Mean Value Selected

An EOI time analysis based on the Schlieren photography was also conducted in order to validate the pressure-based injection timing study. The Schlieren videos were visually analysed on a frame by frame basis for all cold flow cases and the following injection parameters were determined: injection start (i_{start}), injection end (i_{end}), and injection duration (i_{dur}). Injection start was established as the time at which the fuel plume first appears at the spark plug electrodes. Injection end was defined as the moment the fuel ceased to flow in the vicinity of the electrodes. Injection duration is the difference between i_{end} and i_{start}. These PSC injection parameters are shown in **Table 5**, along with their 95% confidence intervals.

Table 5 - PSC Injection Timing Parameters Based on Schlieren Photography

P_{RATIO}	PSC Injection Parameters		
	Start, i_{start} [ms]	End, i_{end} [ms]	Duration, i_{dur} [ms]
2	20.5 ± 2.2	72.9 ± 1.4	52.4 ± 3.6
3	16.2 ± 0.7	90.9 ± 1.7	74.7 ± 2.4
4	13.1 ± 0.4	115.3 ± 2.1	102.1 ± 2.5

The PSC timing data based on the Schlieren photography fits in well with the EOI data determined using the pressure approach. The i_{end} parameters determined using the Schlieren photography are plotted alongside the EOI 95% confidence intervals from the pressure measurements in **Figure 20**. For injection pressure ratios of two and three, EOI time values at 98 $\%P_{MPI}$ are a good match, while for injection pressure ratios of 4, $\%P_{MPI}$ value of about 99.5 is required.

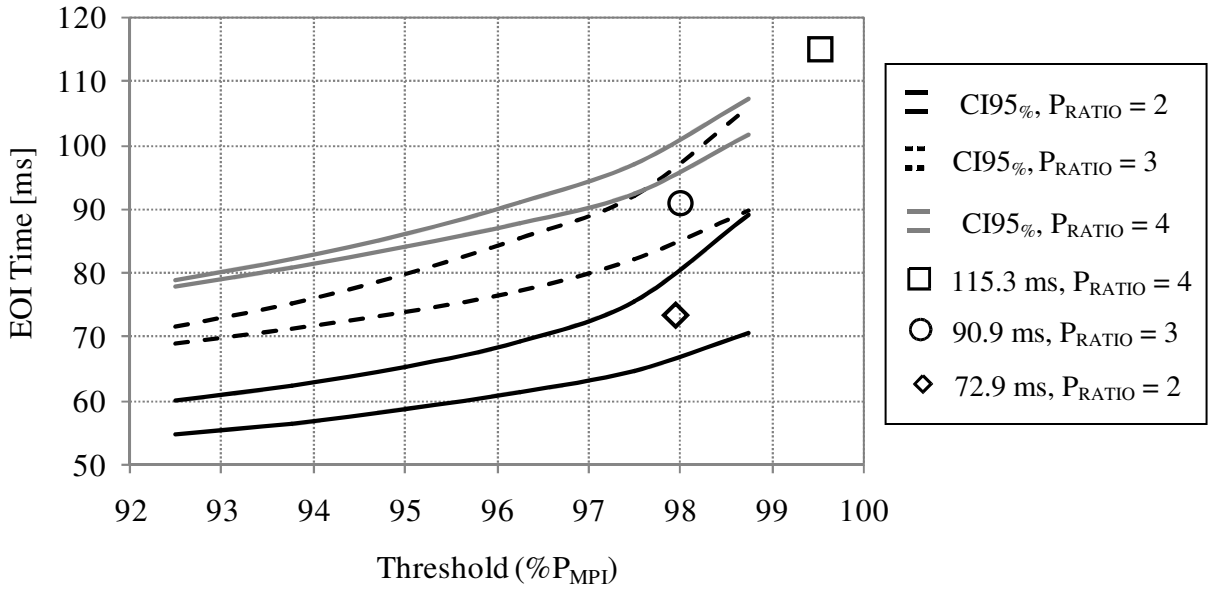

Figure 20 - Comparison Beteen Pressure and Schlieren Photography EOI Study

The injection start values shown in **Table 5** were observed to decrease with increased pressure ratio. These i_{start} values represent the amount of time it takes to first see the fuel plume after the commanded start of injection. It is interesting to note that the i_{start} values are significantly longer than the average

solenoid delay time of 1.95 ms discussed in the previous chapter. The temporal difference between the i_{start} values, which range from 13.1 ms to 20.5 ms, and the solenoid delay, could be attributed to the time required for the fuel to travel through the capillary tube into the spark plug body. The combustion bomb was purged with air by means of pressurizing and depressurizing several times between each experimental run. Consequently, prior to each experiment, the fuel system contained only air downstream of the solenoid valve exit. This air had to be displaced by the fuel during each injection, which explains the additional delay observed between the solenoid valve opening and fuel reaching the electrodes. **Figure 21** shows a close-up the pressure data shown in **Figure 17** in order to demonstrate the difference in injection delay based on the pressure measurements. According to **Figure 21**, a significant pressure rise is observed after ~ 5 ms, which means that the actual start of injection occurred several milliseconds before the natural gas was observed at the spark plug electrodes.

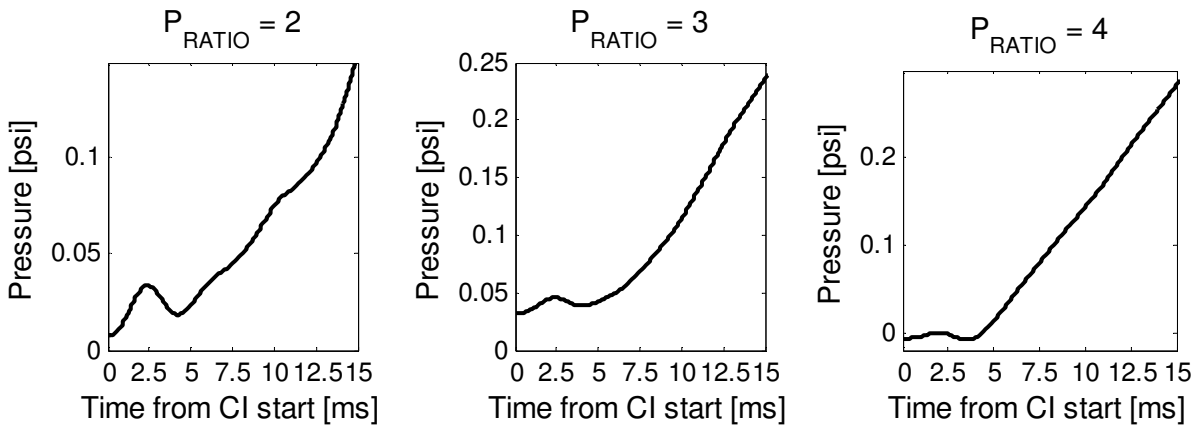

Figure 21 - Injection Start Detail of Cold Flow Pressure Data

The discrepancy in injection delay between that observed in the Schlieren images and that observed from the pressure data varies with pressure ratio from ~ 15 ms at P_{RATIO} = 2 to ~ 7 ms at P_{RATIO} = 4. It is however not unlikely that the actual time required for fuel to reach the spark plug electrodes in a reciprocating engine is closer to that observed in the Schlieren images. Due to the blow-down during the

exhaust stroke and the back-flow of air into the capillary tube during the compression stroke, the gas composition inside the capillary tube may be similar to that observed in these experiments.

4.1.3 Charge Motion Entrainment

Heywood (1988) attributes the engine cylinder charge motion as one of the major factors that controls the combustion process in both spark-ignition and compression ignition engines. Heywood breaks down the charge motion into several types, namely: swirl, squish and tumble. Swirl is defined as organized bulk gas rotation around the cylinder axis. This type of motion is usually accomplished by discharging the intake flow tangentially into the cylinder through the intake valve. Squish refers to the gas motion in the radial direction oriented from the perimeter of the cylinder towards its axis. Squish motion is significant when the piston nears the firedeck and pushes the in-cylinder gases away from the low clearance volume formed near TDC. Tumble is defined as the bulk gas motion around an axis that is perpendicular to the cylinder axis. Tumble motion is usually attained by using two intake valves instead of one, which causes a bias in the flow direction.

Tumble was the most prominent bulk charge motion observed in this study. Due to the lack of the moving parts present in a reciprocating ICE, swirl and squish motions were absent. The tumble motion resulted from the orientation of the PSC spark plug, which injected the fuel with a directional bias. The typical tumble motion observed at a pressure ratio of four is illustrated in the slides of **Figure 22**. Vortices resulting from the shear flow of the injected fuel with the quiescent air were also observed. The large scale vortices were in the order of 15 mm in size at a pressure ratio of four, ~ 7 mm at a pressure ratio of three and ~ 4 mm at a pressure ratio of two. The turbulent motion was seen to dissipate earlier at the smaller pressure ratios.

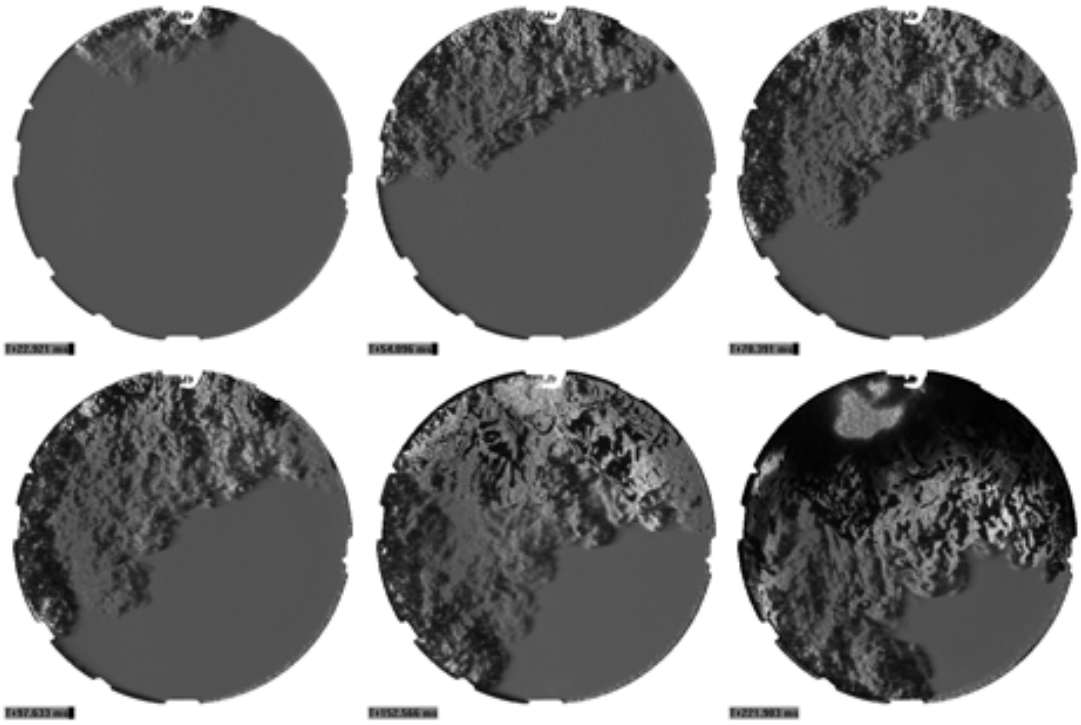

Figure 22 - Progression of Fuel Jet and Combustion Event at $P_{RATIO} = 4$

The amount of charge motion developed was found to vary with time and pressure ratio. The variation with time is explained by the gaseous jet resulting from the fuel injection event, which begins to entrain the quiescent surrounding air near the beginning of injection. The variation with pressure ratio is a result of the increased mass flux as the pressure ratio increases. **Figure 23** shows images taken at the end of injection for each pressure ratio. An image representing the start of injection is also shown, where fuel is just visible exiting the spark plug body. The air-fuel mixture perimeter is outlined with a white line to make the boundary between air and air-fuel mixture clear. As the pressure ratio is increased, the air-fuel mixture occupies an increasing percentage of the combustion bomb. Since the Schlieren images display density gradients inside the combustion bomb, all mixture fraction gradients above zero should be visible. Mixture fraction (ζ) is a conserved scalar which represents the amount of gas that originated from the fuel stream at a certain location "i". Equation 4.1 shows the mixture fraction as a function of mass fraction (Z) of two fluids. The subscripts "1" and "2" represent the fuel and the air streams.

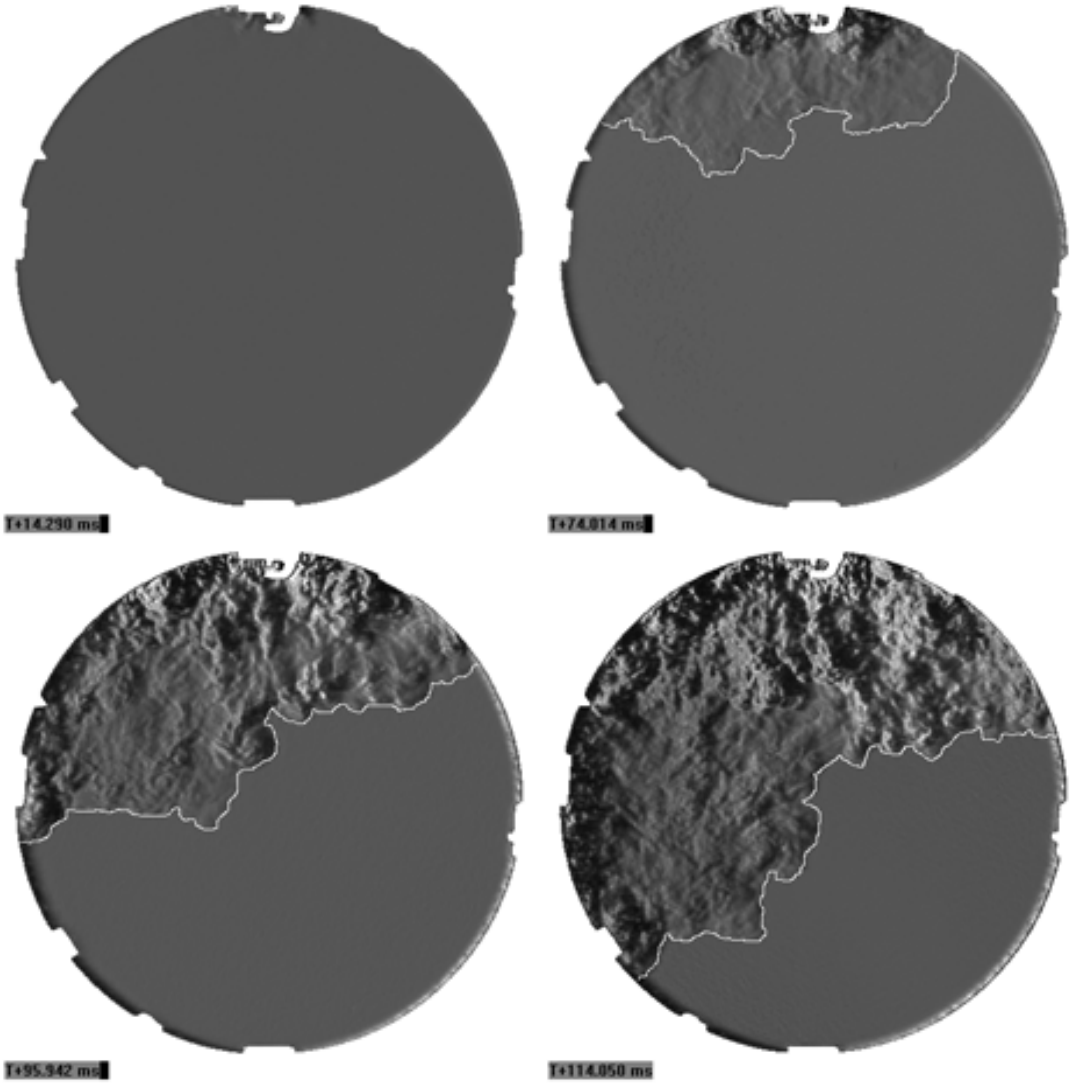

Figure 23 - Schlieren Images of the Start of Injection (Top Left), P_{RATIO} 2 EOI (Top Right), P_{RATIO} 3 EOI (Bottom Left), P_{RATIO} 4 EOI (Bottom Right)

$$\zeta = \frac{Z_i - Z_{i2}}{Z_{i1} - Z_{i2}} \qquad \text{(Eq. 4.1)}$$

The rate of developing charge motion is also observed to increase with increasing pressure ratio. **Figure 24** shows the plot of non-zero density gradient area as a function of time for each pressure ratio. The slopes of the lines which represent rate of jet expansion and air entrainment are seen to increase with

increasing pressure ratio. Also, the maximum area values reached at the end of injection are seen to increase with increasing pressure ratio. The plots in **Figure 24** were determined based on the image binarization technique further discussed in section 4.2.5.

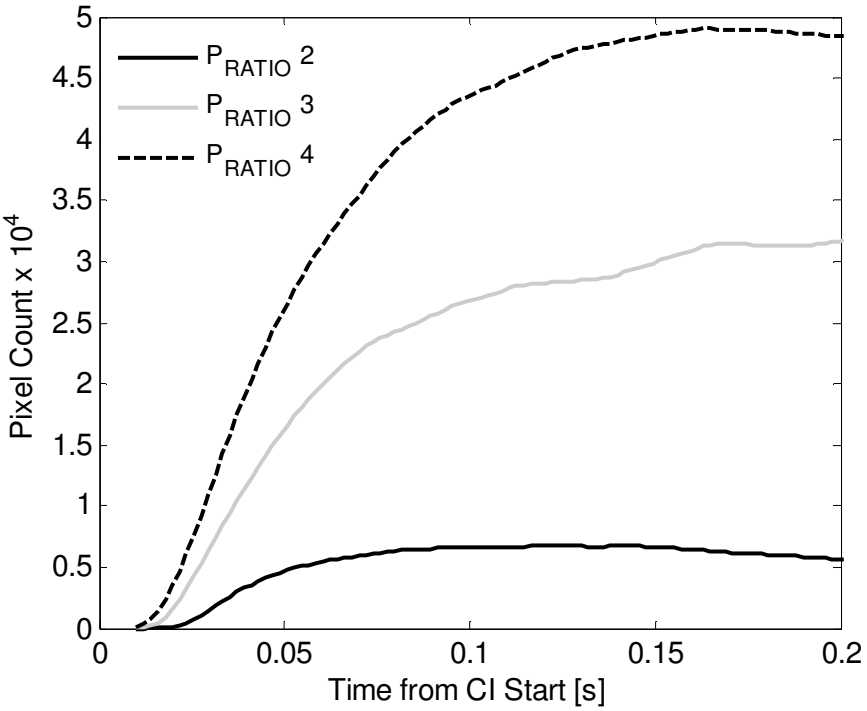

Figure 24 - Cold Flow Injection Average Pixel Count

The pixel count for a pressure ratio of two in **Figure 24** begins to slowly decay after ~ 150 ms. This is due to the fact that Schlieren imaging works on density gradients, and the density gradients are slowly disappearing as the injected fuel continuously diffuses and mixed with the surrounding air.

4.2 COMBUSTION ANALYSIS

A combustion analysis based on the pressure data for each combusting event was performed to determine the changes in combustion characteristics as the spark timing (T_S) and pressure ratio (P_{RATIO}) were varied. Combustion characteristics including ignition delay (t_{ign}), combustion duration (t_{comb}), heat release rate (HRR), and integrated heat release (IHR) were investigated. The ignitability of the jet plume was very dependent on spark timing as well as pressure ratio. The combustion success shown in **Figure 25** is a parameter that represents the ratio of combusting runs to the total runs performed at a certain spark timing and pressure ratio. The error bars were determined using the 90% confidence intervals for proportions equation specified by Navidi (2006). The combustion parameters previously mentioned were influenced by both the spark timing and the injection pressure ratio, although pressure ratio was found to alter combustion performance more significantly. These findings will be further discussed in the following sections.

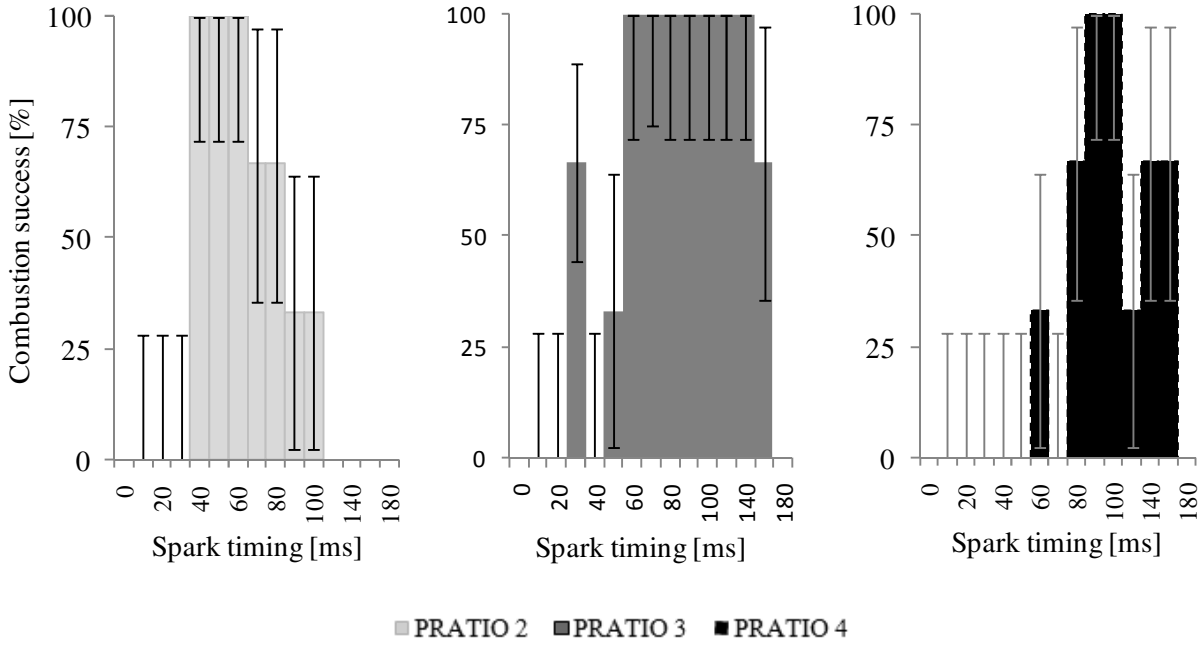

Figure 25 - Combustion Success as a Function of Spark Timing for Each Pressure Ratio

The combustion success parameter in **Figure 25** is a good indicator of the combustion reliability. Repeated attempts to ignite the jet plume at less than ideal conditions, such as those with a combustion success of less than 100%, would result in poor performance and high emissions. Spark time intervals that exhibit reliable combustion (100% success rate) are shown in **Table 6** for each pressure ratio. One point of interest in **Figure 25** is at a pressure ratio of three and a spark timing of 30 ms. Several repeats were performed at this test point; however, combustion success remained intermittent (about 66%). Although P_{RATIO} and T_S were maintained constant, the ignitability of the jet plume varied presumably due to the chaotic nature of turbulence. The position of the jet plume at the time of spark became the leading factor governing the flammability. This point will be further discussed in the image analysis sections to follow. Points tested with spark timings just above and below this value (40 ms and 20 ms) showed no signs of combustion.

Table 6 - Spark Timing with 100% Combustion Success

P_{RATIO}	Range [ms]			Window [ms]
2	40	→	60	20
3	60	→	140	80
4	90	→	100	10

Test cases with an injection pressure ratio of three demonstrated the widest spark timing window that results in successful combustion. Minimum spark timings that lead to successful combustion were found to increase with increasing pressure ratio. The least favourable pressure ratio was found to be four, as it required the highest spark timing retardation and it had the narrowest spark timing window (10ms).

It is interesting to note that the experiments conducted by Gorby on the Ricardo Hydra were at an average injection pressure ratio of four. As mentioned above, this pressure ratio is the least favourable amongst the three tested and it requires a minimum spark delay of 90 ms between CSOI and the time of spark for

reliable combustion to occur. Although it is understood that the engine charge motion and mixing scales are much different from those observed in the combustion bomb, it is useful to point out the engine test conditions for comparative purposes. Gorby maintained a constant CSOI of 41 CAD before the time of spark. Since most of his testing was conducted at 2000 RPM, this translates to 3.42 ms between the commanded start of injection and the time of spark. As previously shown in Section 4.1.2, the duration between commanded start of injection and the time the fuel jet plume is observed at the spark plug electrodes is 13.1 ± 0.4 ms. This result sheds some light on Gorby's inability to ignite the PSC charge, since it is likely that there was no fuel present at the spark plug electrodes at the time of spark. Also, according **Table 6**, a spark timing delay of 3.42 ms is ~ 25 times less than that required for the successful combustion of the PSC charge in the constant volume bomb at the pressure ratio used by Gorby. Considering that a full engine cycle lasts 60 ms at 2000 RPM, some modifications may be necessary to the PSC injection system in order to reduce the required spark delay.

Examples of test cases which were not ignitable are shown at the time of spark for each pressure ratio in **Figure 26**, **Figure 27**, and **Figure 28**. The top left images in **Figure 26** and **Figure 27** indicate that the spark was triggered before the fuel jet was present. The top right images in **Figure 26** and **Figure 27** and the top left image in **Figure 28** correspond to snapshots of the spark near the head of the jet. It is conjectured that because the amount of air that has been entrained into the jet plume near the beginning of injection is likely very small, the spatial distribution of ignitable mixture is very limited and ignition is not repeatedly achievable. The bottom left and the top right images in **Figure 27** and **Figure 28** are examples of spark initiation near the beginning of injection, after the air that was present prior to injection has been displaced away from the electrodes. At this point, the air-fuel mixture is believed to be outside its flammability limits, since it is likely very fuel rich near the electrodes. Examples of four cases where the fuel is thought to have mixed past its flammability limits are shown in the bottom frames of **Figure 26** and in the bottom right frames of **Figure 27** and **Figure 28**. In all four instances, the spark was triggered after the observed fuel injection had completed and the bulk gas motions nearly dissipated. Since the

overall relative air/fuel ratio in each case is most probably far beyond the lean limit of combustion, the spark initiated in a fuel-lean zone and no flame was observed.

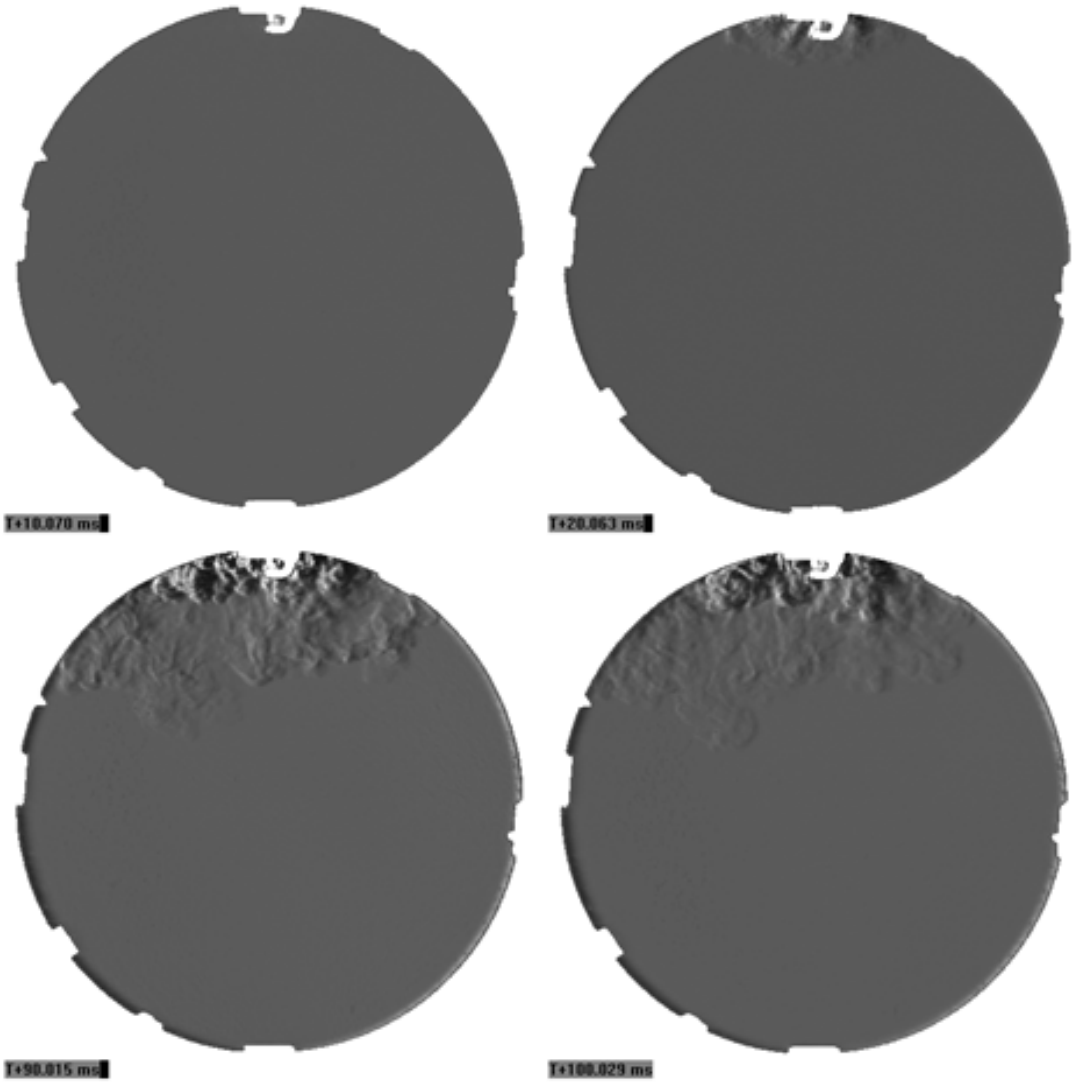

Figure 26 - Examples of Incombustible Test Cases for P_{RATIO} = **2**: T_S = 10 ms (Top Left), T_S = 20 ms (Top Right), T_S = 90 ms (Bottom Left), T_S = 100 ms (Bottom Right)

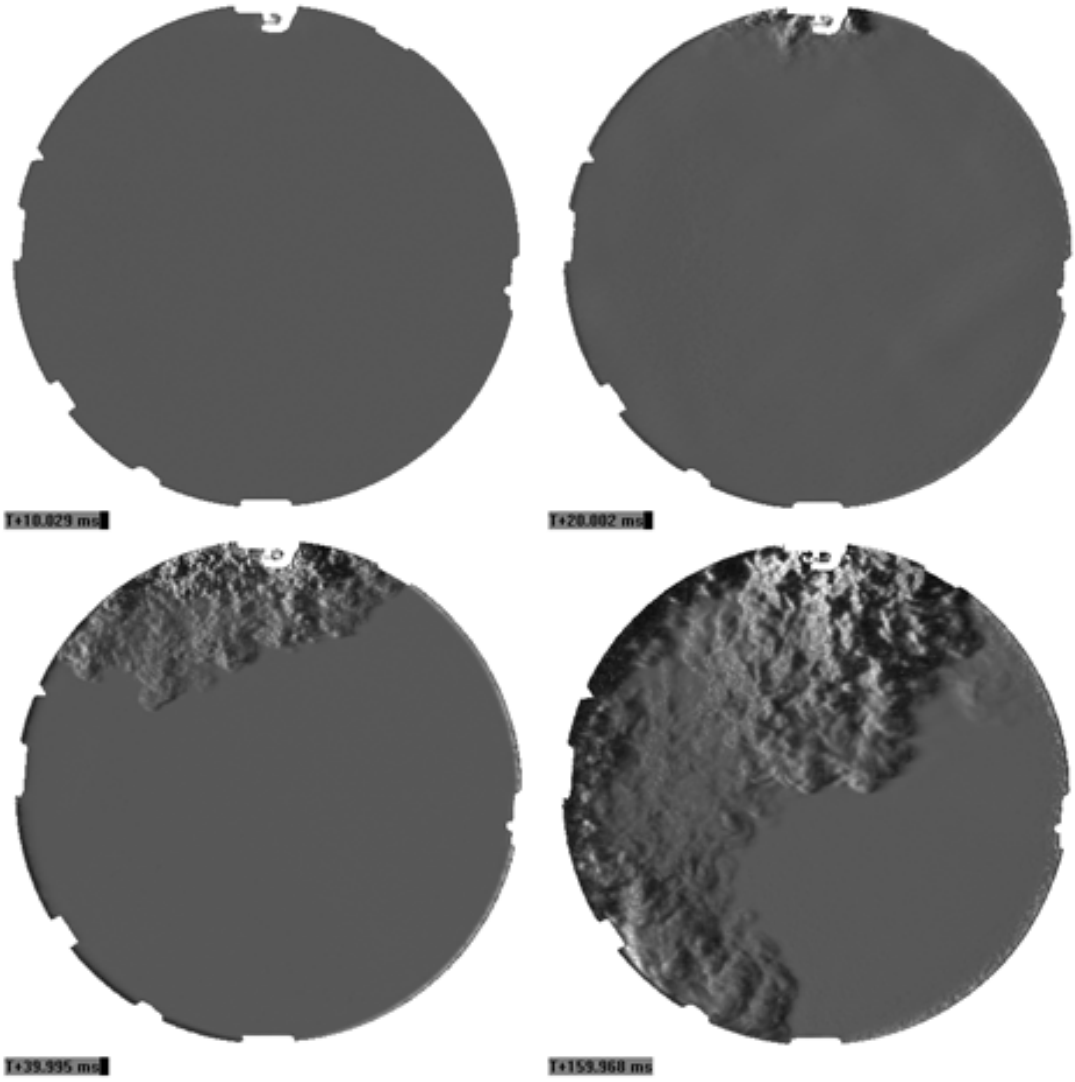

Figure 27 - Examples of Incombustible Test Cases for P_{RATIO} = **3**: T_S = 10 ms (Top Left), T_S = 20 ms (Top Right), T_S = 40 ms (Bottom Left), T_S = 160 ms (Bottom Right)

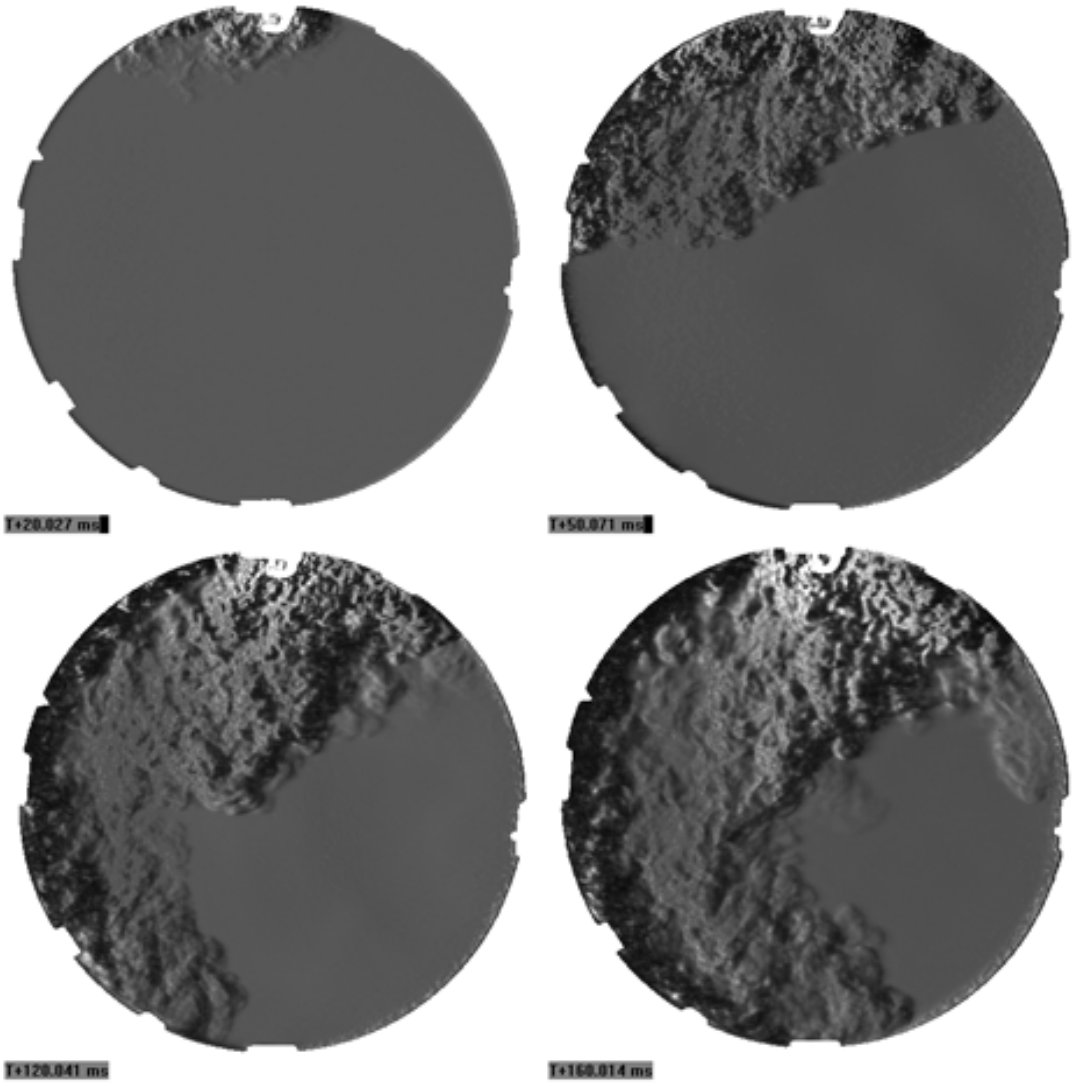

Figure 28 - Examples of Incombustible Test Cases for P_{RATIO} = **4**: T_S = 20 ms (Top Left), T_S = 50 ms (Top Right), T_S = 120 ms (Bottom Left), T_S = 160 ms (Bottom Right)

4.2.1 Integrated Heat Release Analysis

Although the primary interest of this study was to determine the pressure ratios and spark timings that lead to successful combustion, the quality of combustion was of interest as well. One run is said to have better combustion quality than another if the amount of net heat released is higher, the heat is released at a higher rate, and the combustion delay is lower. The cold flow study demonstrated that at constant injection pressure ratio, the injected amount of fuel will remain constant, in the worst case scenario to within 11% of the average value. Therefore, in order to compare the combustion quality of different spark timings at constant pressure ratio, it is helpful to look at the amount of heat released in each test.

It is important to note that the heat release studies performed yield net heat release results only. In order to determine the gross heat release, one must know the heat transfer through the walls of the combustion bomb. Since this experiment was not set up to do heat flux measurements the inefficiencies due to combustion and the heat losses from the combustion bomb must be grouped together. Equation 4.2 defines the net heat release rate according to Stone (1999), where Q_{net}, Q_{hr} and Q_{ht} are the net heat release, the gross heat release and the heat transfer respectively.

$$\frac{dQ_{net}}{d\theta} = \frac{dQ_{hr}}{d\theta} - \frac{dQ_{ht}}{d\theta} = \frac{\gamma}{\gamma - 1} p \frac{dv}{d\theta} + \frac{1}{\gamma - 1} v \frac{dp}{d\theta} \qquad \text{(Eq. 4.2)}$$

Equation 4.2 gives the crank angle (θ) resolved heat release (normally applied to an operating ICE) as a function of instantaneous pressure (p), instantaneous volume (v), and the ratio of specific heats (γ). In the case of the constant volume combustion bomb, Equation 4.2 is applied on a time varying basis and the volume varying term drops out. The result is shown in Equation 4.3.

$$\frac{dQ_{net}}{dt} = \frac{dQ_{hr}}{dt} - \frac{dQ_{ht}}{dt} = \frac{1}{\gamma - 1} v \frac{dp}{dt} \qquad \text{(Eq. 4.3)}$$

Considering the large mass of the combustion bomb steel walls, they are assumed to be a constant temperature heat sink. The test cell ambient temperature was maintained at a near constant 15 °C. Also, the initial temperature of the charge was found to be within 5 °C between runs. Thus, the heat transfer out of the combustion bomb is assumed to be constant at constant pressure ratio. The heat transfer is assumed to vary with pressure ratio, since the mass of injected fuel also varies with pressure ratio. Since the heat transfer is assumed constant for a constant pressure ratio, the changes in gross heat release are reflected in the net heat release value. A sample plot of net heat release rate and net integrated heat release is shown in **Figure 29**.

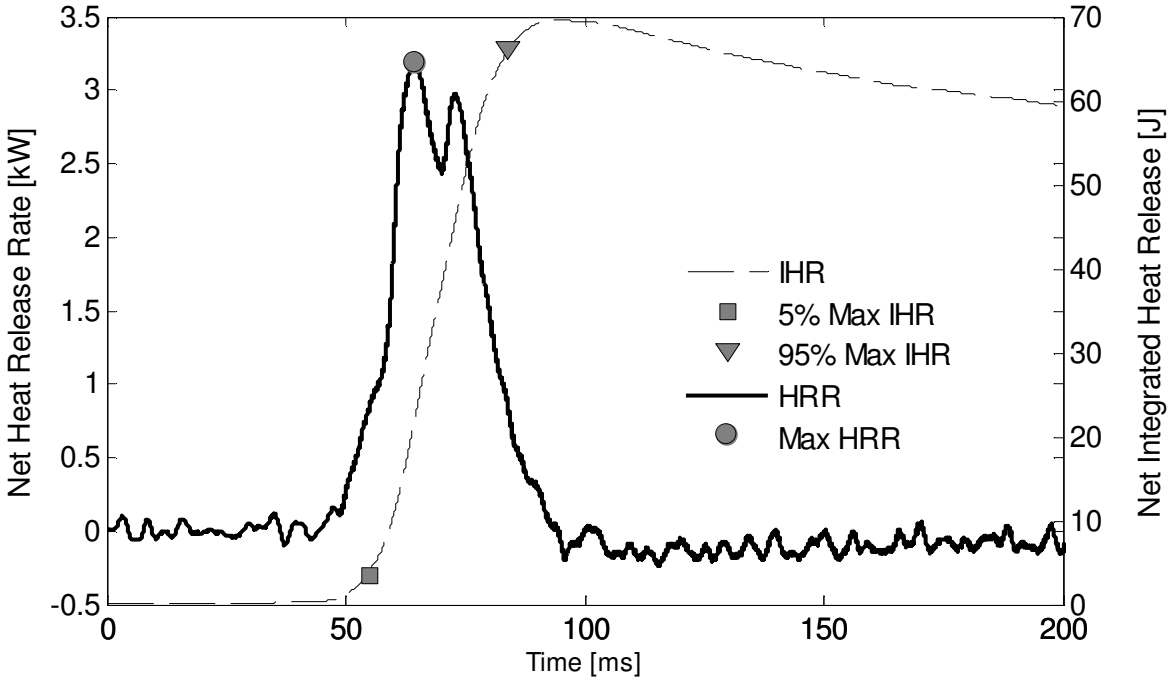

Figure 29 - Net Heat Release Plot for Exp 043, $P_{RATIO} = 3$, $T_S = 30$ms

The combustion parameters discussed in the following sections are determined based on the heat release data of each individual run, which are typical to that shown in **Figure 29**. Start of combustion is defined as the point where 5% of the maximum integrated heat release has been reached. End of combustion is defined as 95% of the maximum integrated heat release. The duration between the time of spark and the

time of 5% max IHR is referred to as the ignition delay (t_{ign}). Combustion duration (t_{comb}) is defined as the time between 5% max IHR and 95% max IHR. The Schlieren images corresponding to the time of spark, 5% max IHR, max HRR and 95% max IHR are shown in **Figure 30**. The flame can be distinguished from the unburned fuel by the increased luminosity gradients. In this run, the ignition delay (t_{ign}) is 24.84 ms (top right), the maximum heat release rate is 3.2 kW (bottom left) and the combustion

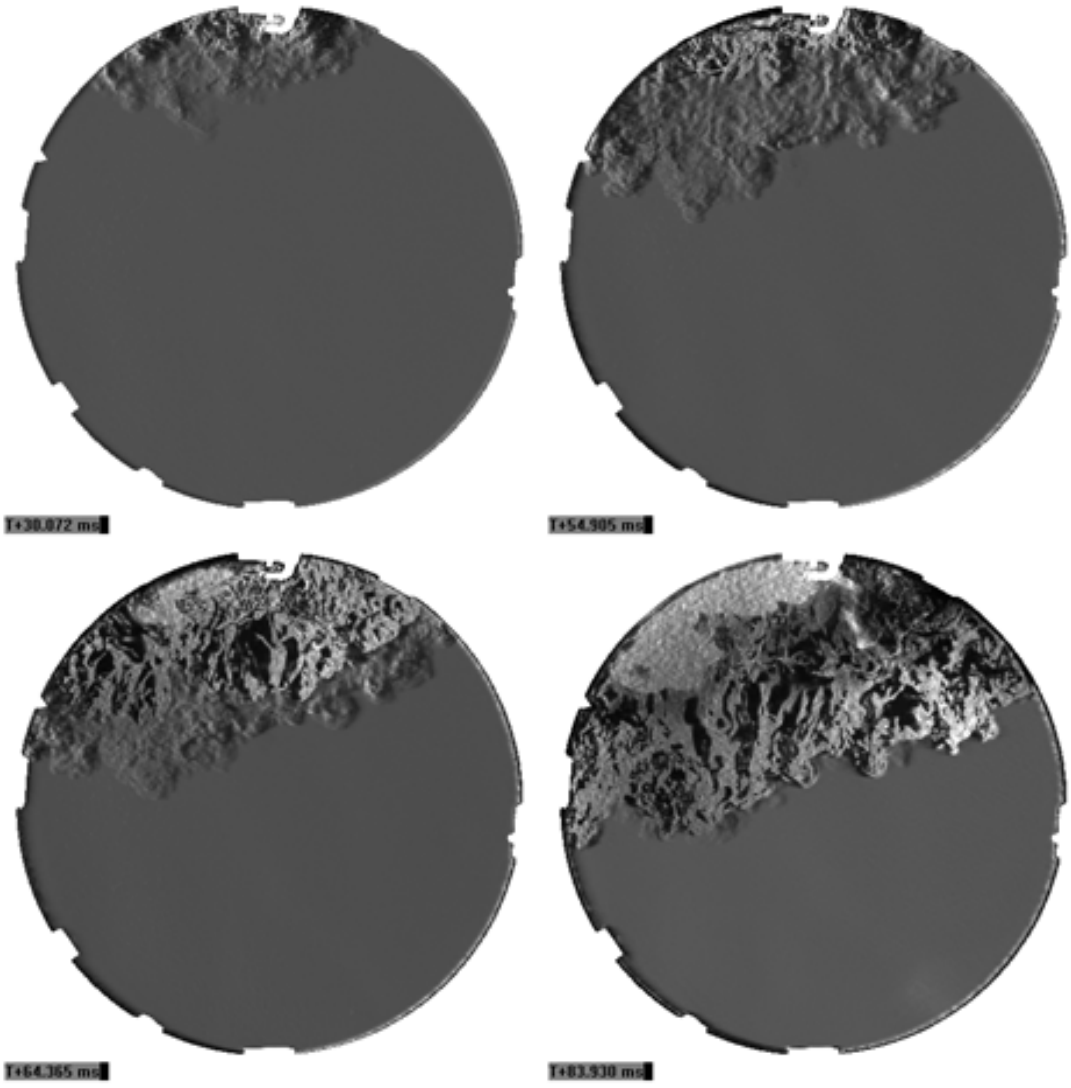

Figure 30 - Schlieren Images Corresponding to T_S (Top Left), 5% Max IHR (Top Right), Max HRR (Bottom Left), and 95% Max IHR (Bottom Right) for $P_{RATIO} = 3$, $T_s = 30$ ms

duration is 29.12 ms (bottom right). Note that a significant amount of fuel has flown past the spark plug electrodes at the time of spark, which is clearly seen in the top right image.

The heat release due to combustion as a function of spark timing is shown in **Figure 31**, **Figure 32**, and **Figure 33**, for pressure ratios of two, three and four respectively. It is expected that the longer the spark is delayed after commanded injection, the longer that the injected natural gas will have to mix with the surrounding air. Some of this natural gas will inevitably mix past the lean limit of combustion (LLC) and will therefore not burn. Thus, the heat release due to combustion is expected to decrease with increasing spark delay. The study of stratified methane injections in a constant volume bomb conducted by Kitagawa et al. (2002) found that the mass fraction burned decreased with increasing ignition timing due to bulk quenching of the flame in the over lean surroundings.

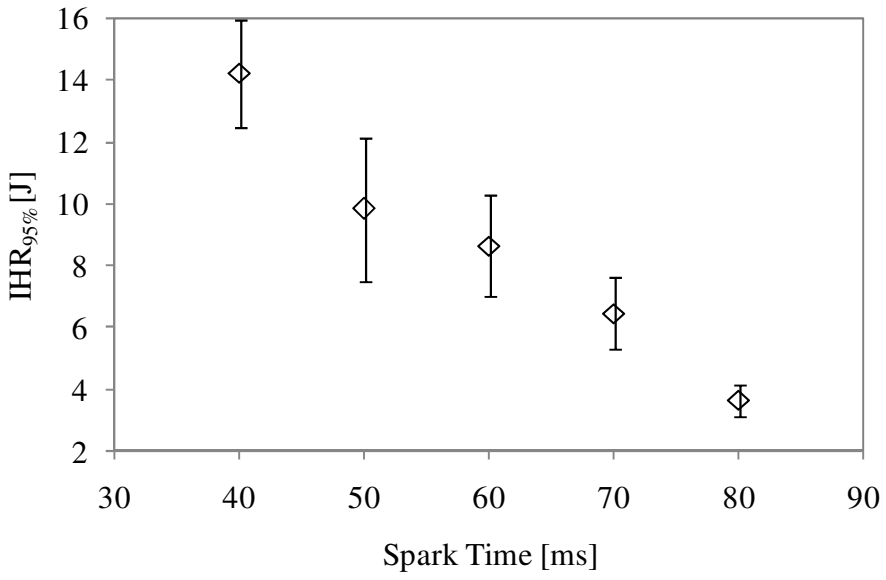

Figure 31 – Net Integrated Heat Release for $P_{RATIO} = 2$

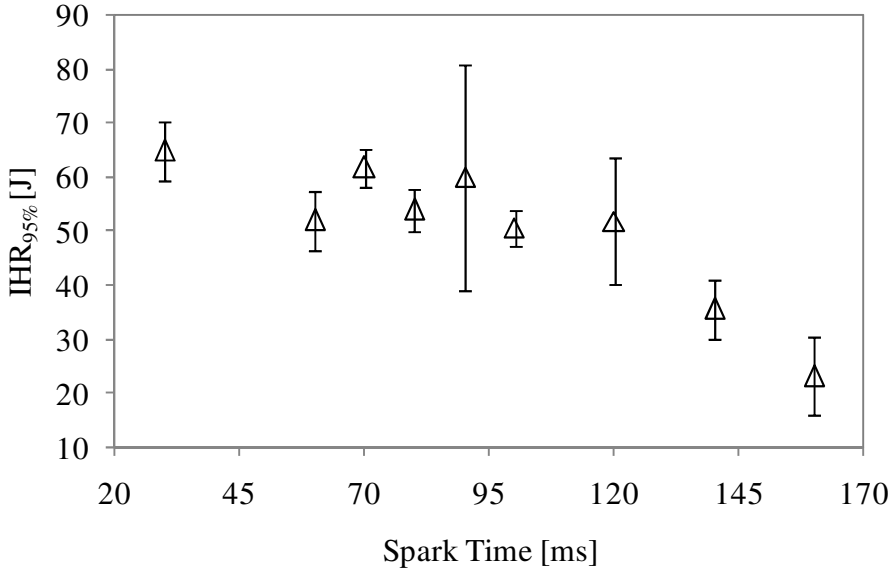

Figure 32 - Net Integrated Heat Release for $P_{RATIO} = 3$

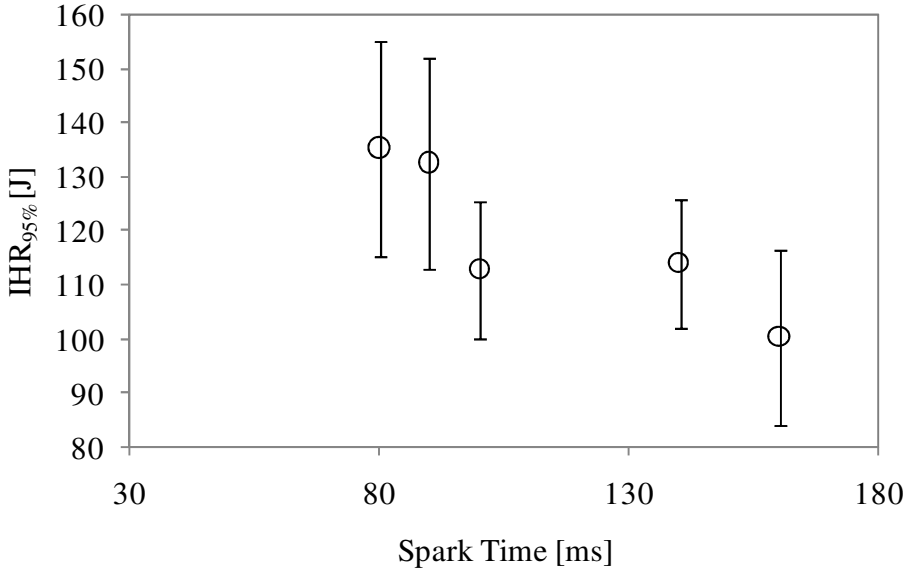

Figure 33 - Net Integrated Heat Release for $P_{RATIO} = 4$

The combustion heat release seems to be a strong function of spark timing for pressure ratios of two and three. At a pressure ratio of two, the heat release steadily decreases by more than three times that of the best case value of 14 J at 40 ms to 4 J at 80 ms spark delay. Similar behaviour is seen from the results at

a pressure ratio of three, where the heat release decreases from ~ 65 J at 30 ms to ~ 25 J at 160 ms spark delay. Although the average values of heat release for pressure ratios of four also decrease with increasing spark delay, the results are not statistically different due to the large uncertainties observed. It is thought that the large error bars in **Figure 33** are primarily due to increased turbulence in the combustion bomb resulting from the high injection pressure. The large turbulence generated at a pressure ratio of four is expected to introduce a high variability in the amount of fuel that mixes past the LLC and thus, the dependence of heat release on spark delay is not as apparent.

Since the amount of fuel injected is unchanged at constant pressure ratio, it is expected that the amount of unburned fuel should increase with decreasing integrated heat release. Schlieren images of the time of spark and the time at which combustion ends are shown in **Figure 34**, **Figure 35**, and **Figure 36** for pressure ratios of two, three and four. A white line is drawn around the perimeter of the flame front to help distinguish the burned mixture from the unburned reactants. The top frames in each figure represent the most advanced spark timing that lead to successful charge ignition for each pressure ratio. The bottom frames represent the most retarded spark timing that can sustain successful charge ignition.

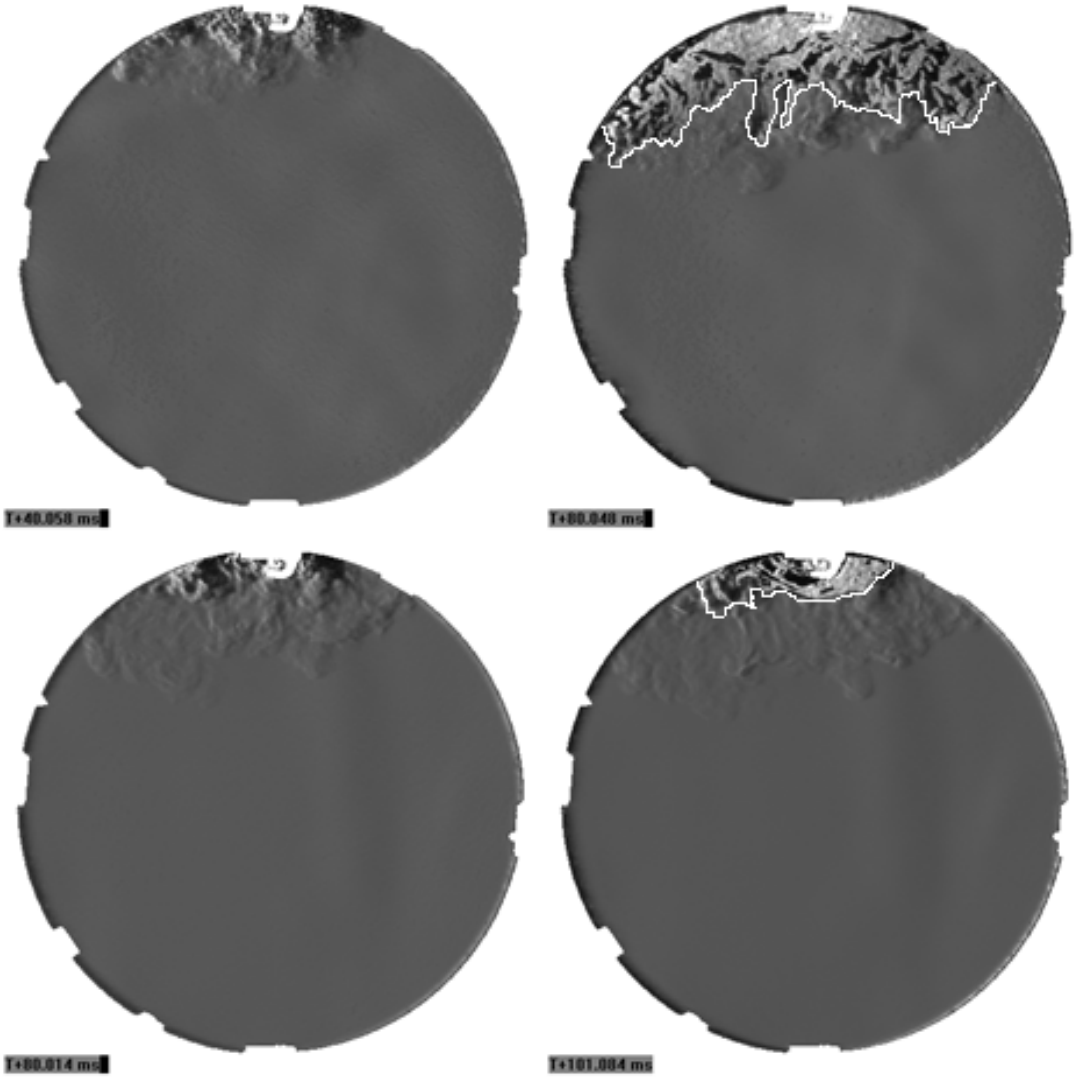

Figure 34 - Schlieren Images at Time of Spark (Left) and 95% Max IHR (Right) for T_S = 40 ms (Top) and T_S = 80 ms (Bottom) at P_{RATIO} = 2

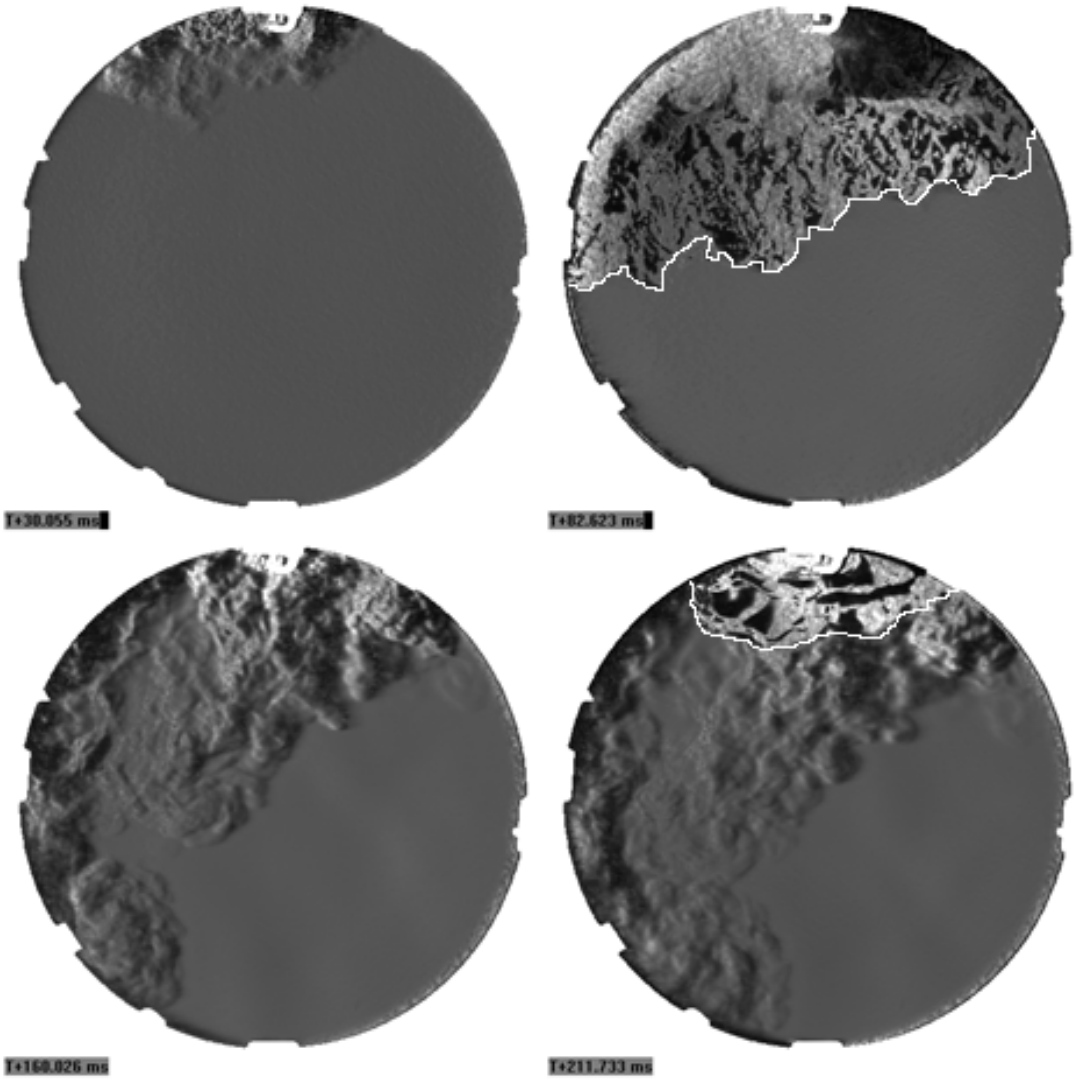

Figure 35 - Schlieren Images at Time of Spark (Left) and 95% Max IHR (Right) for T_S = 30 ms (Top) and T_S = 160 ms (Bottom) at P_{RATIO} = 3

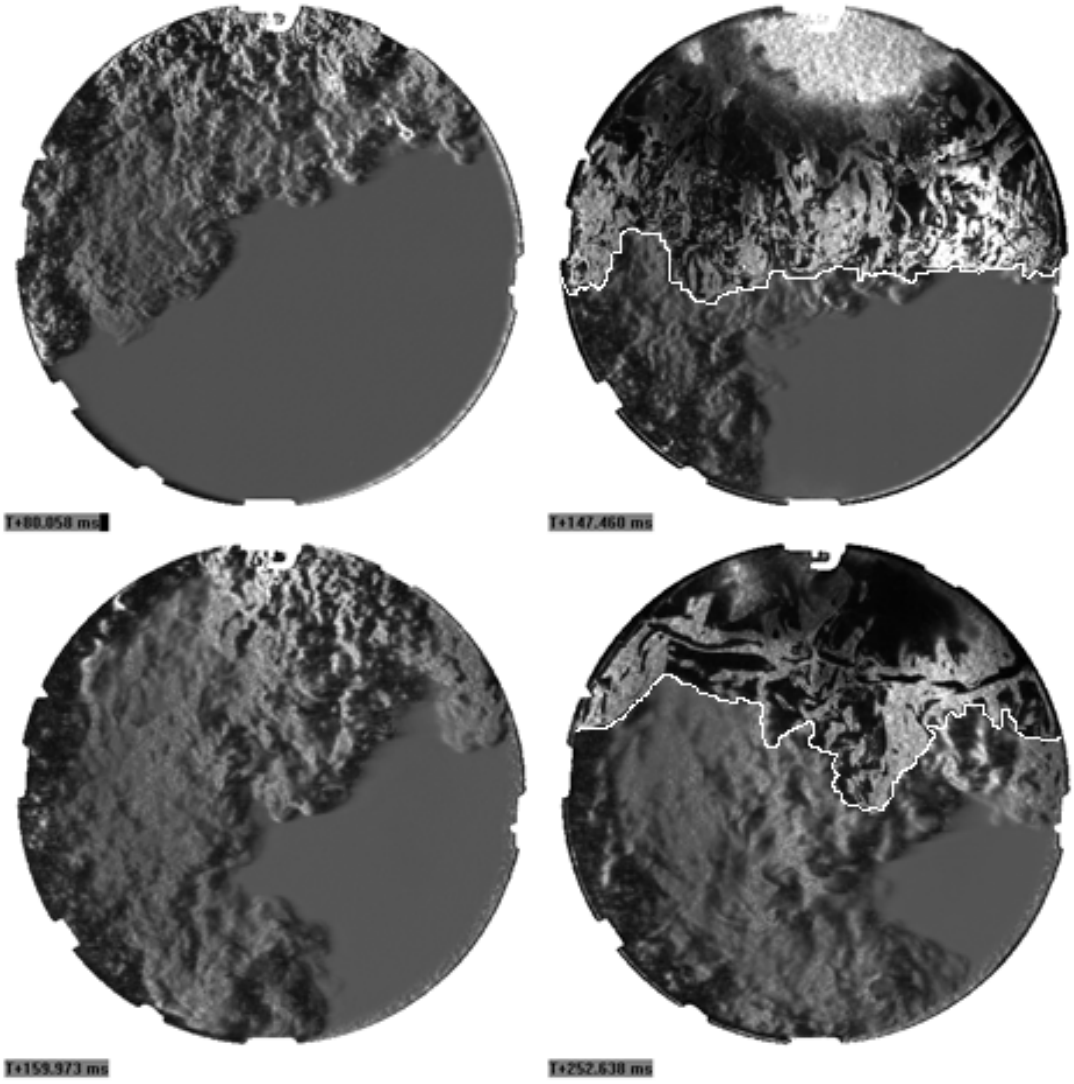

Figure 36 - Schlieren Images at Time of Spark (Left) and 95% Max IHR (Right) for T_S = 80 ms (Top) and T_S = 160 ms (Bottom) at P_{RATIO} = 4

The expected trend is apparent at all three pressure ratios, as the amount of unburned fuel remaining at the end of combustion for the earlier spark timings is significantly less. The difference between the early and late spark timings is most apparent for a pressure ratio of three. **Figure 35** shows that at a spark timing of 30 ms the amount of unburned fuel is minimal, while at T_S = 160 ms the burned gases are only present in the vicinity of the spark plug and the unburned gases occupy nearly 2/3 of the combustion bomb.

4.2.2 Heat Release Rate Analysis

According to Heywood (1988) the rate of heat release is governed primarily by flame type, i.e. premixed or diffusion. The premixed flame speed varies with charge motion, charge composition and combustion chamber geometry. Diffusion flame combustion rates are dependent on injection rate, fuel composition and charge motion. The type of flame present in these experiments is dependent on both pressure ratio and spark timing. Late spark timings allow the fuel and air to mix for a longer duration and thus the combustion consists of a premixed flame. Early spark timings initiate combustion as a premixed flame, followed in some cases by a diffusion flame. Pressure ratio affects the rate of heat release since fuel injected at a higher pressure ratio has an increased momentum flux and thus enhances the air entrainment into the fuel. Also, the increased turbulence generated at higher pressure ratios increases the flame speed by "wrinkling" the flame, which has the effect of increasing the flame surface area. For a diffusion flame, increased turbulence results in steeper air-fuel concentration gradients. These increase the heat release rate by increasing local rates of diffusion.

The maximum rate of heat release in **Figure 37**, **Figure 38**, and **Figure 39** is plotted against spark timing for pressure ratios of two, three and four respectively. At a pressure ratio of two, the maximum HRR is a strong function of spark timing and it is observed to decrease with increasing spark timing. The plot of maximum HRR in **Figure 38** indicates a similar dependence on spark timing as that in **Figure 37**, however, the uncertainties are higher. The maximum rate of heat release graph in **Figure 39** shows no statistical dependence of maximum HRR on spark timing for a pressure ratio of four, as HRR rate values are all within the error bars shown. The observed injection duration at a pressure ratio of four is significantly longer than at pressure ratios of two and three. Since the end of the observed fuel injection occurs long after the time of spark for pressure ratios of four, considerable charge motion in the form of bulk gas flows and turbulent vortices is still present during the combustion event. This is believed to be

the primary reason that the maximum rate of heat release is unaffected by spark timing at this pressure ratio.

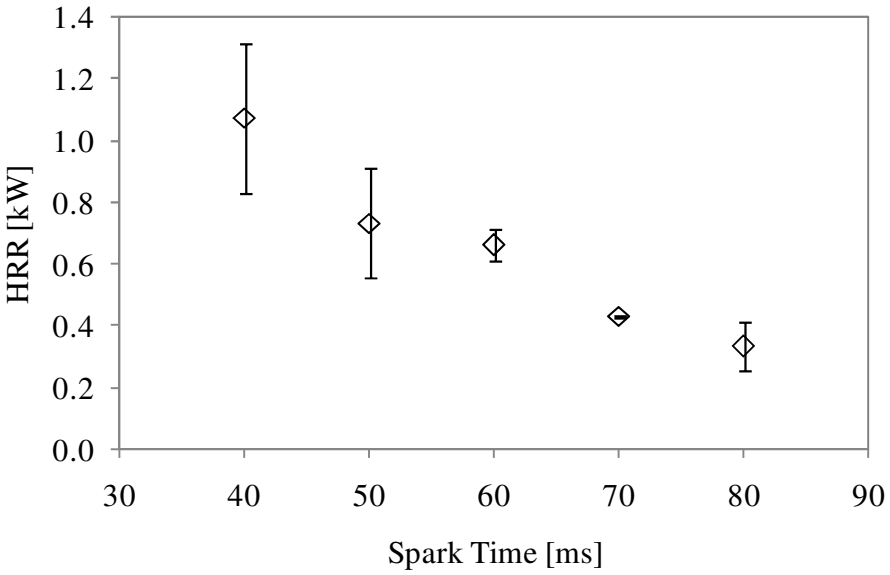

Figure 37 - Maximum Rate of Heat Release for $P_{RATIO} = 2$

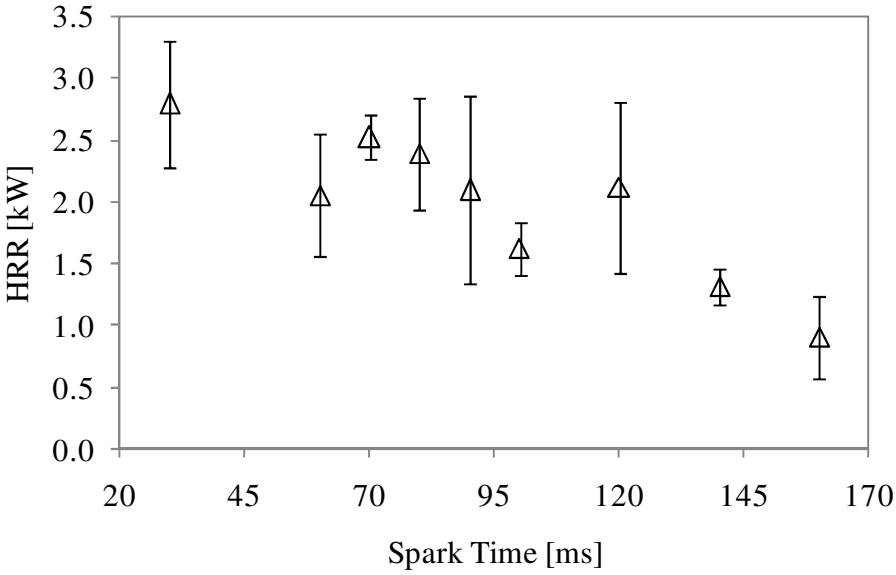

Figure 38 - Maximum Rate of Heat Release for $P_{RATIO} = 3$

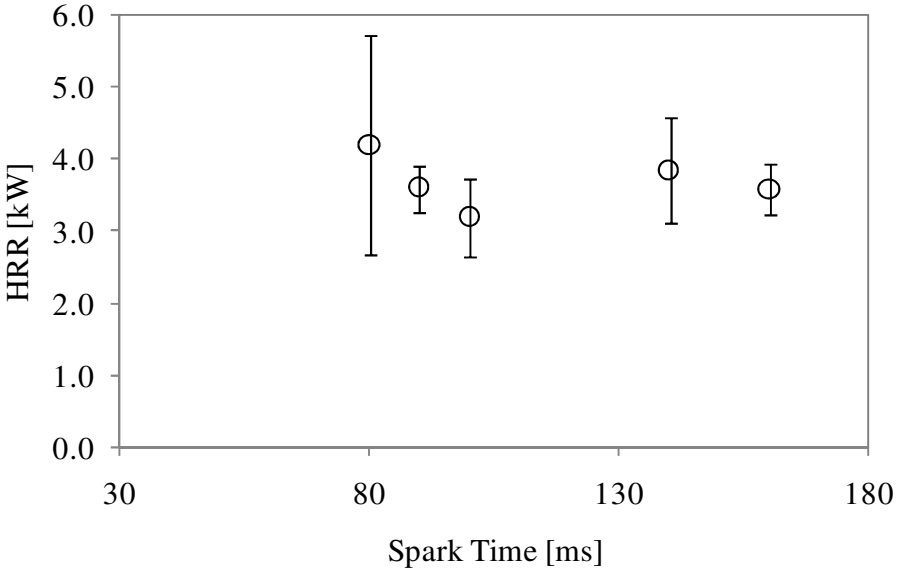

Figure 39 - Maximum Rate of Heat Release for $P_{RATIO} = 4$

4.2.3 Combustion Duration Analysis

Two factors that govern combustion duration in a stratified charge environment are fuel-oxidizer mixing rate and quantity of fuel available. The mixing rate is proportional to the charge motion inside the combustion chamber and the gas diffusion rates. The charge motion in these experiments was entrained by the fuel injection event and was further described in Section 4.1.3. As the fuel injection event nears completion, charge motion was observed to diminish until it is completely dissipated. This observation was consistent with that of Alger *et al.* (2005) who conducted particle image velocimetry (PIV) studies in a gasoline direct injected (GDI) engine operating at 750 RPM. Alger *et al.* determined that the charge motion entrained from the fuel injection event dissipated within ~ 9 ms (40 CAD) after the end of injection.

As mentioned in the previous section, charge motion is a parameter that strongly influences the flame speed. Therefore, in the case of these experiments, the flame speed should increase during the fuel

injection process and decrease near the end of injection. If combustion duration were governed solely on flame speed, it would be expected that ignition close to the end of injection should increase the burn time. However, in a stratified environment, if the spark event is highly delayed, more fuel mixes past the lean limit. When the spark initiates, the flame kernel grows, and consumes only reactants which are within the flammability limits of the fuel. Since there is now less fuel available to burn at the later spark timings, the combustion duration will decrease.

Given that the charge motion inside the combustion bomb and the amount of fuel available to burn both decrease with increasing spark timing, a clear trend in combustion duration with spark timing is difficult to predict. The combustion duration for a pressure ratio of two is plotted in **Figure 40**. The only spark timing that stands out to be significantly different from the rest is at 40 ms. At a pressure ratio of three (**Figure 41**), the combustion duration starts with a value of 37 ms at a spark timing of 30 ms, steadily increases to a maximum at a spark timing of 100 ms, and then abruptly drops again at T_S = 120 ms. It is likely that the fuel available to burn after 100 ms significantly decreases. For a pressure ratio of four,

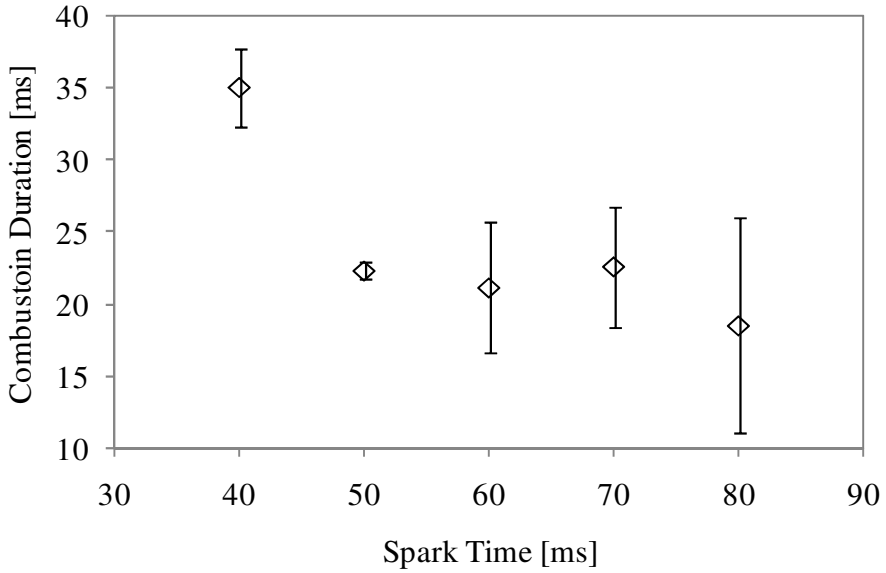

Figure 40 - Combustion Duration for P_{RATIO} = 2

which is shown in **Figure 42**, the combustion duration values are not statistically different for any spark timing.

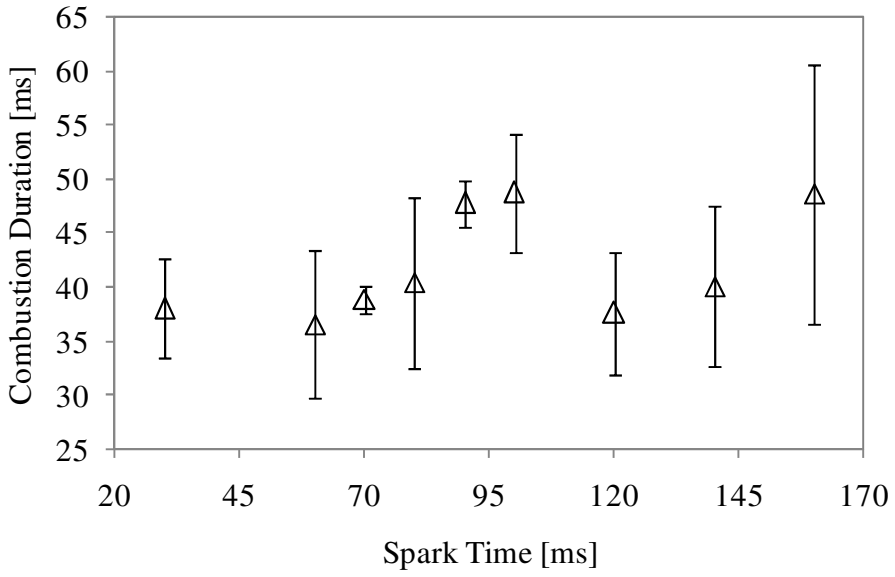

Figure 41 - Combustion Duration for $P_{RATIO} = 3$

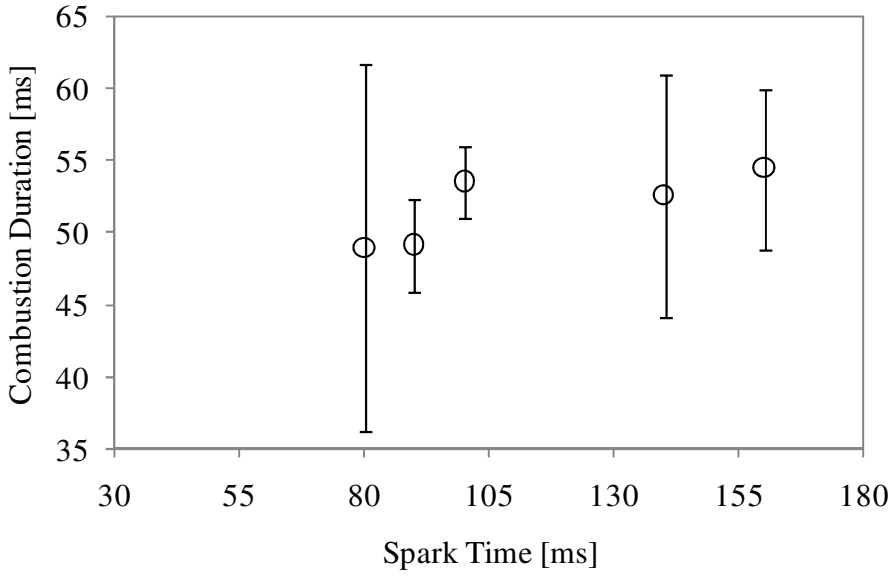

Figure 42 - Combustion Duration for $P_{RATIO} = 4$

In order to account for the reduced amount of fuel available to burn with increasing spark timing, the combustion duration is normalized with the integrated heat release. By normalizing t_{comb} with IHR, the heat release parameter becomes factored into the combustion duration time, leaving flame speed as the only significant parameter. The plot of normalized combustion duration in **Figure 43** shows an increasing trend with decreasing pressure ratio. This behaviour is expected, since the charge motion induced increases as the pressure ratio is increased. The study of PSC injection timing as a function of pressure ratio discussed earlier, found the following average injection durations: P_{RATIO} = 2 : 72.9 ms, P_{RATIO} = 3 : 90.9 ms, and P_{RATIO} = 4 : 115.3 ms. The normalized combustion duration is seen to increase for spark timings that are near or past the end of injection. As the pressure ratio was increased, the duration between end of injection and charge motion dissipation was observed to increase. At pressure ratios of two, the normalized combustion duration increases for spark timings greater than 60 ms (10 ms before the end of injection). For pressure ratios of three, the increase in normalized combustion duration begins 30 ms after the end of injection. At a pressure ratio of four, an increase in normalized combustion

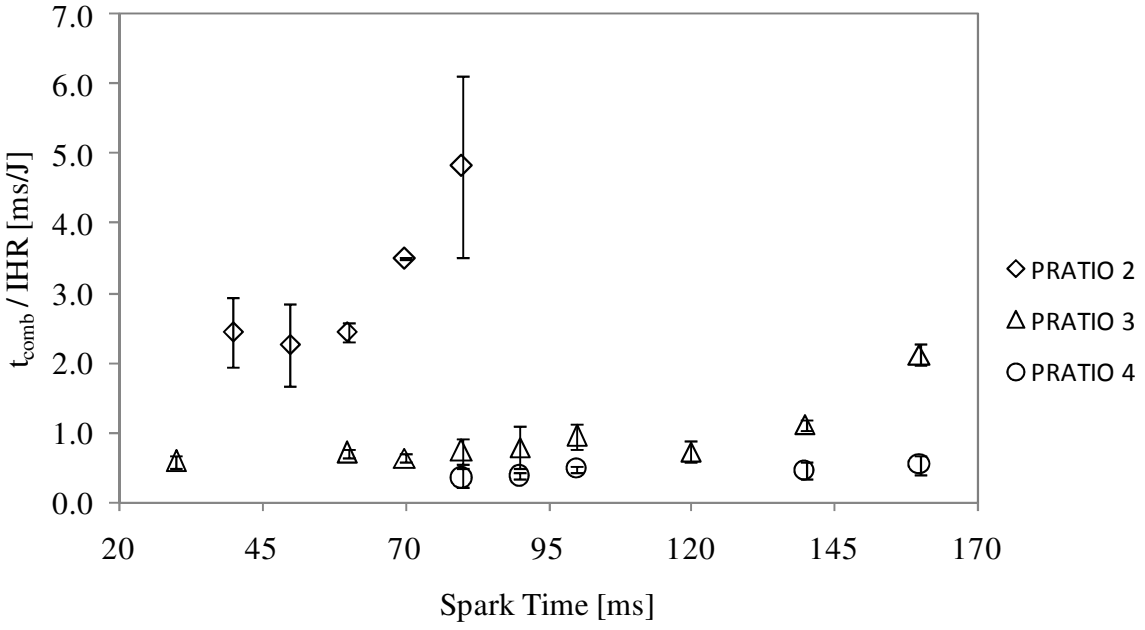

Figure 43 - Combustion Duration Normalized by Integrated Heat Release

duration is not detected, which may be due to the longer time required for the charge motion to dissipate.

4.2.4 Ignition Delay Study

The ignition delay shown in **Figure 44** has a definite increasing trend from pressure ratios of two. The uncertainties are also observed to increase with increasing pressure ratio, which make it more difficult to compare ignition delay times of $P_{RATIO} = 3$ to those of $P_{RATIO} = 4$. For $P_{RATIO} = 3$, the uncertainties have a decreasing trend with increasing spark timing. This is believed to be a result of the decreasing turbulence level with increasing spark timing. There are three spark timings (90 ms, 100ms and 160 ms) where the ignition delay at a pressure ratio of three is seen to be less than at a pressure ratio of four. At constant pressure ratio, the ignition delay remains statistically constant with spark timing at all pressure ratios. However, the uncertainty in ignition delay is seen to decrease with spark timing for pressure ratios of three. This trend could be explained by the decreasing level of turbulence near the spark plug electrodes as the fuel injection event nears completion.

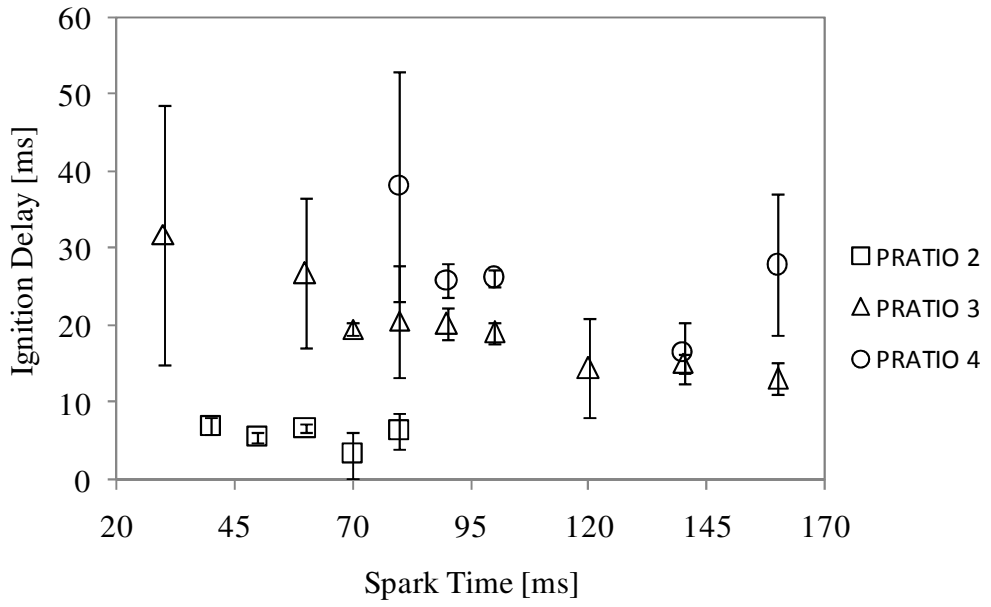

Figure 44 - Ignition Delay

The increased velocities near the spark plug electrodes at higher pressure ratios are believed to adversely affect the ignition delay. Ahmed *et al.* (2007) studied the effects of fuel and air velocity on the ignitability and flame stability of non-premixed flames. They concluded that the ignitability region is much narrower than the flame stability region when plotted against air-fuel velocity. Ahmed *et al.* attribute this finding to the fact that a flame edge is much more susceptible to straining out during the ignition phase than the established flame phase. Ahmed *et al.* propose that increased charge velocities cause an excessive reduction in flame front temperature, which can lead to extinction. The experiments conducted by Ahmed *et al.* support the argument that during the ignition phase, the developing PSC flame kernel is more susceptible to extinction at the increased velocities resulting from increased pressure ratio. Also, mixing air and fuel at a faster rate than the rate of reaction can result in localized flame extinction, which could explain the high ignition delay times at increased pressure ratio.

4.2.5 Fuel Jet and Flame Growth Study

Quantitative results attained from the pressure data were useful in determining parameters of interest such as integrated heat release, heat release rate, ignition delay, combustion duration and PSC injection duration. In order to try and explain fuel jet ignition difficulties and discrepancies between experiments, the Schlieren photographs were analyzed. The Schlieren photography was also used to generate some quantitative results, such as the PSC system injection timing parameters.

Two parameters of interest which could not be determined from the pressure data are the fuel jet and the flame kernel growth rates. The development of both fuel jet and flame kernel could be studied from the Schlieren Videos acquired; however, it is a tedious process requiring a manual frame by frame study. Instead, a systematic automated procedure was developed using a series of Matlab algorithms as listed below:

1) Acquire a set of 25 images prior to start of injection. Use average of these images as background. Resulting image is shown in **Figure 45** on the left.
2) Load frame under study, shown in **Figure 45** on the right.

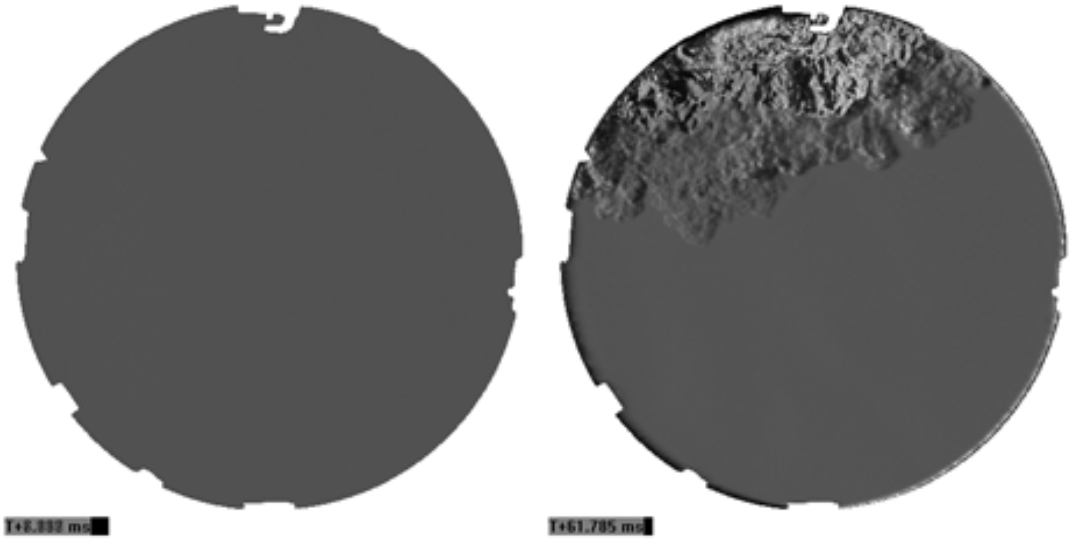

Figure 45 - Step 1, Background Image (Left); Step 2, Frame under Study (Right)

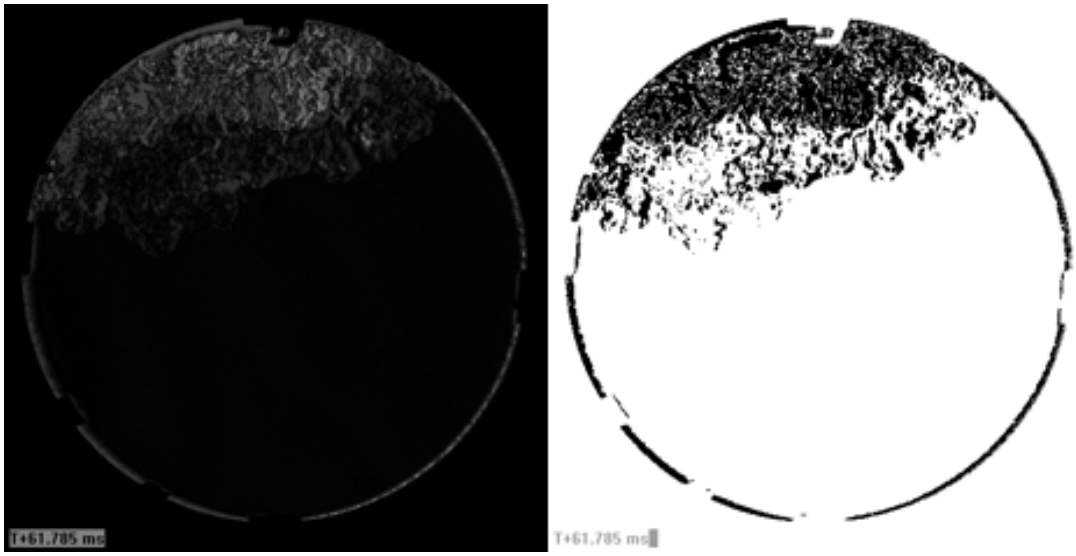

Figure 46 - Step 3, Subtracted Image (Left); Step 4, Binarized Image (Right)

3) Subtract the background image from the frame under study and subtract the frame under study from the background image. Add the two subtractions together to form the image shown in **Figure 46** on the left. The double subtraction was necessary to maintain the pixels in the image which were of lower value (i.e. more "black") than the background. Since the images were processed as 16bit rather than double precision matrices, pixel subtractions that yield negative numbers are truncated to a value of zero. A simplified example of this process is shown in **Figure 47**.

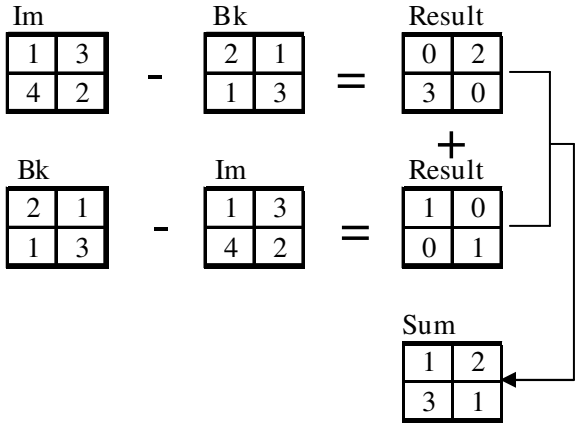

Figure 47 - Simplified Example of Image Subtraction and Addition

4) Select threshold value and binarize image. Set the grey pixels below the threshold to white and those above the threshold to black. The resulting image is shown in **Figure 46** on the right.
5) Count the black pixels in each progressive image and store values in an array.
6) Plot the pixel count array as a function of time for a plot of jet and flame kernel development.

The cold flow fuel jet development is shown as a function of time in **Figure 48**, for pressure ratios of two and three. In order to better illustrate the growth trend, the plot of $P_{RATIO} = 4$ has been omitted from **Figure 48** and is found in **Figure 53**. The Schlieren mercury vapour light is powered by an AC source, therefore some periodic amplitude fluctuations are observed in **Figure 48**. These fluctuations were found

to have a frequency of 120 Hz. This frequency is double that of the power source due to the process of background subtraction. Since the background is subtracted from the image of interest and the image of interest is also subtracted from the background, the luminosity fluctuations occur at twice the frequency of the light. These fluctuations are a result of the double subtraction between the image under study and the background, which has an effect of inverting the negative alternating signal and therefore doubling the peak to peak frequency. An FFT filter algorithm was written and applied to the raw curves in order to eliminate this noise. Both the raw and the FFT curves are shown in **Figure 48**.

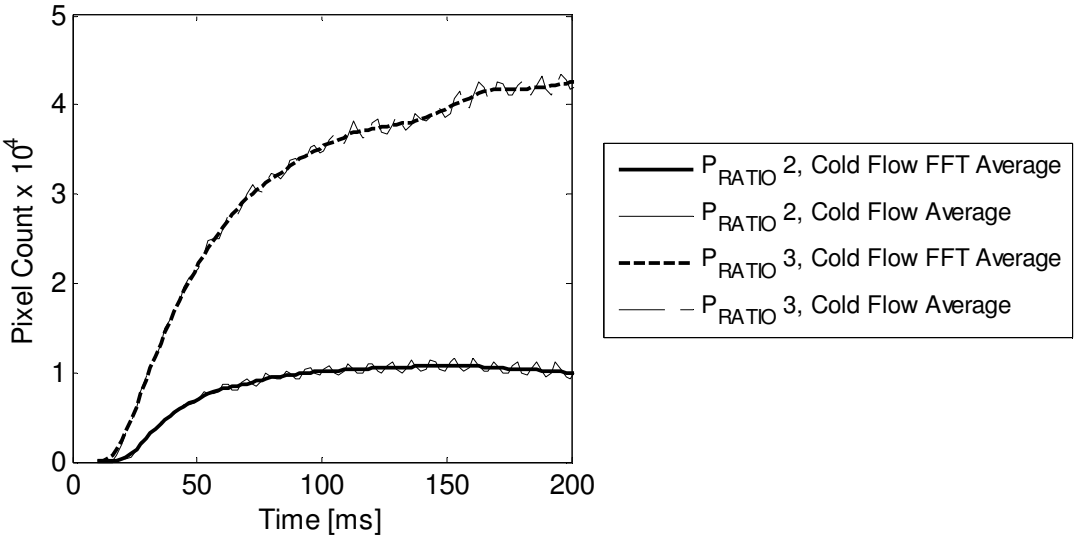

Figure 48 - Cold Flow Fuel Jet Development, P_{RATIO} 2 and P_{RATIO} 3

A threshold sensitivity study was conducted to determine if the general trends remain the same for different thresholds. The 16 bit images were processed with a threshold pixel value of 5000. A plot of a single reacting run is shown at different threshold values in **Figure 49**, where the pressure ratio is three and the spark time is 30 ms. The signal response in the time domain is the same for all three threshold cases. The slopes of the response curves decrease with increasing threshold value. Since this study is focused on relative differences between runs, changes in absolute values in the pixel count domain do not affect the results. Events such as first sighting of the jet plume and first detection of the flame kernel are

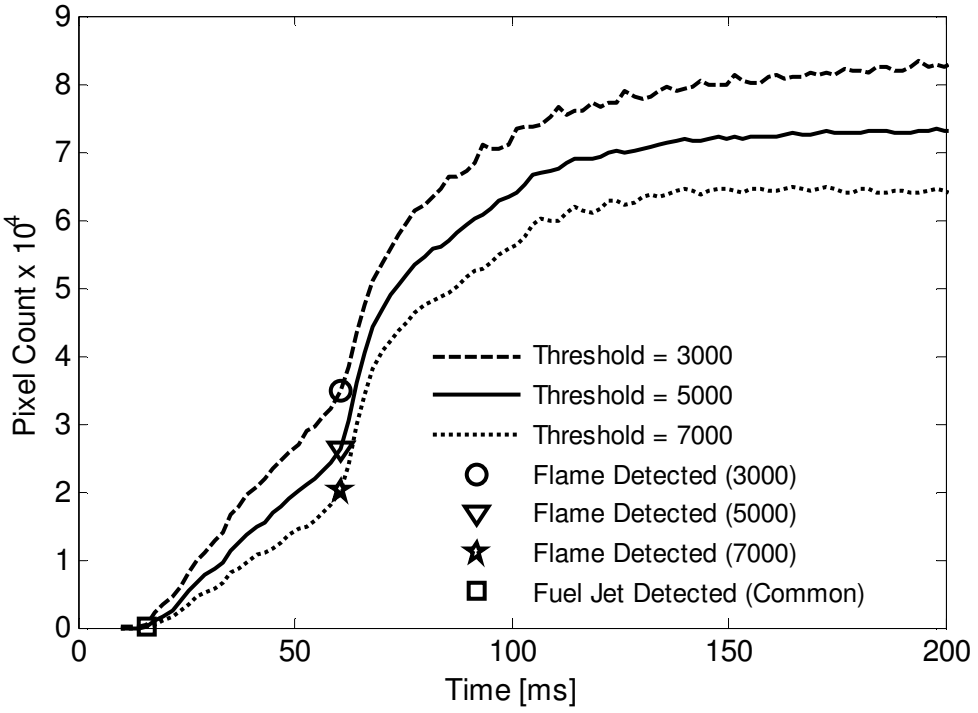

Figure 49 - Plots of Different Threshold Values for $P_{RATIO} = 3$, $T_S = 30$ ms

constant with varying threshold value. Thus, a threshold value of 5000 was maintained constant for processing all experiments.

The Schlieren visualization study conducted by Namazian et al. (1981) in an optically accessible ICE suggests that there is a temporal phase shift between the increase of the volume of gases inflamed and the mass fraction burned. Namazian found the lead time between volume fraction of flame developed and mass fraction burned to be about 10 CAD which corresponds to 1.2 ms in the internal combustion engine at 1380 rev/min. This trend was also apparent in the current study, where the flame kernel was observed to develop significantly before the $IHR_{5\%}$ point, which defines the start of ignition according to the pressure data. The images in **Figure 50** illustrate the flame kernel growth at the point of ignition ($IHR_{5\%}$) for each pressure ratio. According to the pressure data, only 5% of the fuel has burned at this point, however, it is clearly seen that the ratio of inflamed area to air-fuel area is much greater.

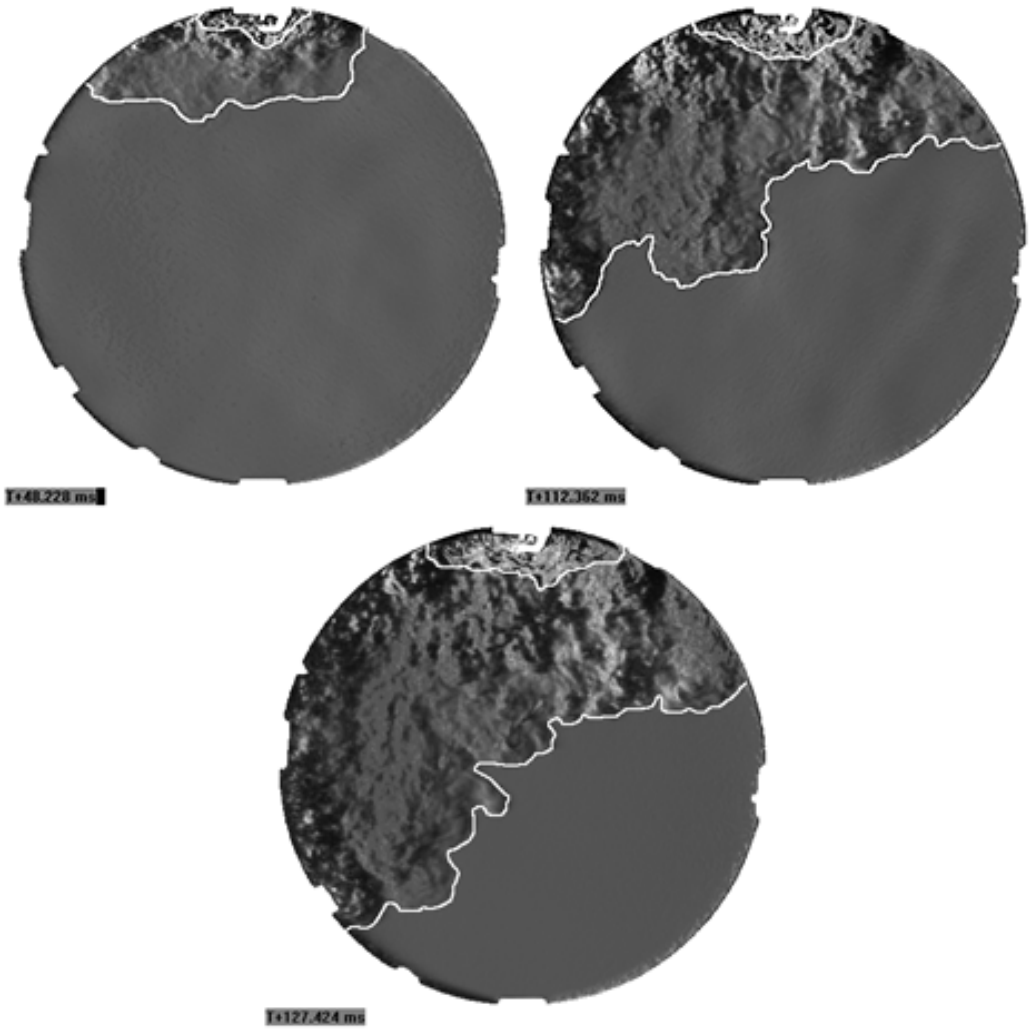

Figure 50 - Flame Kernel Development at the Point of Ignition

Figure 51, **Figure 52**, and **Figure 53** show plots of the total pixel count from the binarized Schlieren images as a function of time for pressure ratios of two, three and four respectively. The curve deviation from the cold flow case indicates the presence of a flame kernel. As the flame kernel grows, the pixel count steadily increases, until the flame growth process has finished. The slope of the flame growth line is proportional to the growth rate and thus the rate of heat release.

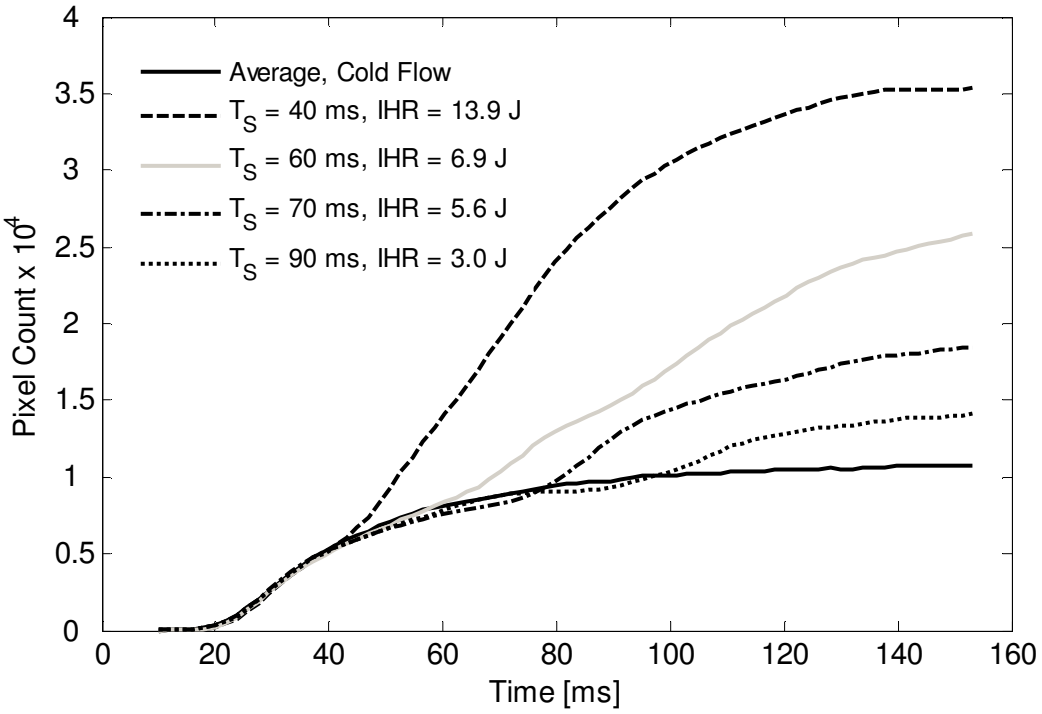

Figure 51 - Cold Flow and Combusting Runs as $P_{RATIO} = 2$

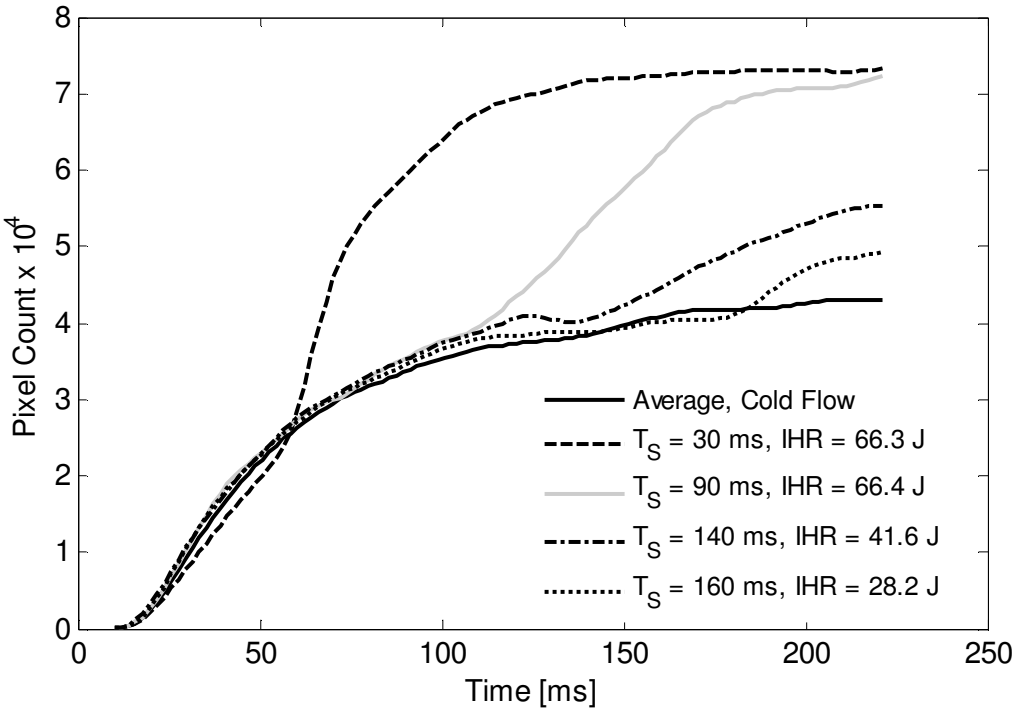

Figure 52 - Cold Flow and Combusting Runs at $P_{RATIO} = 3$

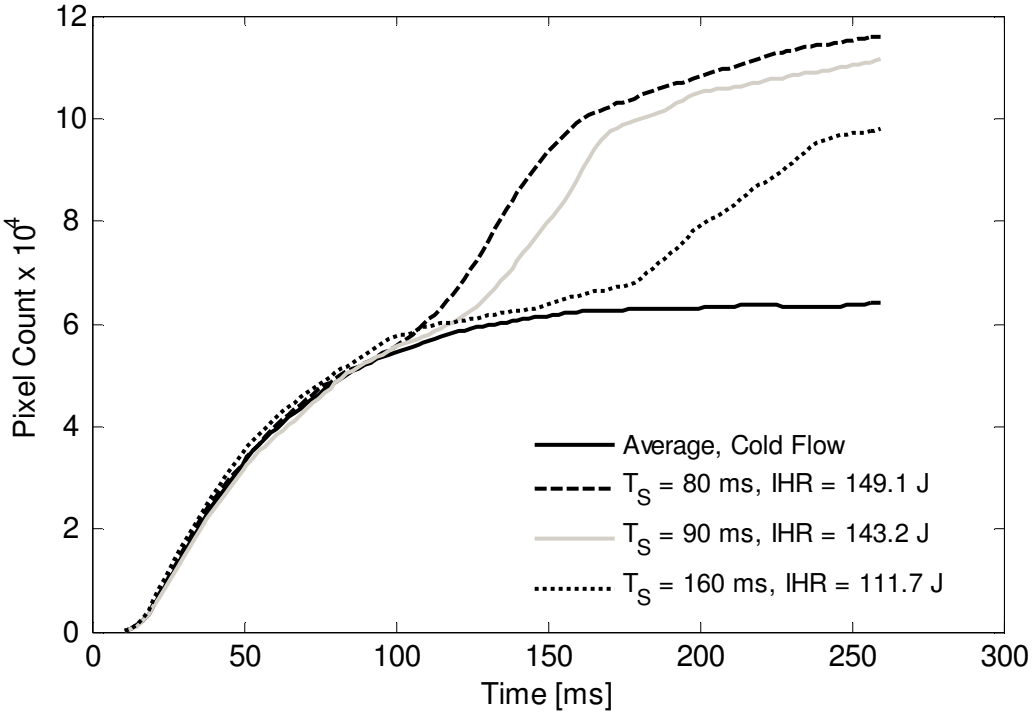

Figure 53 - Cold Flow and Combusting Runs at $P_{RATIO} = 4$

The slopes of the combusting runs, beginning with the point where the curves deviate from the cold flow average, have a decreasing trend with increasing spark timing. This trend is most noticeable for pressure ratios of two and three, which corresponds to the earlier findings that maximum HRR has a tendency to decrease with increasing spark timing. This decreasing trend is not as apparent for a pressure ratio of 4 (**Figure 53**) where there is little difference in the slope values of the flame kernel development.

The integrated heat release values determined from the pressure analysis are shown in the legends of **Figure 51**, **Figure 52** and **Figure 53**. These IHR values are proportional to the maximum pixel count observed for each experiment. For example, in **Figure 52**, the runs with spark timings of 30 ms and 90 ms release a net of 66 J each, whereas those with spark timings of 140 ms and 160 ms release less heat (41 J and 28 J). Although, both spark timings of 30 ms and 90 ms release the same amount of heat, it is evident from the slope of the curves that the 30 ms run releases heat at a faster rate than the run at 90 ms.

According to the combustion calculations performed based on the pressure data, the run with a 30 ms spark timing shown in **Figure 52** has a maximum HRR of 3.2 kW, while the run with a 90 ms spark timing has a maximum HRR of 2.1 kW.

4.3 SUMMARY OF COMBUSTION RESULTS

The highest frequency of combustion success occurred at a pressure ratio of three. The spark timing window that leads to successful combustion decreased with increasing pressure ratio. The spark timing retardation necessary for successful combustion was observed to increase with increasing pressure ratio.

Net integrated heat release values had a decreasing trend with increasing spark timing. Since the amount of fuel injected increased with increasing pressure ratio, net integrated heat release values also increased. Schlieren photographs of the combustion event indicate that the amount of unburned fuel increases with increasing spark timing. Heat release rates were observed to decrease with increased spark timing and increase with increasing pressure ratio.

While combustion duration had no specific trend with either spark timing or pressure ratio, the ratio of combustion duration to IHR showed a trend in both. The normalized combustion duration increased with spark timing for pressure ratios of two and three. This is likely due to the decrease in charge motion as the fuel injection nears completion at the later spark timings. Since charge motion increased with increasing pressure ratio, normalized combustion duration decreased.

Localized flame extinction may be responsible for the increased ignition delay as the pressure ratio was increased. The increased charge motion at higher pressure ratios causes increases in the rate of air-fuel

mixing. Since the reaction rates at the beginning of combustion are relatively slow, mixing rates exceed the reaction rates, resulting in flame quenching.

5. CONCLUSIONS AND RECOMMENDATIONS

Engine load control by varying the air/fuel ratio is a superior method to that of throttling because the pumping losses inherent to throttling are absent. Lean burn operation has been previously shown to be an effective way of increasing engine efficiency and decreasing engine emissions. The PSC concept has been previously shown to increase the lean operating limit of a spark ignited engine using natural gas (Reynolds, 2001). Stratified charge operation using PSC in conjunction with DI has been previously attempted (Gorby, 2007). The results of the previous DI study indicate that the PSC fuel injections failed to ignite in an air-only bulk charge. The research presented in this thesis was aimed at mapping out a range of injection pressure ratios and spark timings that lead to successful combustion of the PSC charge.

5.1 CONCLUSIONS

The experiments described herein were conducted in an optically accessible combustion bomb with a pressurized volume of 231.1 cubic centimetres. The PSC system utilized in the previous engine experiments was installed in the combustion bomb. The Schlieren imaging technique was used to study the PSC injection and combustion characteristics. An in-depth combustion analysis was performed based on the high speed pressure data acquired.

The main objectives of determining the range of pressure ratios and spark timings that lead to successful combustion were achieved. Combustion parameters were compared for all successful experiments. Cold flow studies were also performed to determine the PSC injection delay and duration. The PSC injection solenoid was characterized as a separate entity from the PSC system in order to get an understanding of its contributions to the total system delays. The following conclusions were made:

1. The PSC solenoid injection delay had a consistent average of 1.95 ms and was found to be independent of commanded injection duration. There is a linear response region, in the observed solenoid injection duration as a function of commanded injection duration, with a slope of 8.4. Commanded injection durations of 2.7 ms or higher showed no further increase in observed injection duration. Some solenoid chatter was apparent at CID values between 1.00 and 1.33 ms.

2. The PSC system injection delay was observed to decrease as the pressure ratio was increased. By using the Schlieren images, the average PSC system injection delays were determined to be 20.5 ms, 16.2 ms and 13.1 ms for pressure ratios of two, three and four respectively. These injection delay values are thought to be unacceptably long for the time scales present in an internal combustion engine.

3. The average PSC system injection durations were 52.4 ms, 74.7 ms and 102.1 ms for pressure ratios of two, three and four, which were several times higher than the commanded injection duration of 8 ms. This large discrepancy in duration is likely attributed to the plenum effects of the PSC system downstream of the injection solenoid. As stated in the previous point, at engine operating time scales, this discrepancy between commanded injection duration and observed injection duration needs to be addressed.

4. PSC charge ignition was attainable at all pressure ratios; however, a pressure ratio of three had the largest successful combustion frequency. The minimum spark timing that led to successful combustion increased with increasing pressure ratio, while the ignitable spark timing window decreased as the pressure ratio was increased.

5. Integrated heat release, heat release rate and ignition delay all varied with pressure ratio. Due to the increased amount of fuel injected at the higher pressure ratios, integrated heat release was

observed to increase as well. Heat release rate also increased with increasing pressure ratio due to the increasing charge motion present at higher pressure ratios. Ignition delay increased with increasing pressure ratio, most likely due to localized flame extinction during the reduced heat release rate of the ignition period.

6. Increasing the spark timing resulted in decreasing integrated heat release, release rate and increasing normalized combustion duration. The imaging results strongly suggest that the IHR decreased due to the increasing amount of fuel mixed beyond the lean flammability limit at the later spark timings. It is believed that HRR decreased and normalized combustion duration increased with increasing spark timing because the charge motion present at the earlier spark timings dissipated at the later spark timings.

7. The pixel count data resulting from the image binarization showed the same trends in integrated heat release and heat release rate as the pressure data. A temporal phase shift is observed between flame kernel development and integrated heat release, which is in agreement with previous research in an optically accessible engine.

5.2 RECOMMENDATIONS

The ability to ignite the PSC plume in a bulk charge of air demonstrates that further research is warranted with PSC and DI in a stratified charge engine. Since the previous engine studies were performed at constant pressure ratio, it is recommended that future studies consider varying this. These experiments have shown a significant variability of the discussed combustion parameters with pressure ratio. Since a pressure ratio of three showed the most promising results, it is suggested that future work focus on this pressure ratio as a starting point.

Since the current PSC system exhibits significantly longer injection durations than the commanded injection duration, it is suggested that an alternative method of injecting the fuel charge near the spark plug be investigated. The use of a fast acting direct injector with a minimal downstream plenum volume is desirable instead of the current injection solenoid.

The Schlieren imaging technique demonstrated the qualitative flow characteristics of the PSC jet plume. Further image processing such as image binarization leads to an understanding of trends in plume expansion rate and flame kernel development rate but did not yield any quantitative data. In order to gain a more in-depth understanding of the ignition probability at the spark plug electrodes, a method of quantifying the mixture fraction is highly desirable. A logical next step would be to implement a technique such as planar laser induced fluorescence (PLIF) to map out the ignitable regions of the PSC plume.

6. REFERENCES

Abata, D., 1986, "A Review of the Stratified Charge Engine Concept," *Automotive Engine Alternatives,* R. L. Evans, ed., Plenum Press, New York, pp. 1-36.

Ahmed, S. F., Balachandran, R., Marchione, T., Mastorakos, E., (2007) "Spark Ignition of Turbulent Nonpremixed Bluff-Body Flames", *Combustion and Flame*, Vol. 151, pp. 366-385

Alger, T., Wooldridge, S., Gallant, E., (2005), "The Effect of Fuel Injection on the Velocity Fluctuations in the Bowl of a DISI Engine." SAE Paper 2005-01-2102

Amann, C. A., 1986, "How Shall We Power Tomorrow's Automobile?," *Automotive Engine Alternatives,* R. L. Evans, ed., Plenum Press, New York, pp. 37-82.

Bowker, Albert H., Lieberman, Gerald J., *Engineering Statistics,* 2nd Edition, (1972), Prentice-Hall Inc. NJ, ISBN 0-13-279455-1

Brown G (2003). "Performance of a Partially Stratified-Charge Gasoline Engine" University of British Columbia, Canada, M.A.Sc dissertation

Dahm, Werner J.A., and Dimotakis, Paul E., (1990) "Mixing at Large Schmidt Number in the Self-Similar Far Field of Turbulent Jets", *Journal of Fluid Mechanics*, Vol. 217, pp. 299-330

Evans (2000), "Control Method for Spark-Ignition Engines", United States Patent No. 6,032,640, Issued March 2000

Gorby D (2007). "An evaluation of Partially Stratified Charge Ignition in a Direct Injection Natural Gas Engine", University of British Columbia, Canada, M.A.Sc dissertation

Heywood, J.B., *Internal Combustion Engine Fundamentals*, *(*1988), McGraw-Hill, New York NY, ISBN 0-07-100499-8

Huang, Z., Shiga, S., Ueda, T., Nakamura, H., Ishima, T., Obokata, T., Tsue, M., Kono, M., (2003), "Combustion Characteristics of Natural-Gas Direct-Injection Combustion Under Various Fuel

Injection Timings", *Proc. Instn Mech. Engrs.*, Vol. 217 Part D: J. Automobile Engineering pp. 393-401

Hill, Phillip G., and Oulette, P., (1999), "Transient Turbulent Gaseous Fuel Jets for Diesel Engines." *Journal of Fluids Engineering,* Vol. 121, pp. 93-101

Holman, J. P., 2002, "Heat Transfer", 9th Ed., McGraw Hill, ISBN 0-07-240655-0

Kitagawa, T., Kido, H., Kim, K., Koga, H., Fujioka, K., (2002), "Flame Propagation into Lean Region in Stratified Methane Mixture." SAE Paper 2002-01-2693

Kubseh, John T., (2001), "Development of a Throttleless Natural Gas Engine" SAE Paper 2001-01-2522

Lahbabi, Fatima Z., Borée, Jacques, Nuglisch, Hans J., and Charnay, Georges, (1993), "Analysis of Starting and Steady Turbulent Jets by Image Processing Techniques." *Experimental and Numerical Flow Visualization,* ASME FED, Vol. 172, pp. 315-321

Mi, J., Nathan, G. J., Nobes, D. S., (2001), "Mixing Characteristics of Axisymmetric Free Jets From a Contoured Nozzle, an Orifice Plate and a Pipe." *Journal of Fluids Engineering,* Vol. 123, pp. 878-883

Namazian, M., Hansen, S., Lyford-Pike, E., Sanchez-Barsse, J., Heywood, J., Rife, J., (1981), "Schlieren Visualization of the Flow and Density Fields in the Cylinder of a Spark Ignition Engine." SAE Paper 800044

Navidi, W., 2006, "Statistics for Engineers and Scientists", 1st Ed., McGraw Hill, ISBN 0-07-255160-7

Oulette, P., (1996), "Direct Injection of Natural Gas for Diesel Engine Fuelling," PhD thesis, University of British Columbia

Pischinger, S., Umierski, M., Hüchtebrock, B., (2003), "New CNG Concepts for Passenger Cars: High Torque with Superior Fuel Consumption." SAE Paper 2003-01-2264

Reynolds, C.C.O., (2001), "Performance of a Partially Stratified-Charge Natural Gas Engine", University of British Columbia, Canada, M.A.Sc. dissertation

Settles, G. S., *Schlieren and Shadowgraph Techniques*, (2001), 1st Ed., Springer Berlin Heidelberg NY, ISBN 3-540-66155-7

Shapiro, A. H., *The Dynamics and Thermodynamics of Compressible Fluid Flow*, (1953), Volume I, John Wiley and Sons, ISBN 0-471-06691-5

Stone, Richard, *Introduction to Internal Combustion Engines*, 3rd Edition, (1999), Society of Automotive Engineers, Warrendale PA, ISBN 0-7680-0495-0

Terasen Gas Inc., World Wide Web, Cited August 15, 2008: *http://www.terasengas.com/_AboutNaturalGas/FactsandInformation/GasFacts/DetailedGasFacts.htm*

Ting, D. S. –K., and Checkel, M. D., (2001), "The Effect of Mean Turbulent Strain Rate on the Flame Speed of Premixed, Growing Flames." *Journal of Engineering for Gas Turbines and Power*, Vol. 123, pp. 175 - 181

White, Frank M., *Fluid Mechanics*, (1999), 4th Ed., McGraw Hill, ISBN 0-07-069716-7

APPENDIX A: EXPERIMENT NUMBERS

Pressure Ratio	Spark Timing [ms]												
	10	20	30	40	50	60	70	80	90	100	120	140	160
2	**1**	**2**	**3**	**4**	**5**	**6**	**7**	**8**	**9**	**10**	**-**	**-**	**-**
	31	**32**	**33**	**34**	**35**	**36**	**37**	**38**	**39**	**40**	**-**	**-**	**-**
	61	**62**	**63**	**64**	**65**	**66**	**67**	**68**	**69**	**70**	**-**	**-**	**-**
3	**11**	**12**	**13**	**14**	**15**	**16**	**17**	**18**	**19**	**20**	**101**	**102**	**103**
	41	**42**	**43**	**44**	**45**	**46**	**47**	**48**	**49**	**50**	**107**	**108**	**109**
	71	**72**	**73**	**74**	**75**	**76**	**77**	**78**	**79**	**80**	**113**	**114**	**115**
			92				**91**						
			93										
			94										
			95										
4	**21**	**22**	**23**	**24**	**25**	**26**	**27**	**28**	**29**	**30**	**104**	**105**	**106**
	51	**52**	**53**	**54**	**55**	**56**	**57**	**58**	**59**	**60**	**110**	**111**	**112**
	81	**82**	**83**	**84**	**85**	**86**	**87**	**88**	**89**	**90**	**116**	**117**	**118**

Experiment Order of Execution: (R - Run #, E - Exp #)

R	E	R	E	R	E	R	E	R	E	R	E
1	**46**	21	**66**	41	**67**	61	**6**	81	**71**	101	**112**
2	**31**	22	**47**	42	**43**	62	**33**	82	**11**	102	**106**
3	**84**	23	**65**	43	**86**	63	**34**	83	**73**	103	**104**
4	**2**	24	**50**	44	**27**	64	**88**	84	**90**	104	**115**
5	**22**	25	**18**	45	**39**	65	**62**	85	**61**	105	**108**
6	**69**	26	**35**	46	**83**	66	**55**	86	**45**	106	**118**
7	**15**	27	**1**	47	**74**	67	**19**	87	**64**	107	**102**
8	**14**	28	**32**	48	**70**	68	**37**	88	**51**	108	**116**
9	**38**	29	**40**	49	**4**	69	**59**	89	**23**	109	**107**
10	**76**	30	**29**	50	**21**	70	**26**	90	**42**	110	**109**
11	**81**	31	**48**	51	**3**	71	**60**	91	**91**	111	**110**
12	**24**	32	**54**	52	**7**	72	**52**	92	**92**	112	**114**
13	**72**	33	**12**	53	**63**	73	**77**	93	**93**	113	**113**
14	**41**	34	**28**	54	**79**	74	**16**	94	**94**		
15	**8**	35	**75**	55	**68**	75	**85**	95	**95**		
16	**56**	36	**5**	56	**9**	76	**58**	96	**101**		
17	**30**	37	**17**	57	**10**	77	**80**	97	**103**		
18	**49**	38	**13**	58	**78**	78	**89**	98	**111**		
19	**44**	39	**36**	59	**25**	79	**87**	99	**105**		
20	**20**	40	**57**	60	**82**	80	**53**	100	**117**		

APPENDIX B: SELECT IMAGES FOR COMBUSTING RUNS

The following is a compilation of images corresponding to the time of spark (left), time of max HRR (middle) and end of combustion (right) for the experiments that were successfully ignited.

P_{RATIO} = 2, T_S = 40 ms → **Exp 4**

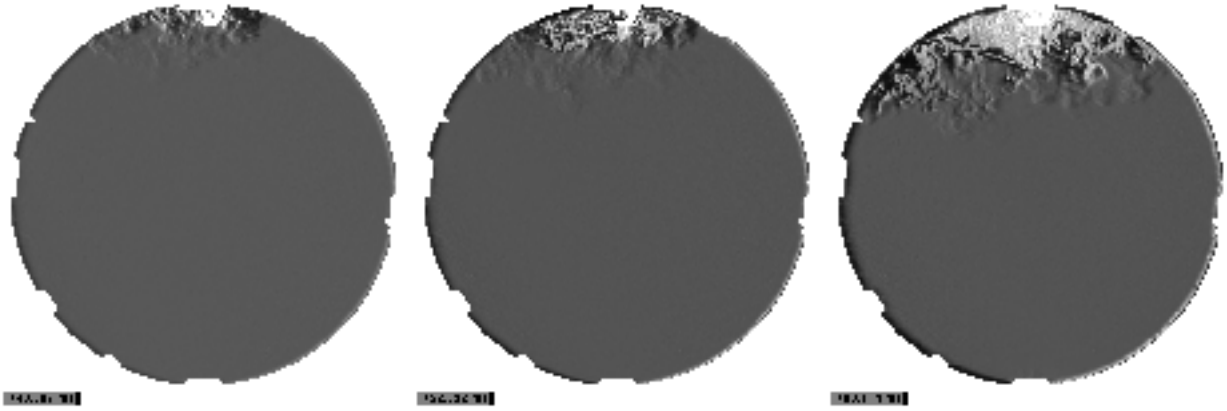

P_{RATIO} = 2, T_S = 40 ms → **Exp 34**

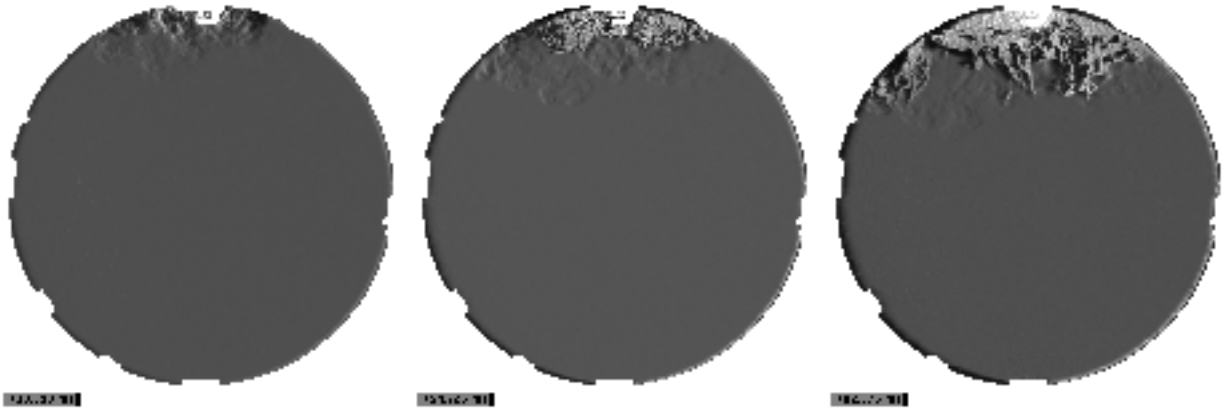

P_{RATIO} = 2, T_S = 40 ms → **Exp 64**

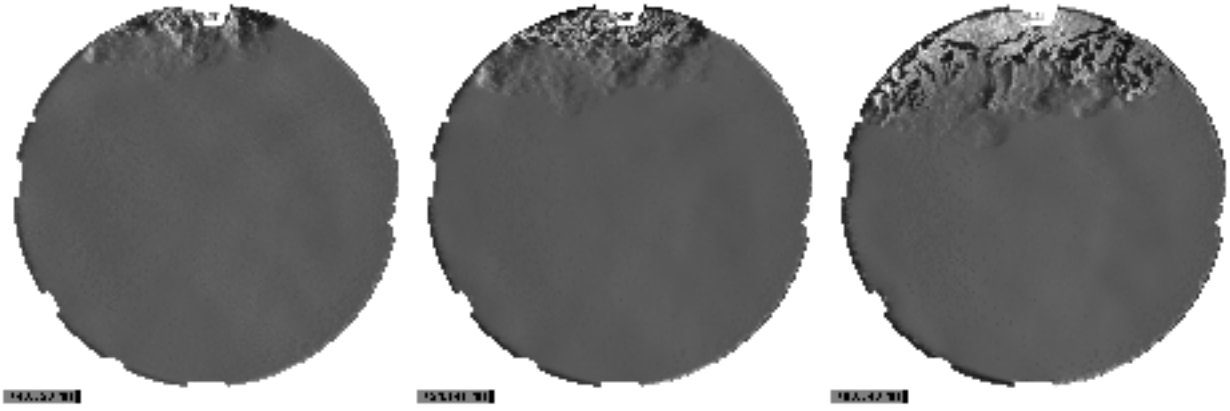

P_{RATIO} = 2, T_S = 50 ms → **Exp 5**

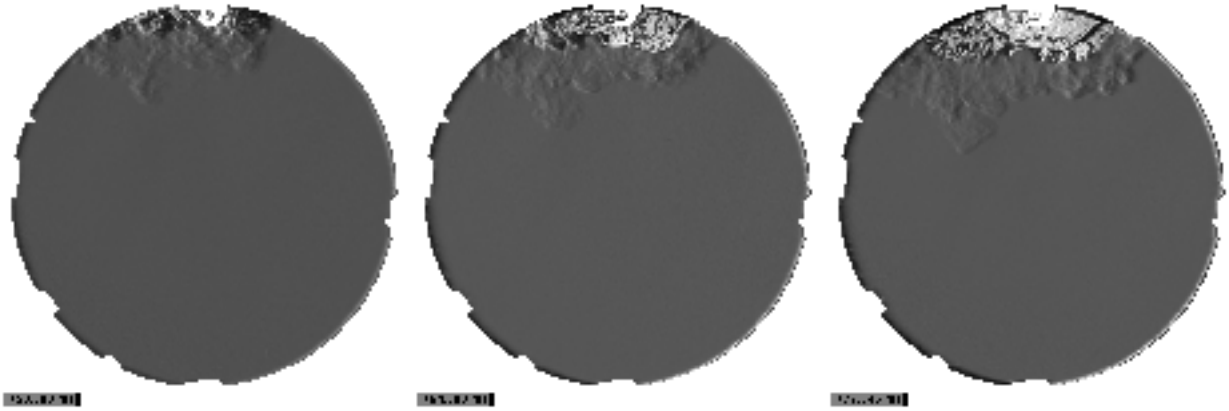

P_{RATIO} = 2, T_S = 50 ms → **Exp 35**

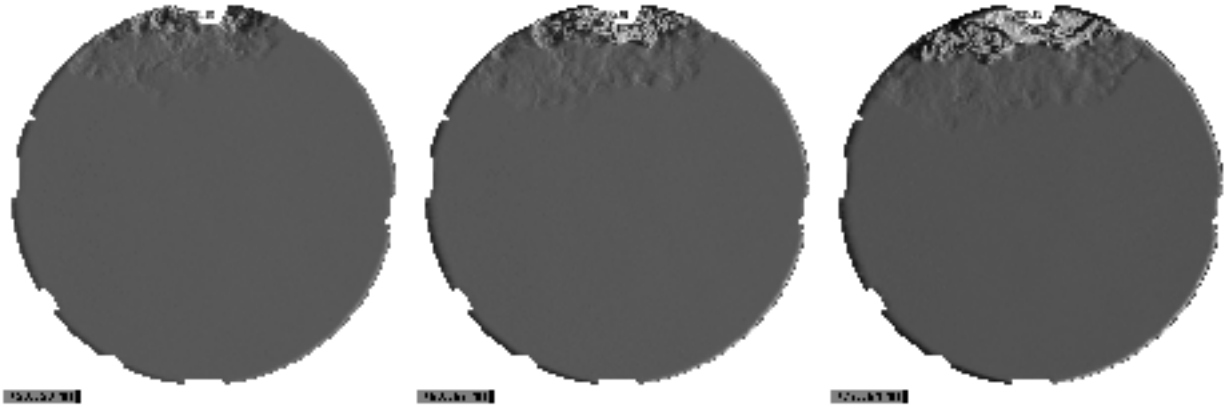

P_{RATIO} = 2, T_S = 50 ms → **Exp 65**

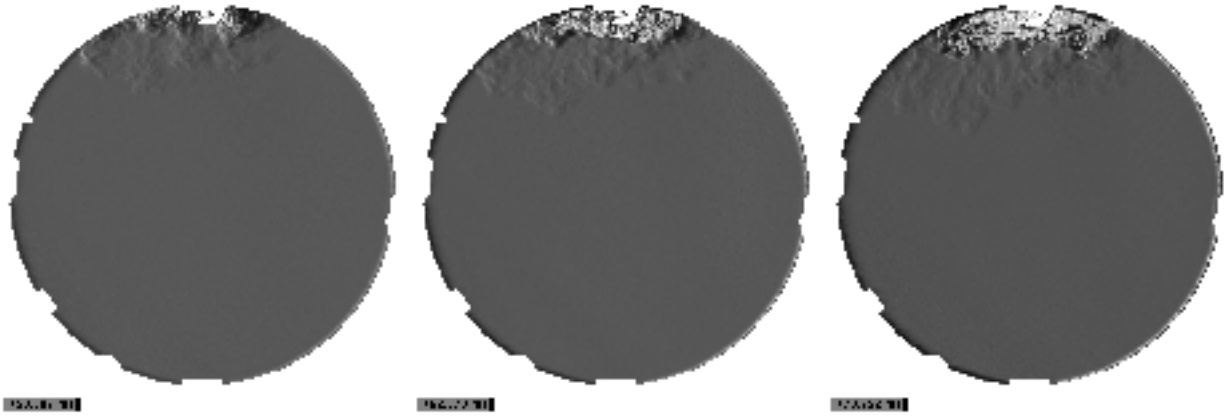

P_{RATIO} = 2, T_S = 60 ms → **Exp 6**

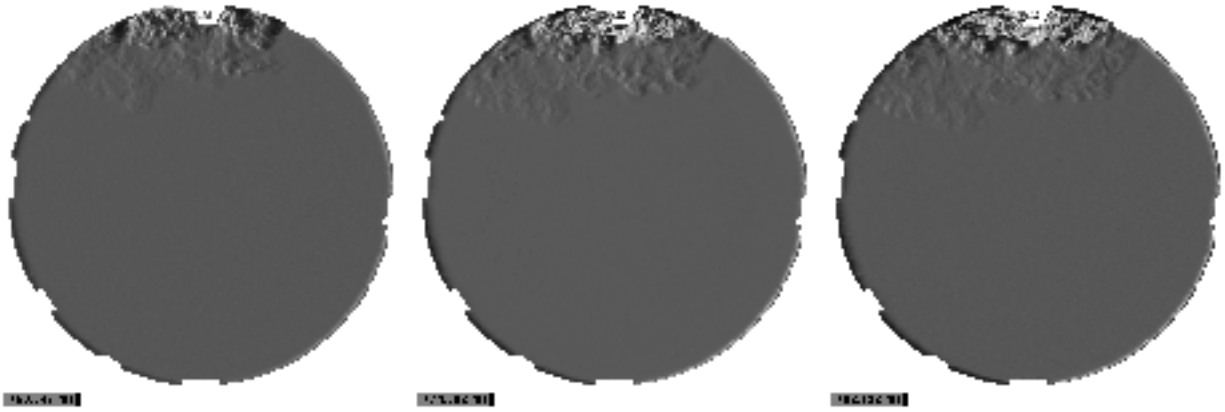

P_{RATIO} = 2, T_S = 60 ms → **Exp 36**

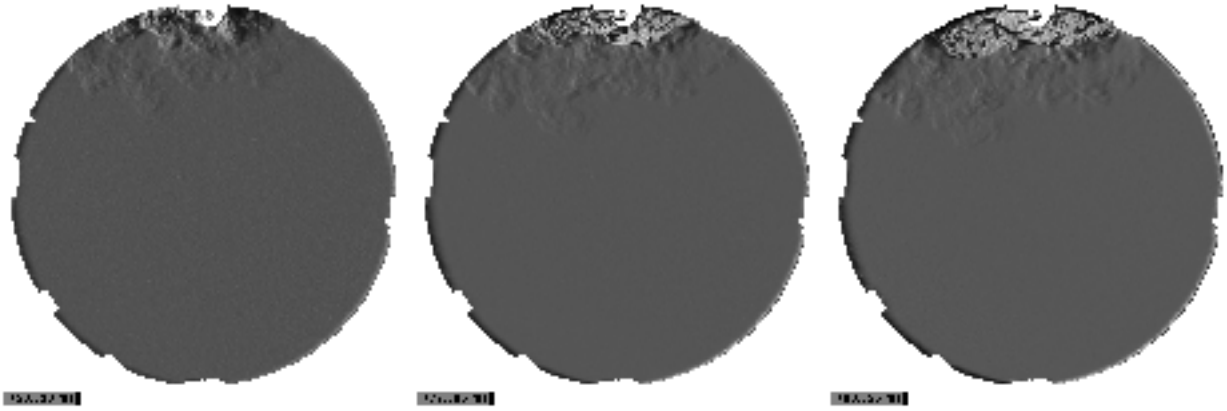

P_{RATIO} = 2, T_S = 60 ms → **Exp 66**

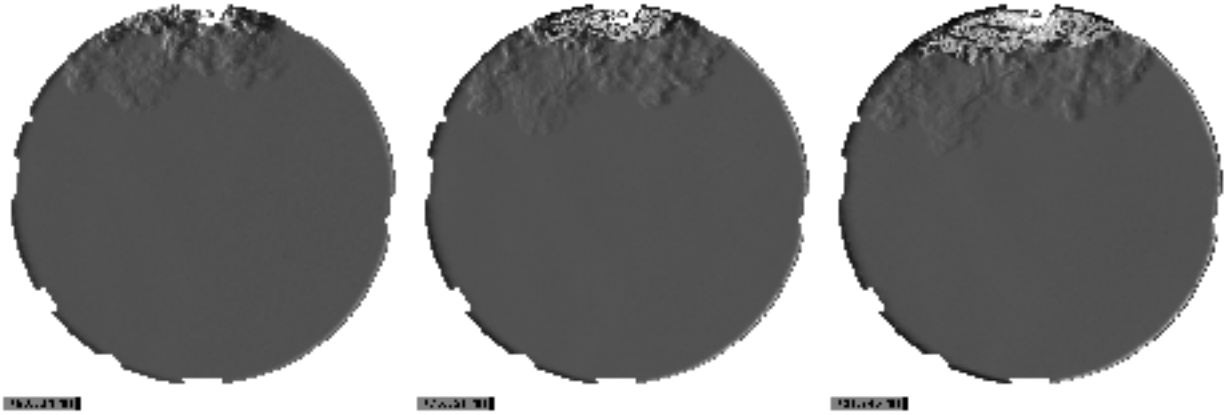

P_{RATIO} = 2, T_S = 70 ms → **Exp 37**

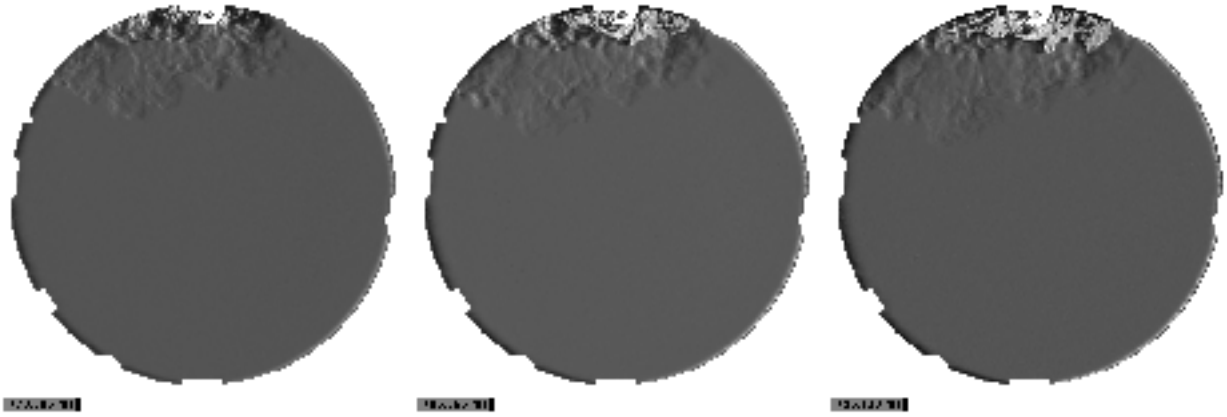

P_{RATIO} = 2, T_S = 70 ms → **Exp 67**

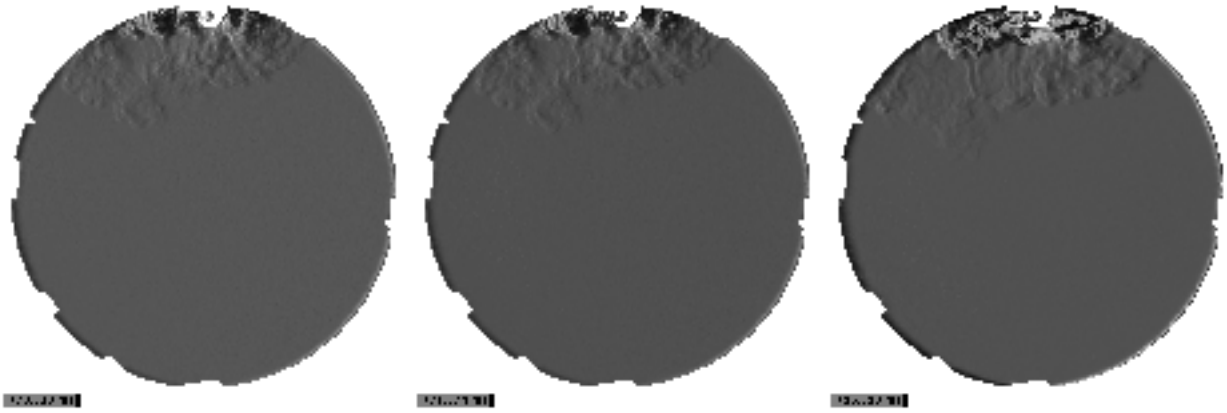

P_{RATIO} = 2, T_S = 80 ms → **Exp 8**

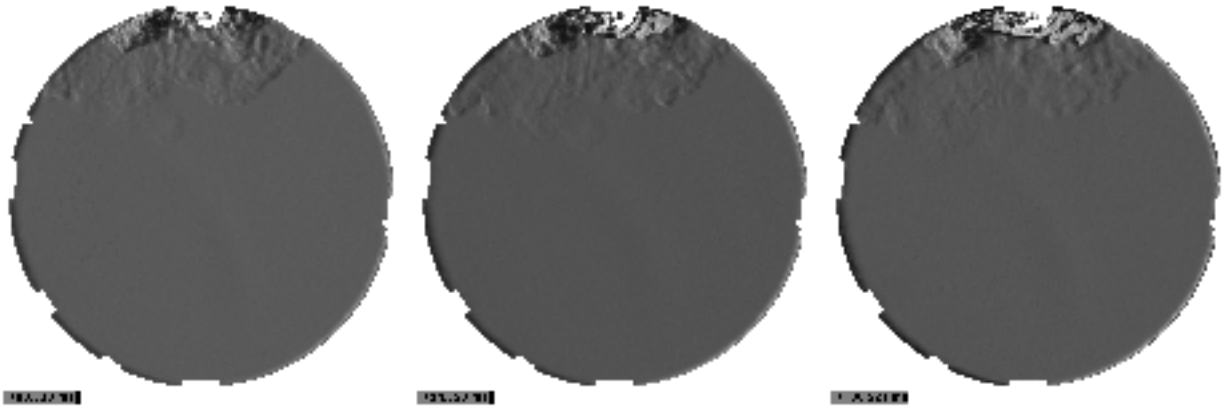

P_{RATIO} = 2, T_S = 80 ms → **Exp 38**

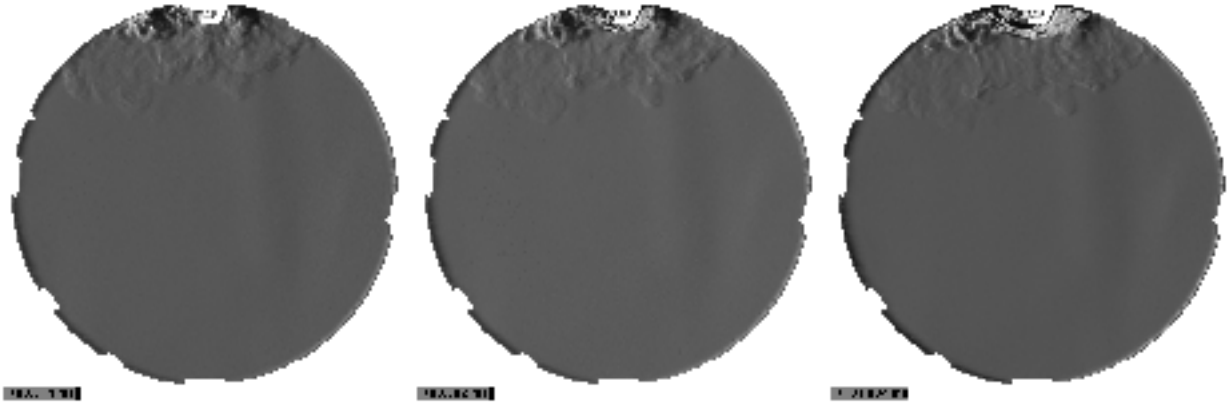

P_{RATIO} = 2, T_S = 90 ms → **Exp 9**

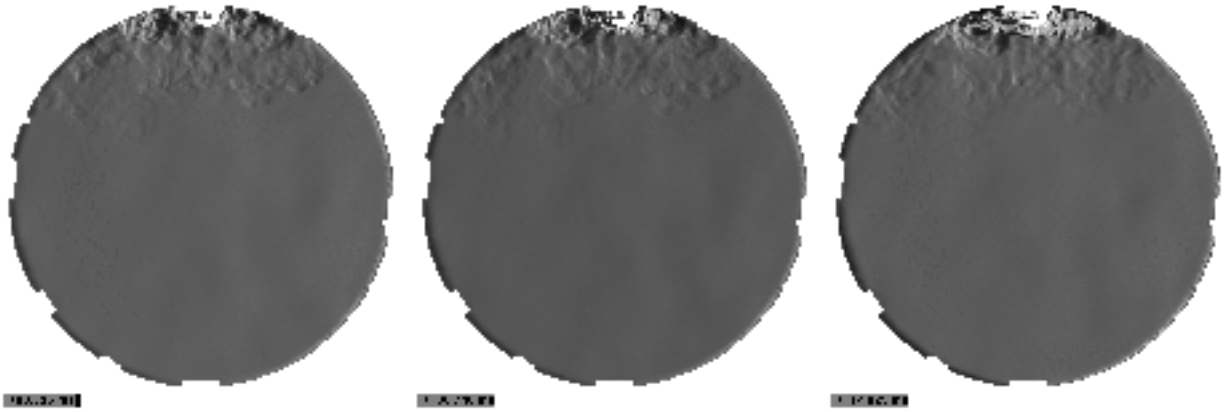

P_{RATIO} = 2, T_S = 100 ms → **Exp 10**

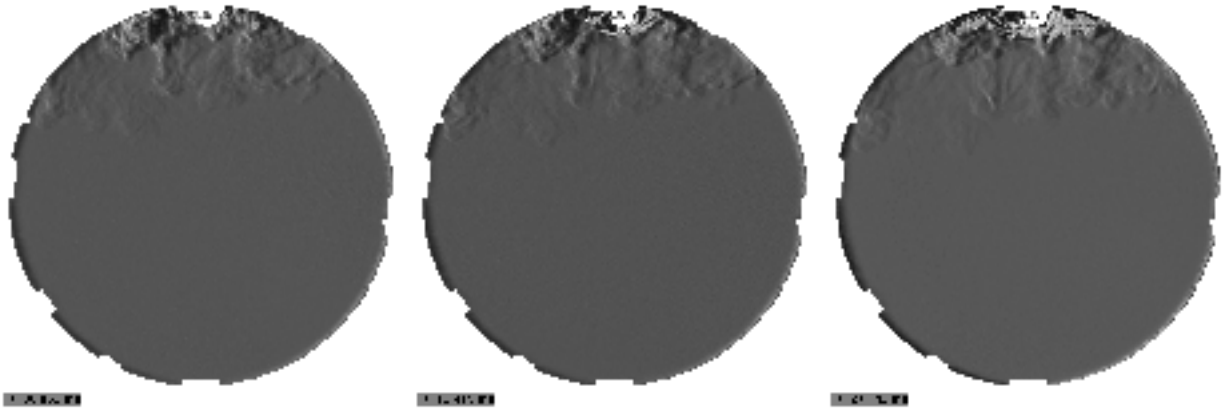

P_{RATIO} = 3, T_S = 30 ms → **Exp 43**

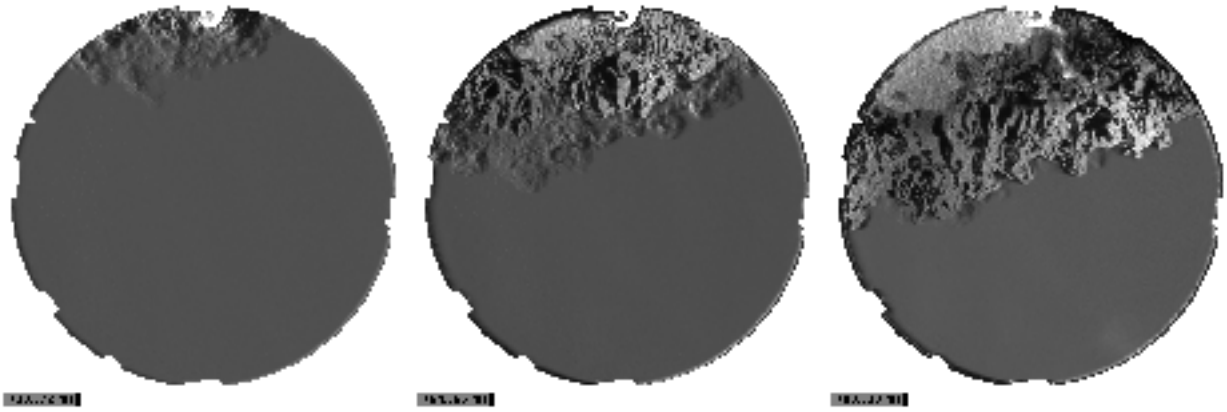

P_{RATIO} = 3, T_S = 30 ms → **Exp 73**

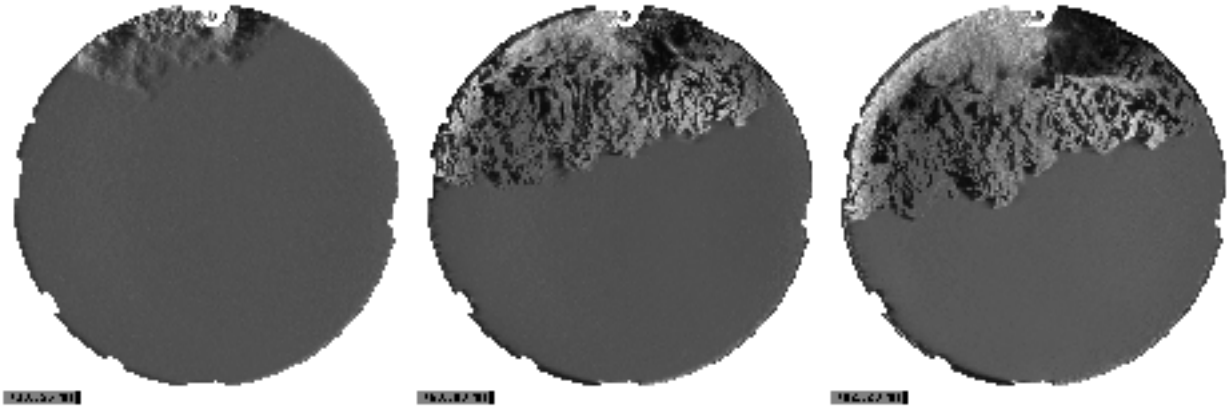

P_{RATIO} = 3, T_S = 30 ms → **Exp 91**

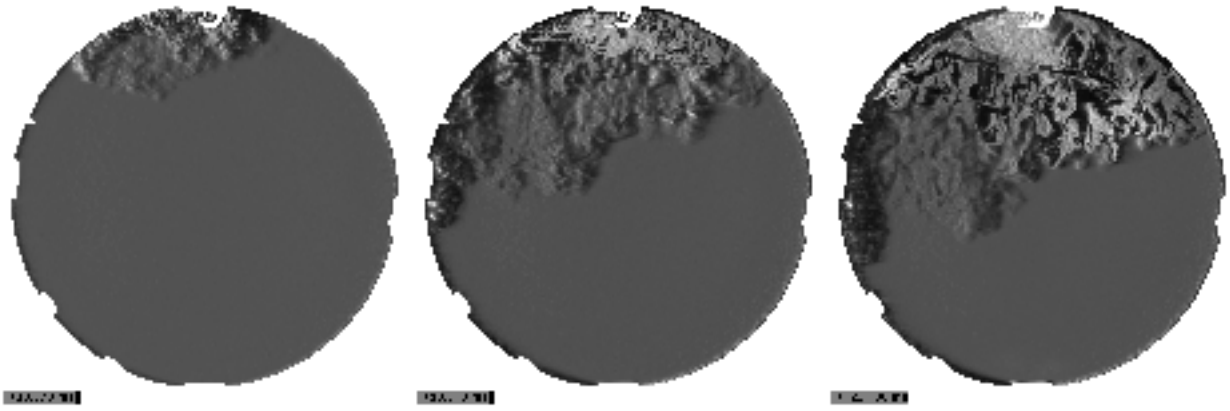

P_{RATIO} = 3, T_S = 30 ms → **Exp 92**

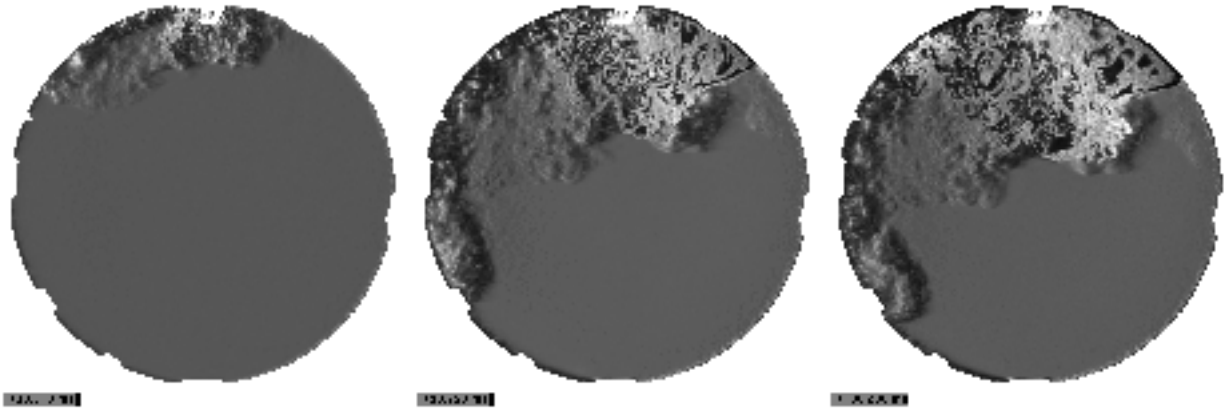

P_{RATIO} = 3, T_S = 30 ms → **Exp 95**

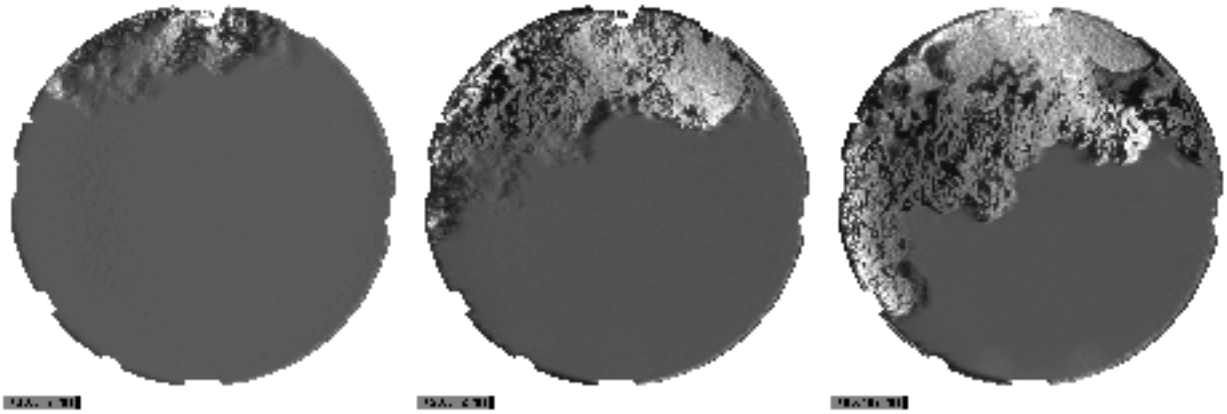

P_{RATIO} = 3, T_S = 50 ms → **Exp 15**

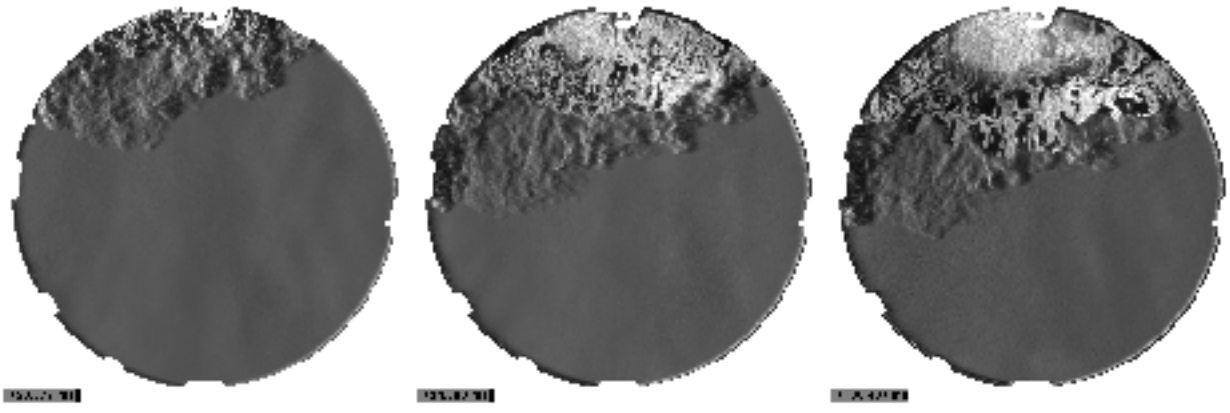

P_{RATIO} = 3, T_S = 60 ms → **Exp 16**

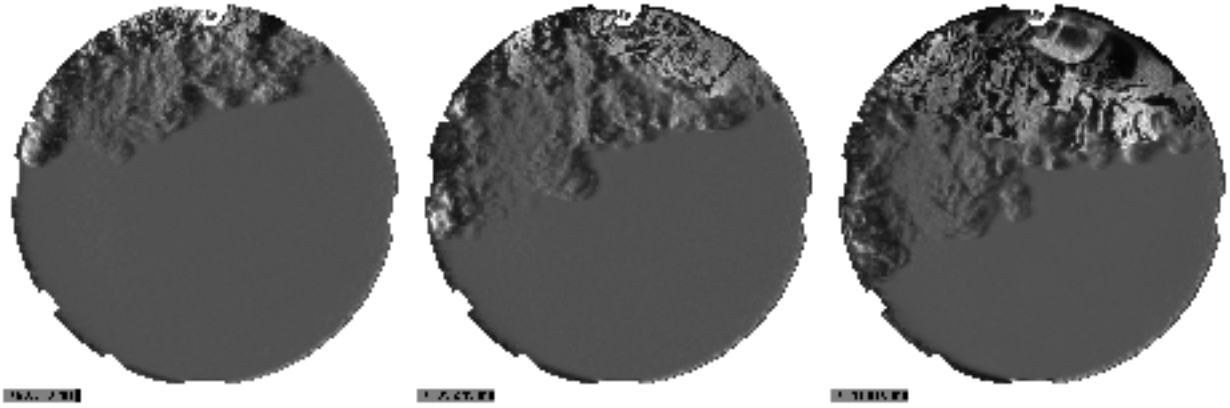

P_{RATIO} = 3, T_S = 60 ms → **Exp 46**

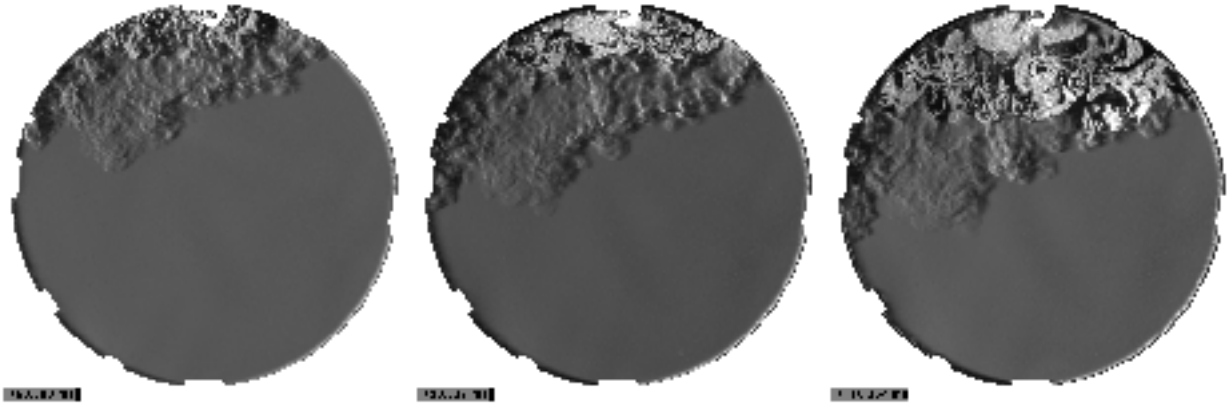

P_{RATIO} = 3, T_S = 60 ms → **Exp 76**

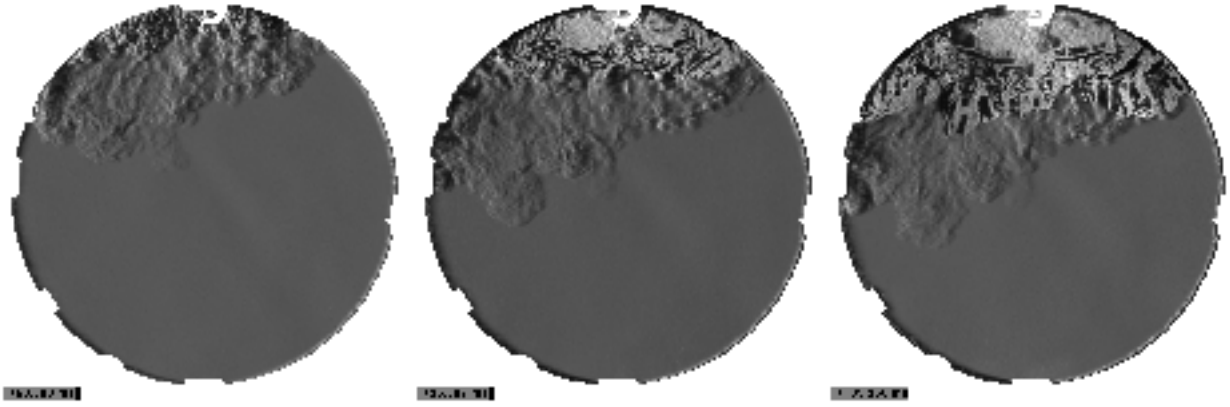

P_{RATIO} = 3, T_S = 70 ms → **Exp 17**

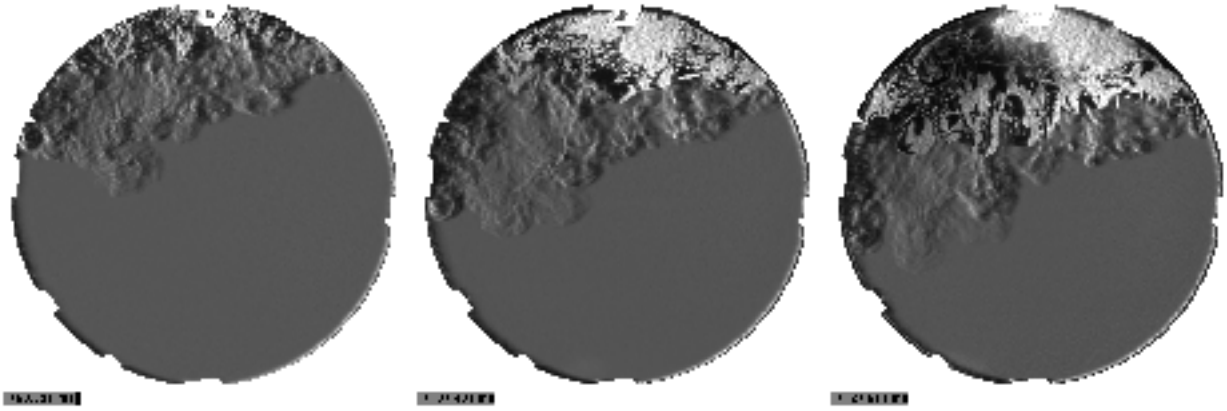

P_{RATIO} = 3, T_S = 70 ms → **Exp 47**

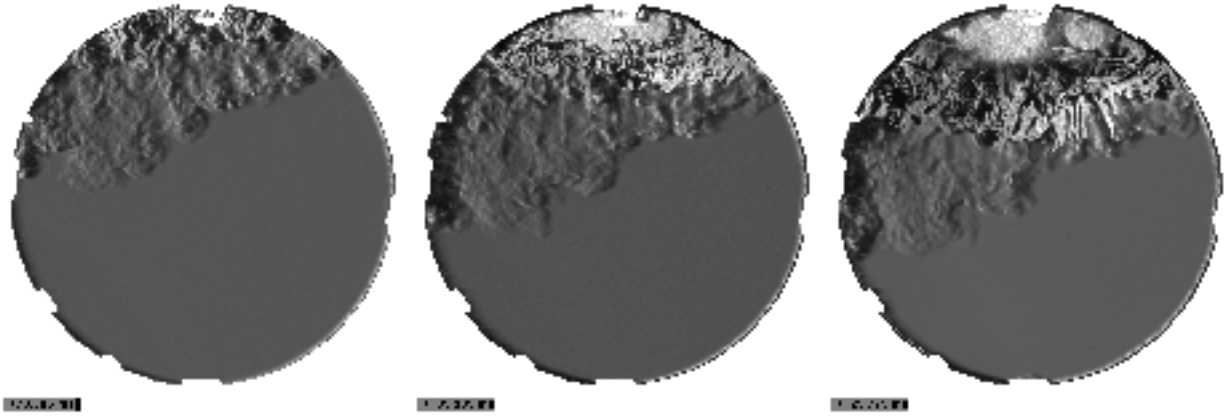

P_{RATIO} = 3, T_S = 70 ms → **Exp 77**

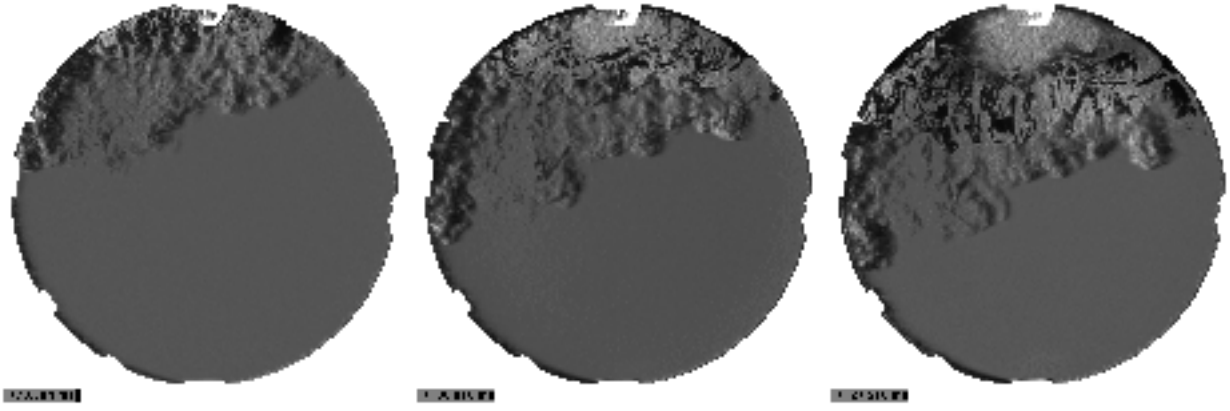

P_{RATIO} = 3, T_S = 80 ms → **Exp 18**

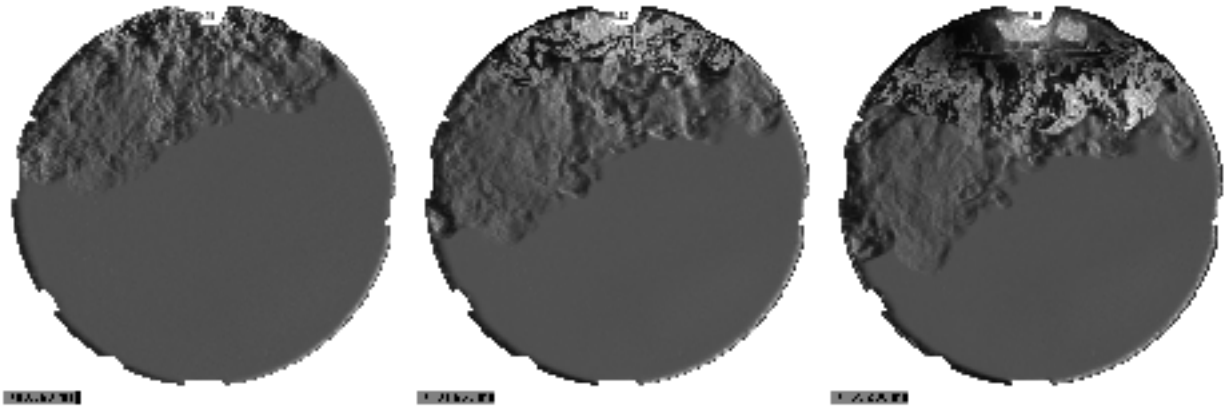

P_{RATIO} = 3, T_S = 80 ms → **Exp 48**

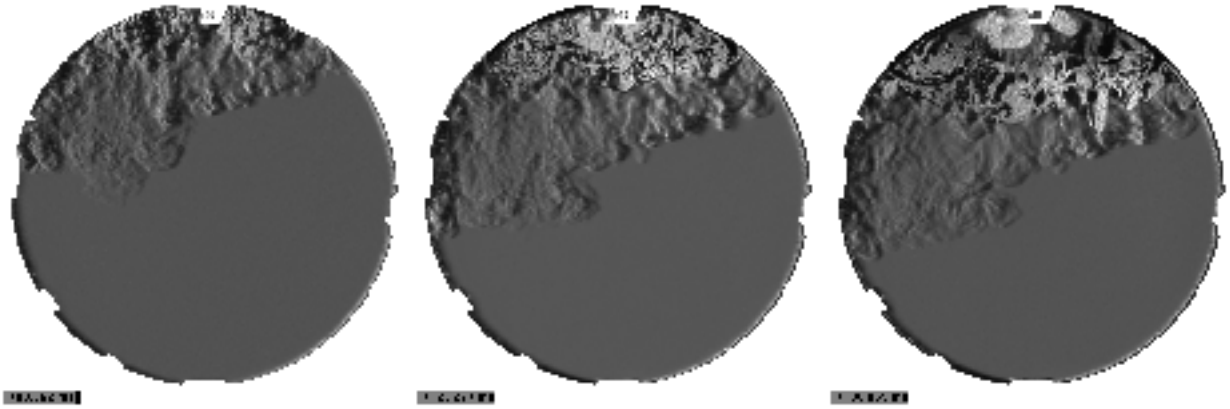

P_{RATIO} = 3, T_S = 80 ms → **Exp 78**

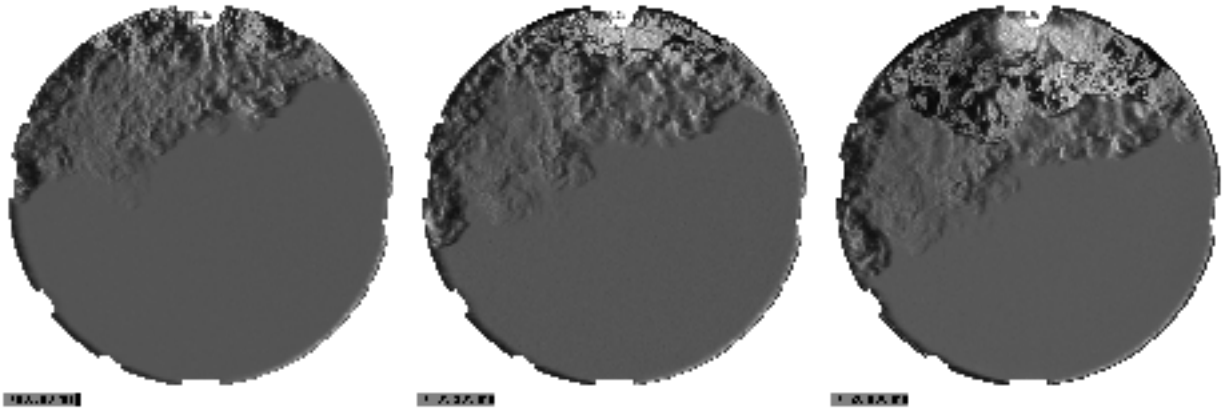

P_{RATIO} = 3, T_S = 90 ms → **Exp 19**

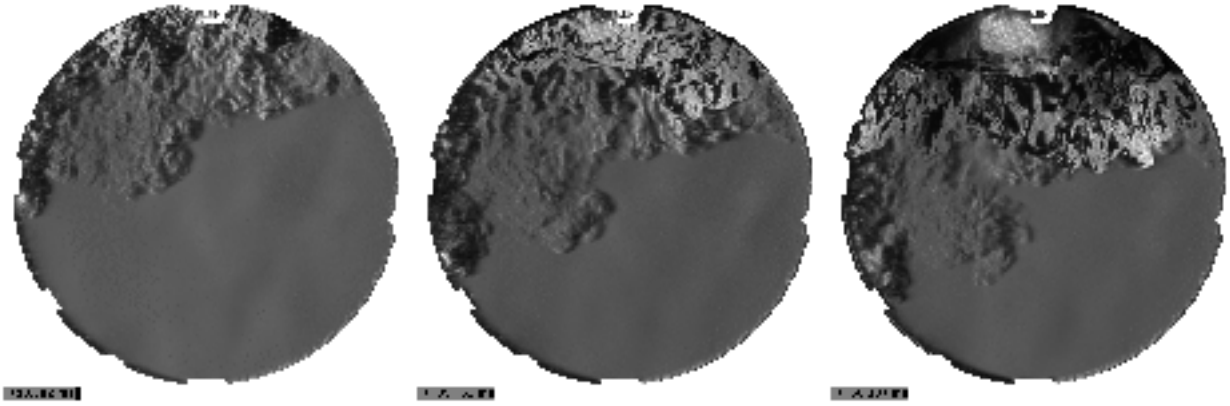

P_{RATIO} = 3, T_S = 90 ms → **Exp 49**

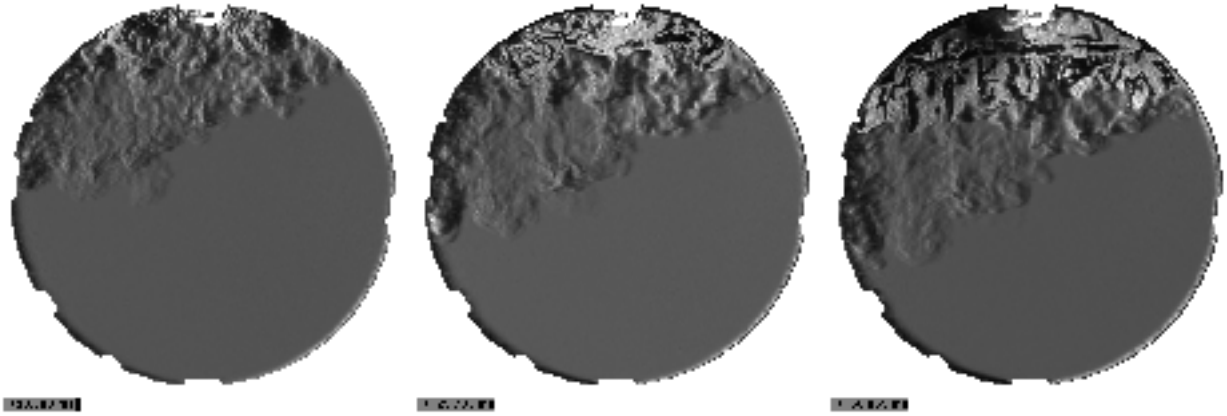

P_{RATIO} = 3, T_S = 90 ms → **Exp 79**

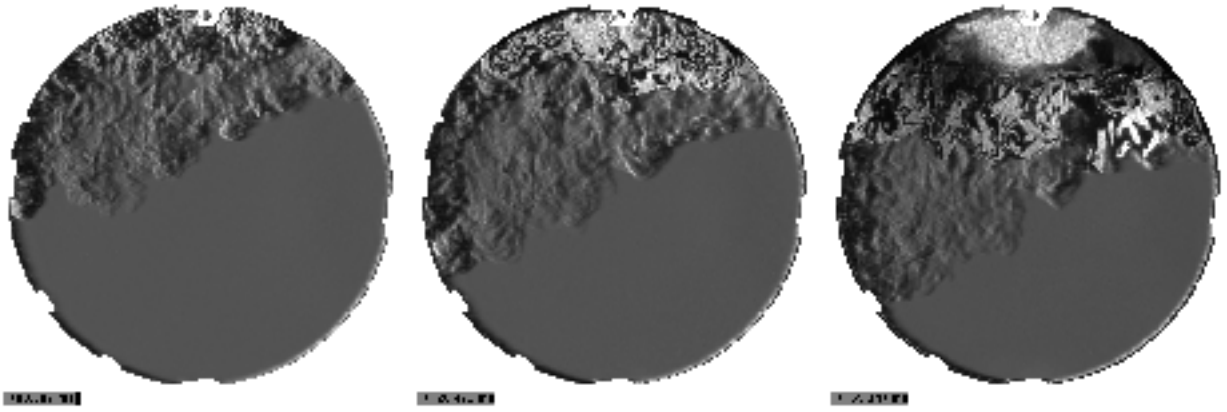

P_{RATIO} = 3, T_S = 100 ms → **Exp 20**

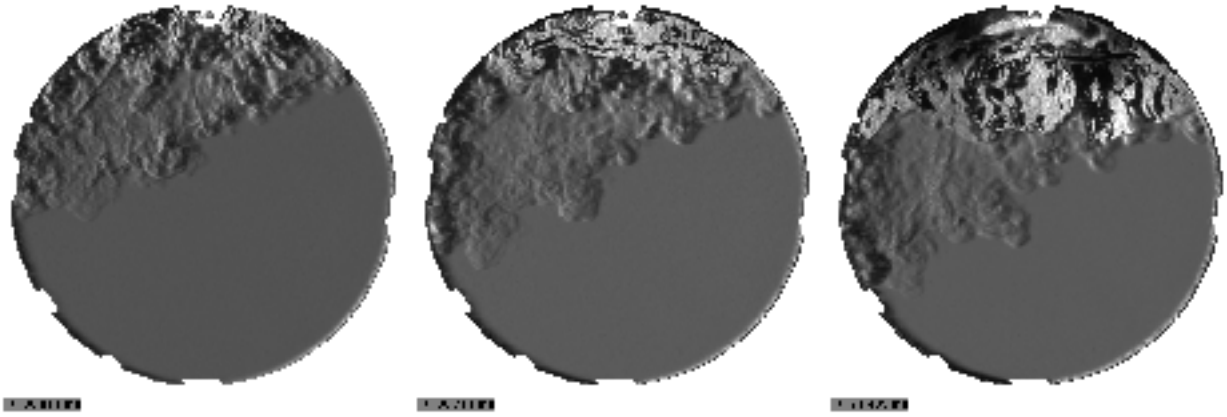

P_{RATIO} = 3, T_S = 100 ms → **Exp 50**

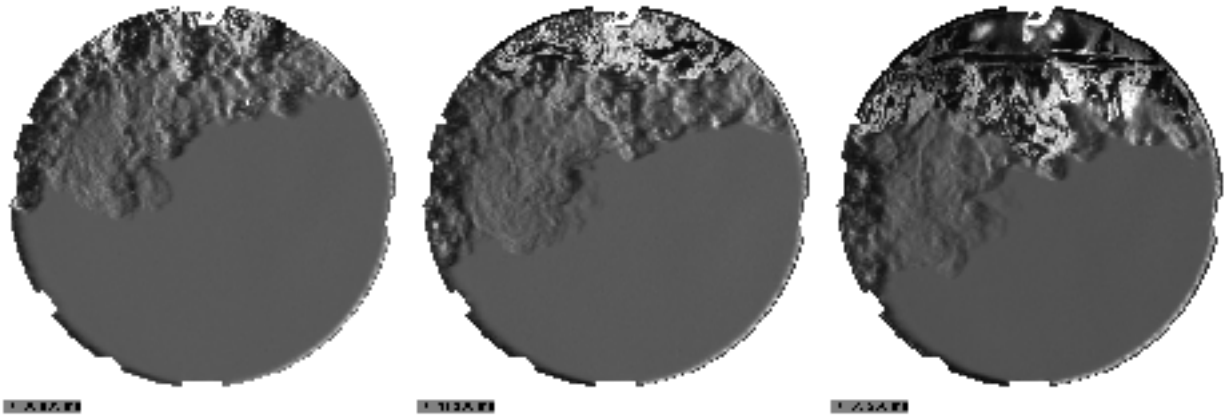

P_{RATIO} = 3, T_S = 100 ms → **Exp 80**

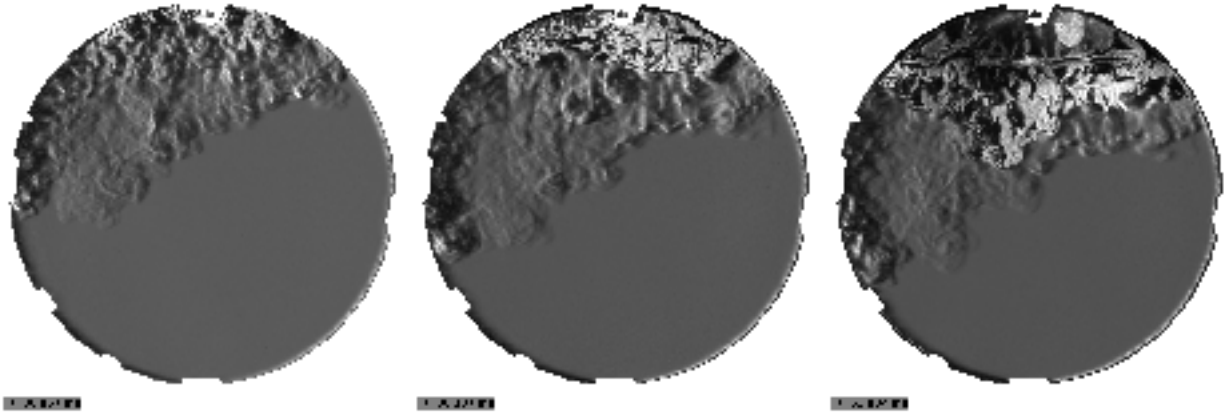

P_{RATIO} = 3, T_S = 120 ms → **Exp 101**

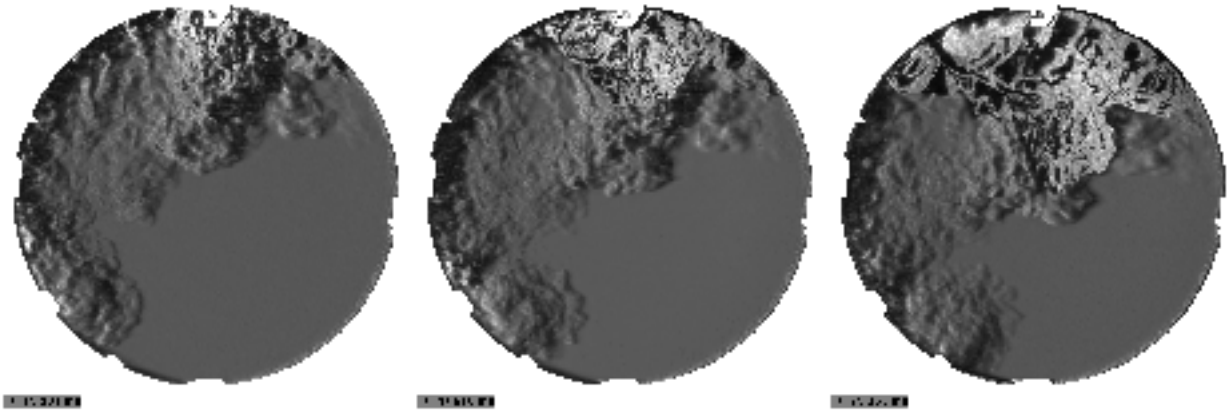

P_{RATIO} = 3, T_S = 120 ms → **Exp 107**

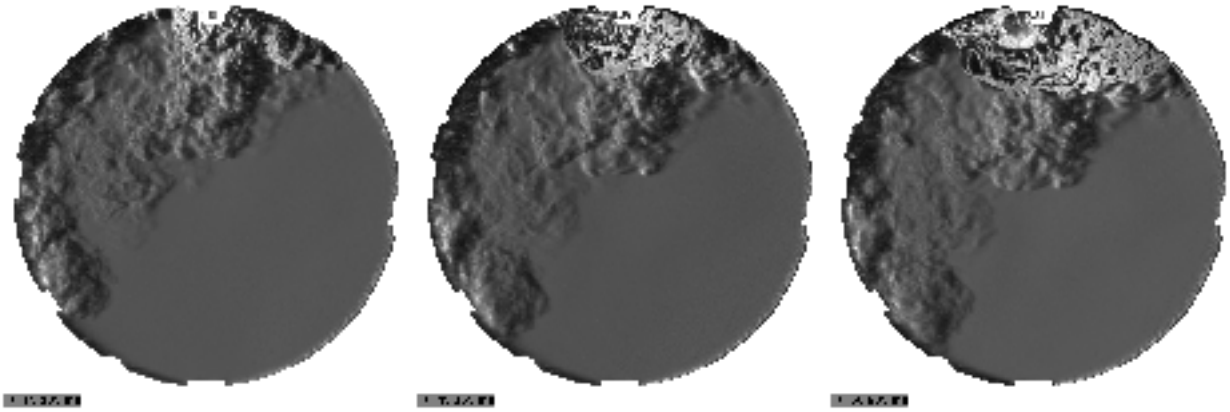

P_{RATIO} = 3, T_S = 120 ms → **Exp 113**

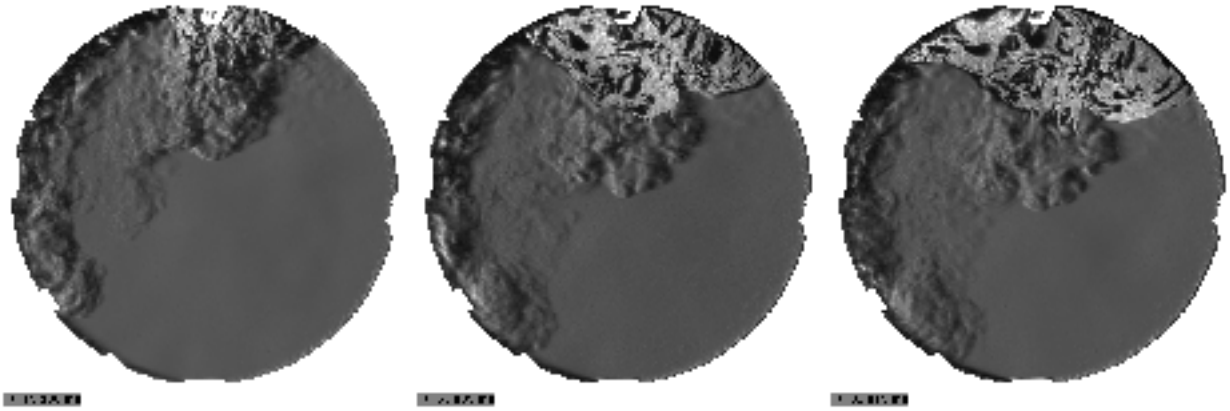

P_{RATIO} = 3, T_S = 140 ms → **Exp 102**

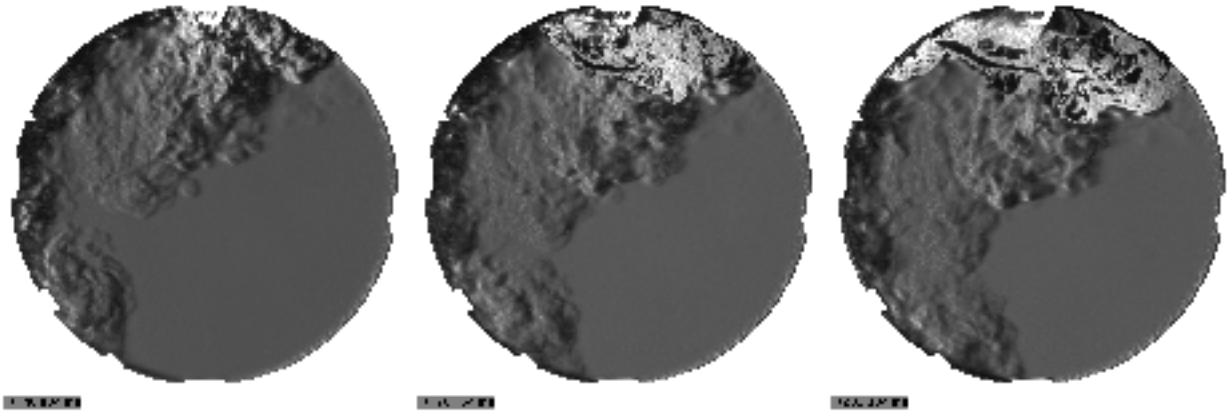

P_{RATIO} = 3, T_S = 140 ms → **Exp 108**

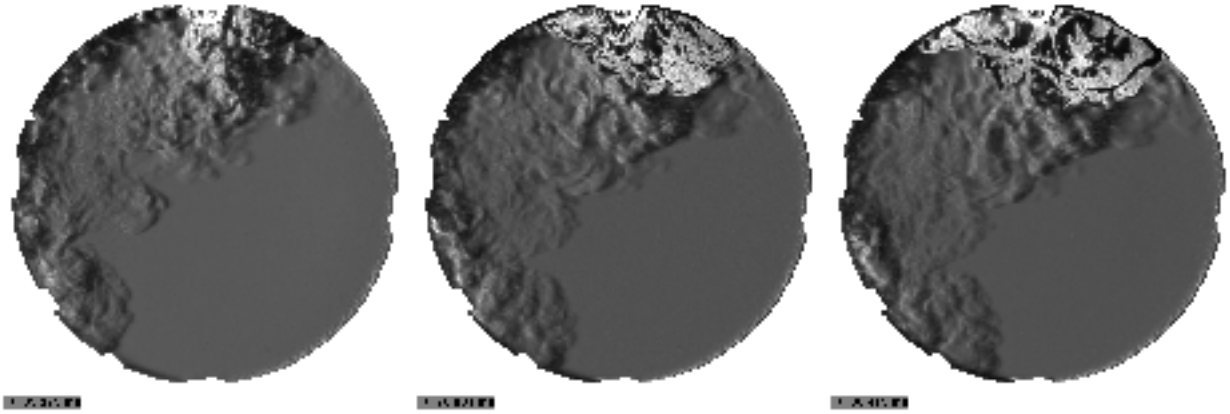

P_{RATIO} = 3, T_S = 140 ms → **Exp 114**

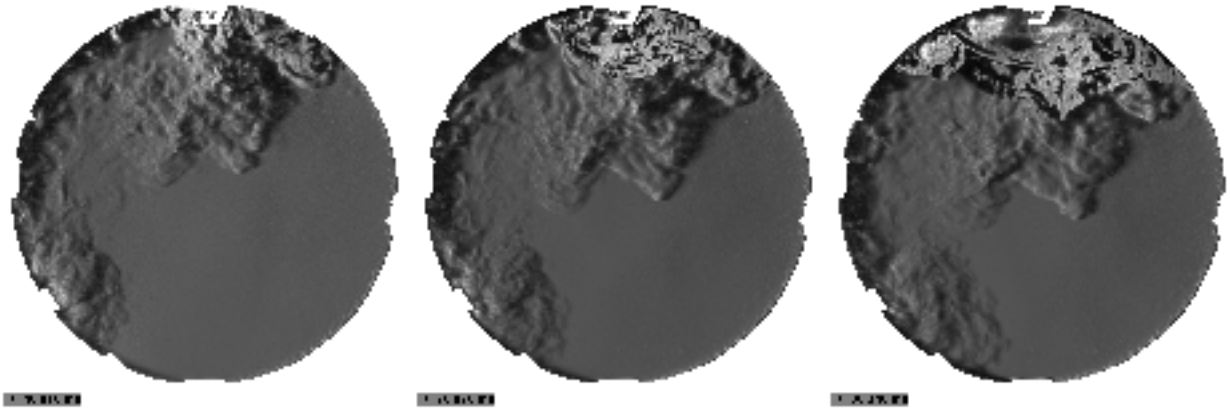

P_{RATIO} = 3, T_S = 160 ms → **Exp 109**

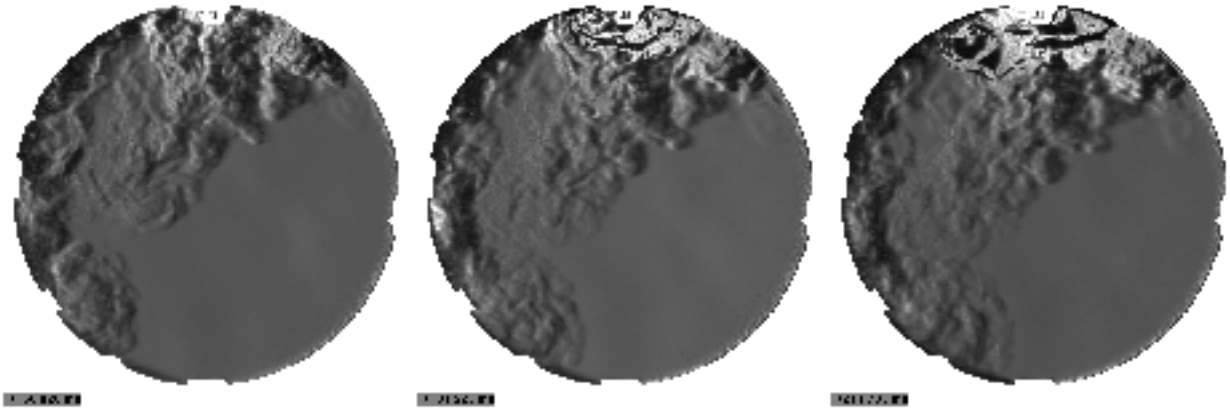

P_{RATIO} = 3, T_S = 140 ms → **Exp 115**

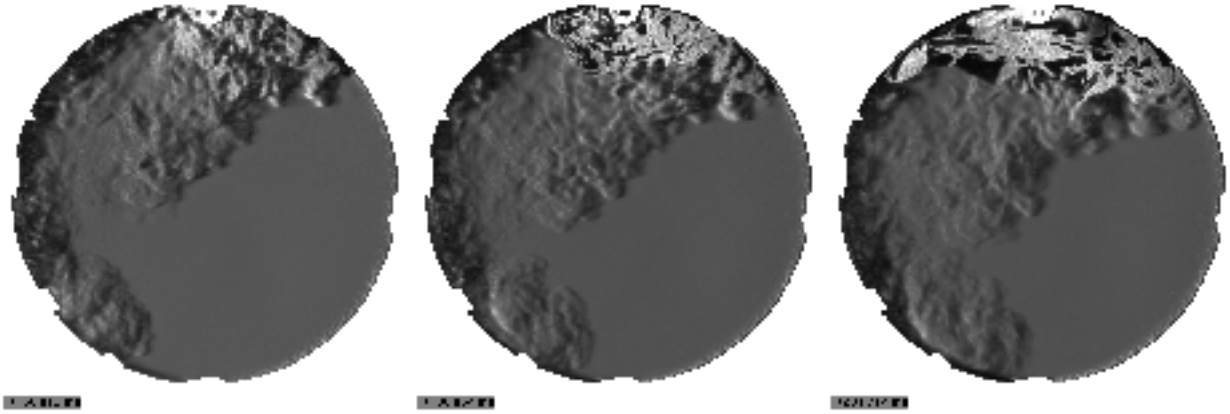

P_{RATIO} = 4, T_S = 60 ms → **Exp 56**

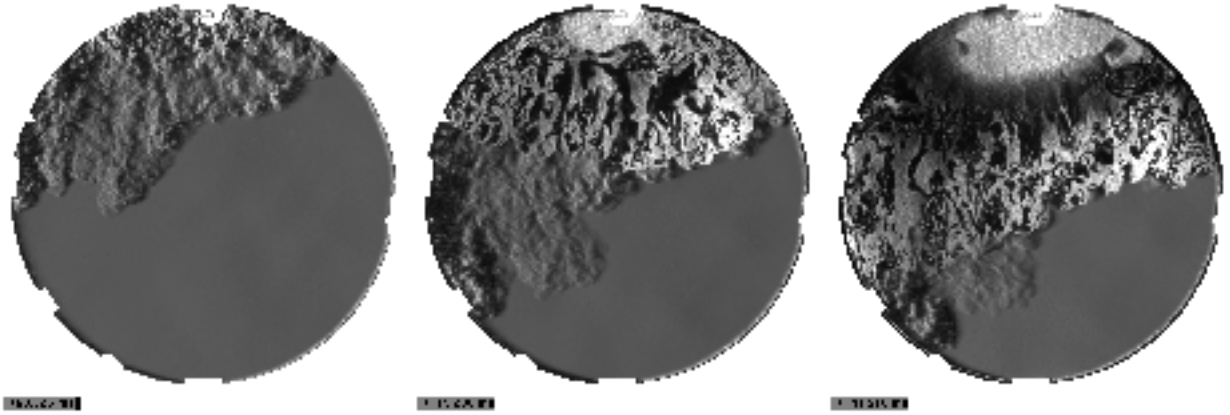

P_{RATIO} = 4, T_S = 80 ms → **Exp 28**

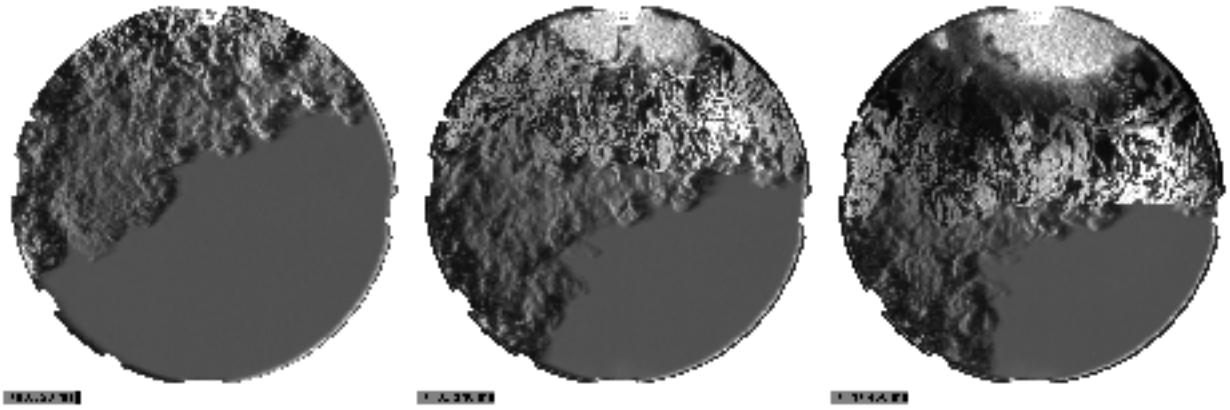

P_{RATIO} = 4, T_S = 80 ms → **Exp 58**

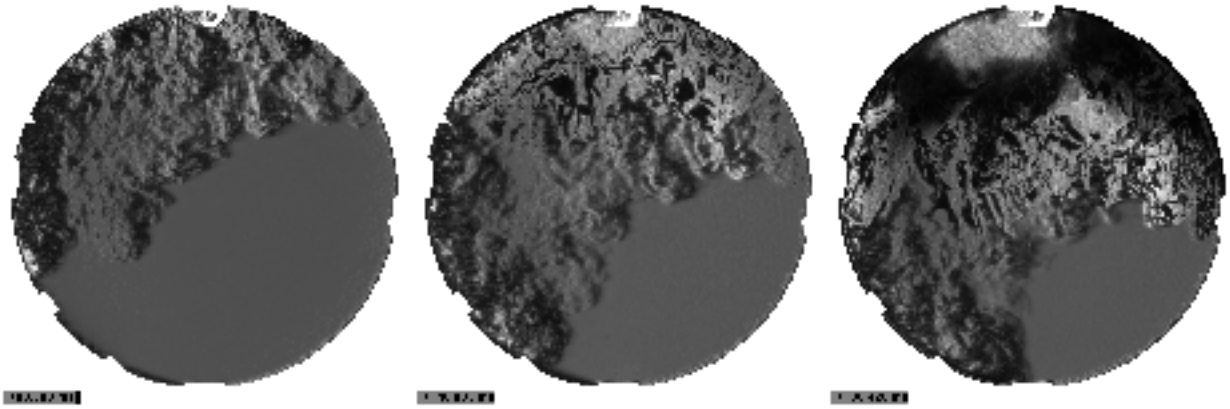

P_{RATIO} = 4, T_S = 90 ms → **Exp 29**

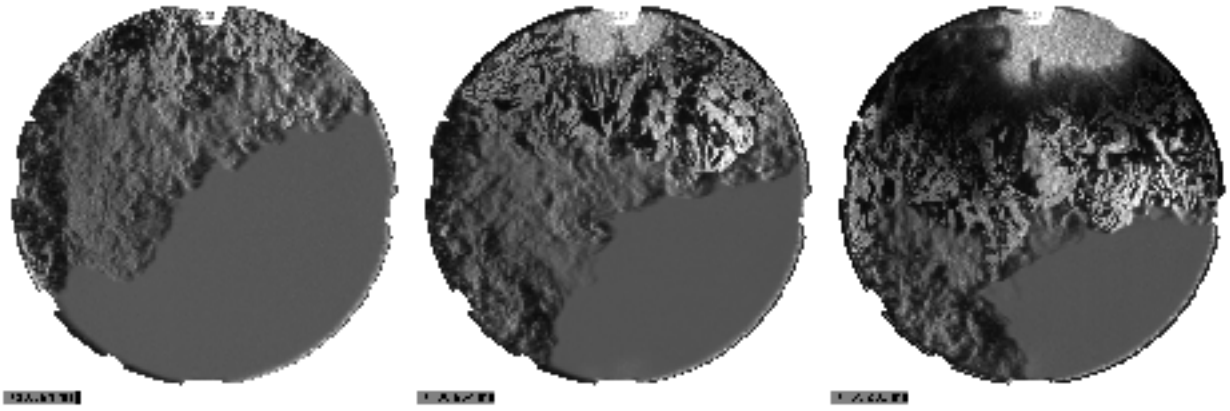

P_{RATIO} = 4, T_S = 90 ms → **Exp 59**

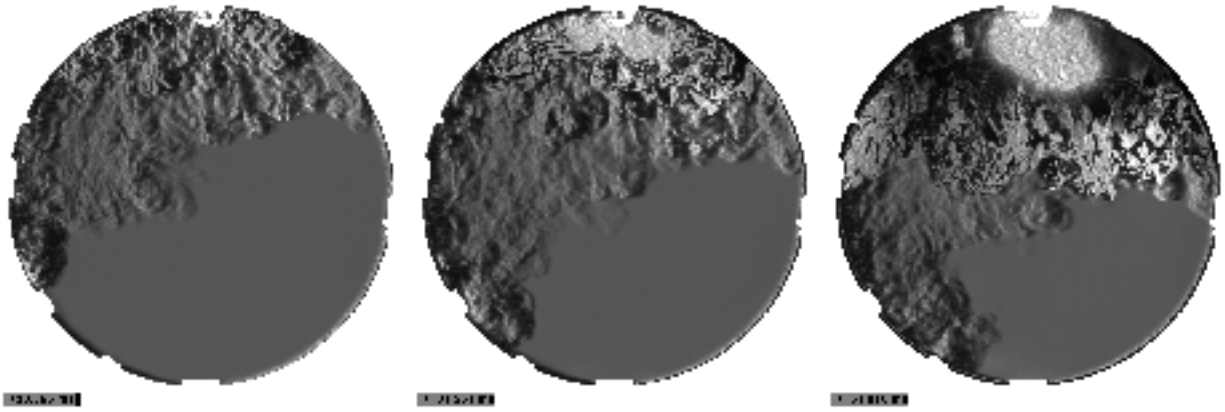

P_{RATIO} = 4, T_S = 90 ms → **Exp 89**

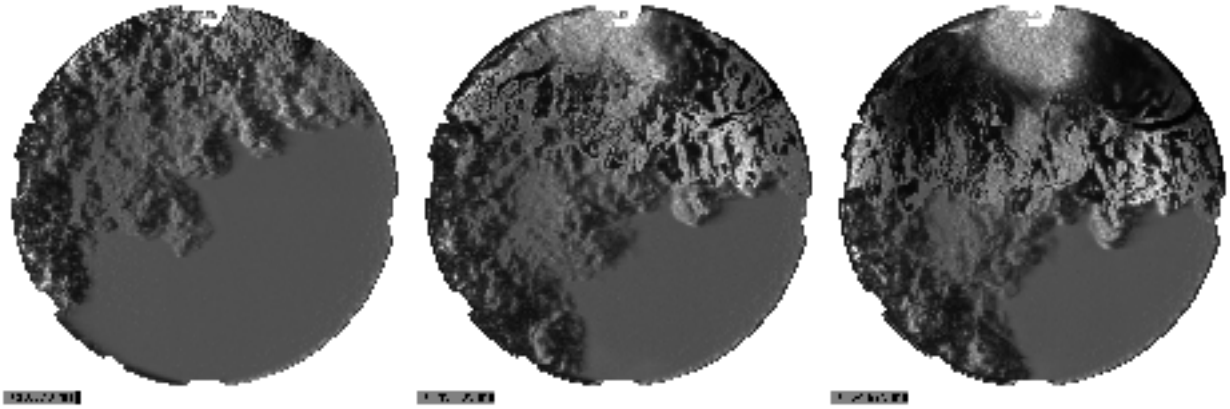

P_{RATIO} = 4, T_S = 100 ms → **Exp 30**

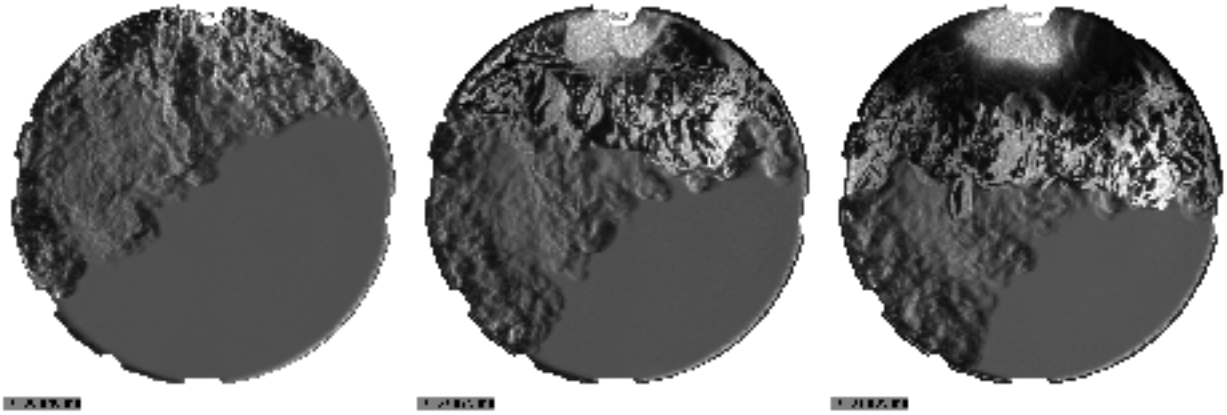

P_{RATIO} = 4, T_S = 100 ms → **Exp 60**

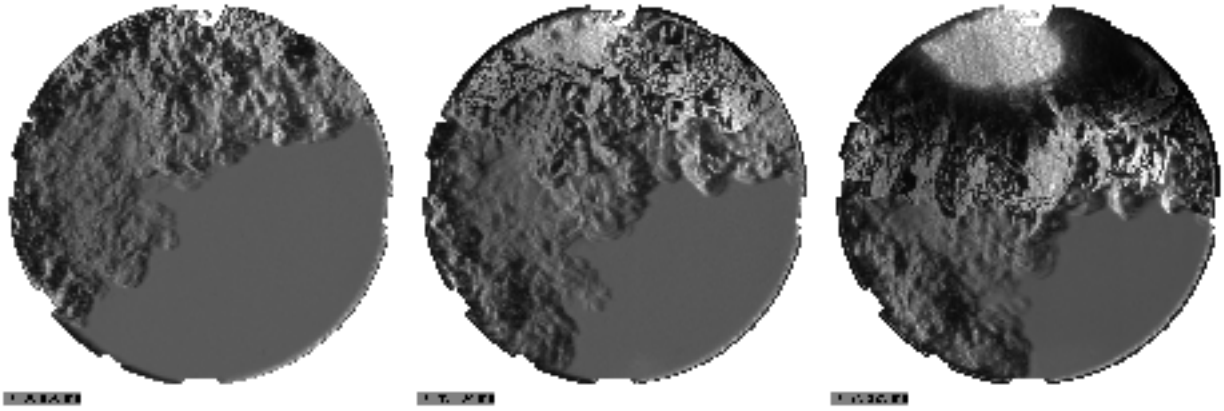

P_{RATIO} = 4, T_S = 100 ms → **Exp 90**

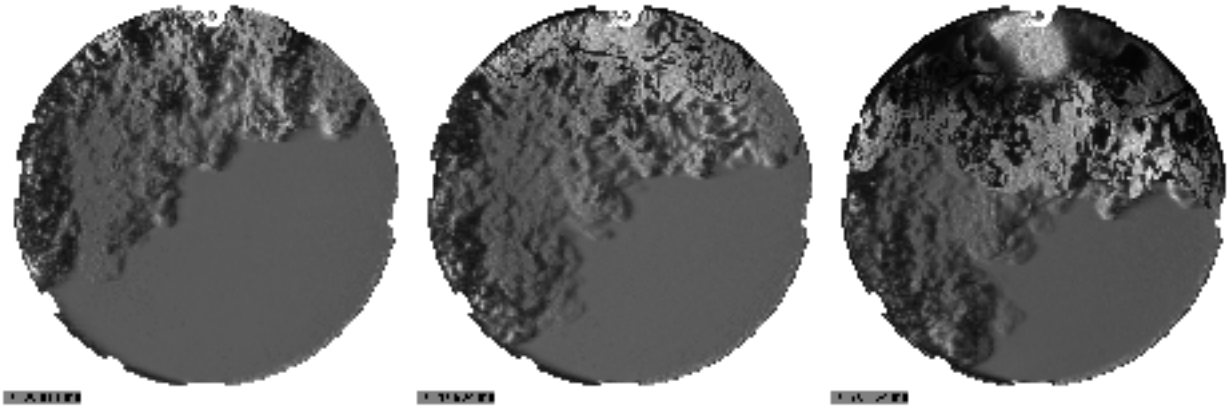

P_{RATIO} = 4, T_S = 120 ms → **Exp 116**

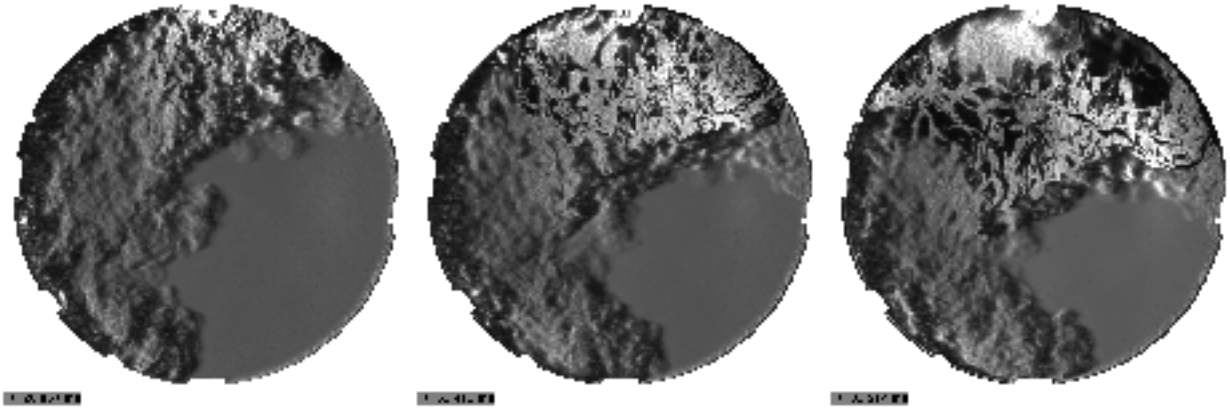

P_{RATIO} = 4, T_S = 140 ms → **Exp 105**

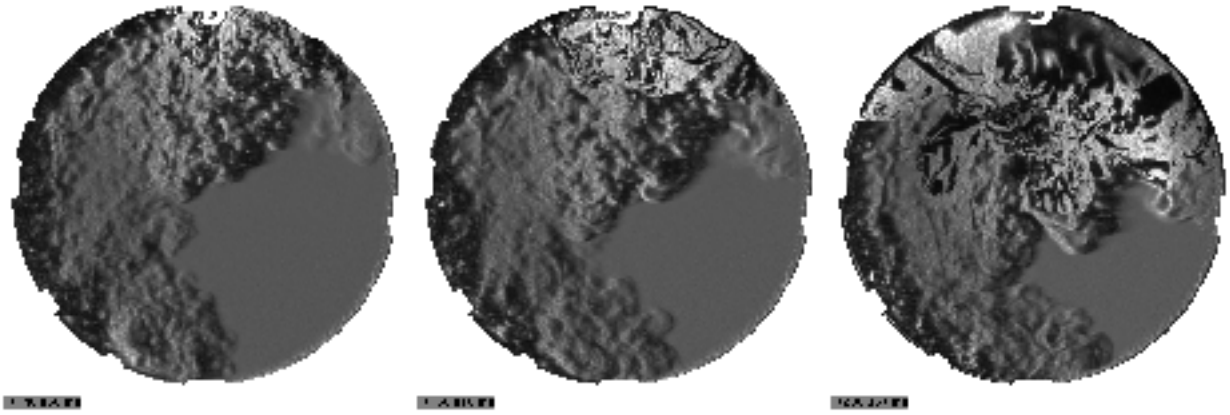

P_{RATIO} = 4, T_S = 140 ms → **Exp 117**

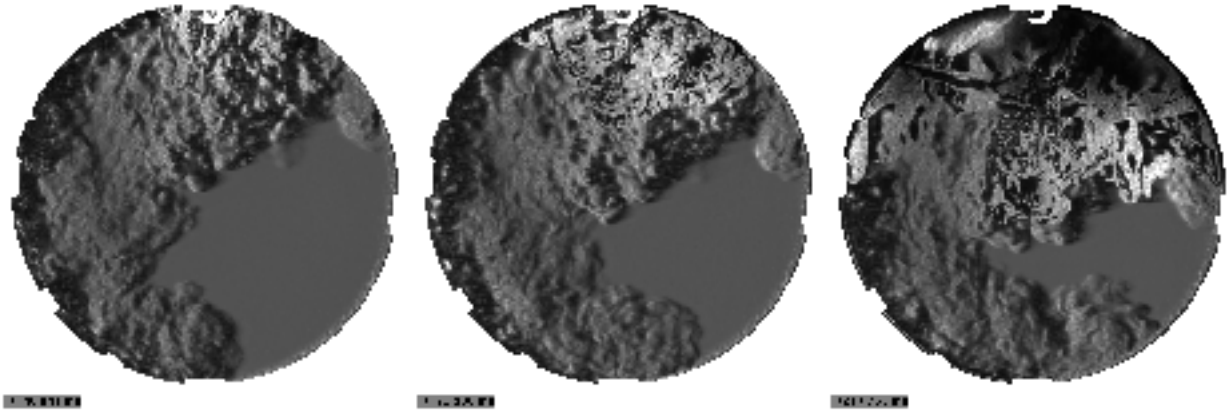

P_{RATIO} = 4, T_S = 160 ms → **Exp 106**

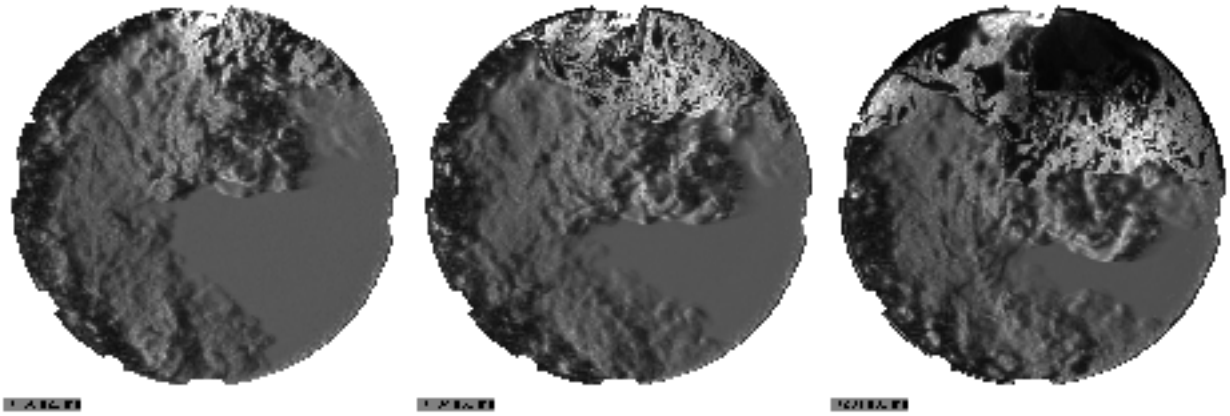

P_{RATIO} = 4, T_S = 160 ms → **Exp 112**

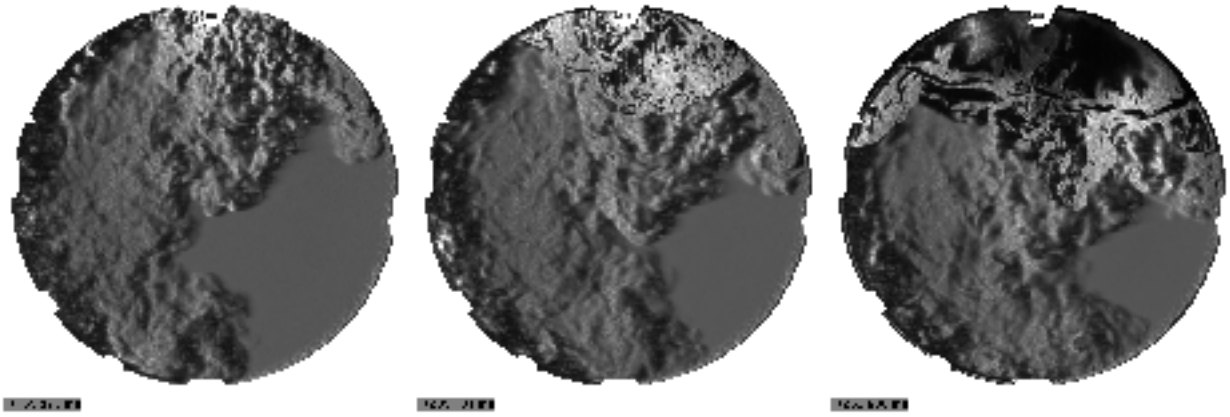

APPENDIX C: SELECT IMAGES FOR NON-COMBUSTING RUNS

The following is a collection of images taken from a typical cold flow experiment at pressure ratios of two, three and four. There are 18 slides shown for each pressure ratio, broken up in 9 slides per page. Image progression order is to the right, then down.

P_{RATIO} 2: First slide at **25.26 ms** after CSOI. The rest of the slides are shown at time intervals of **5.05 ms**.

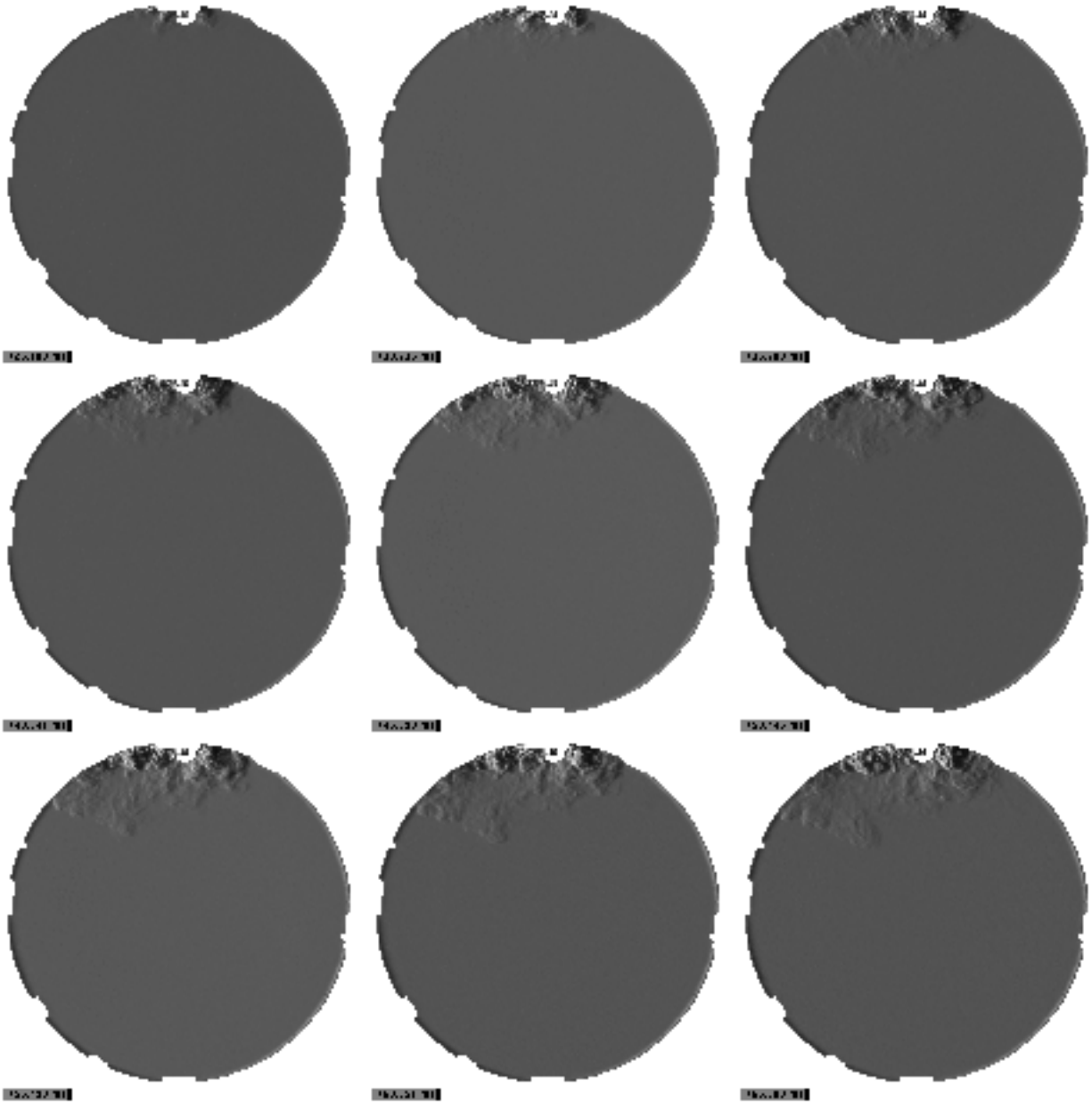

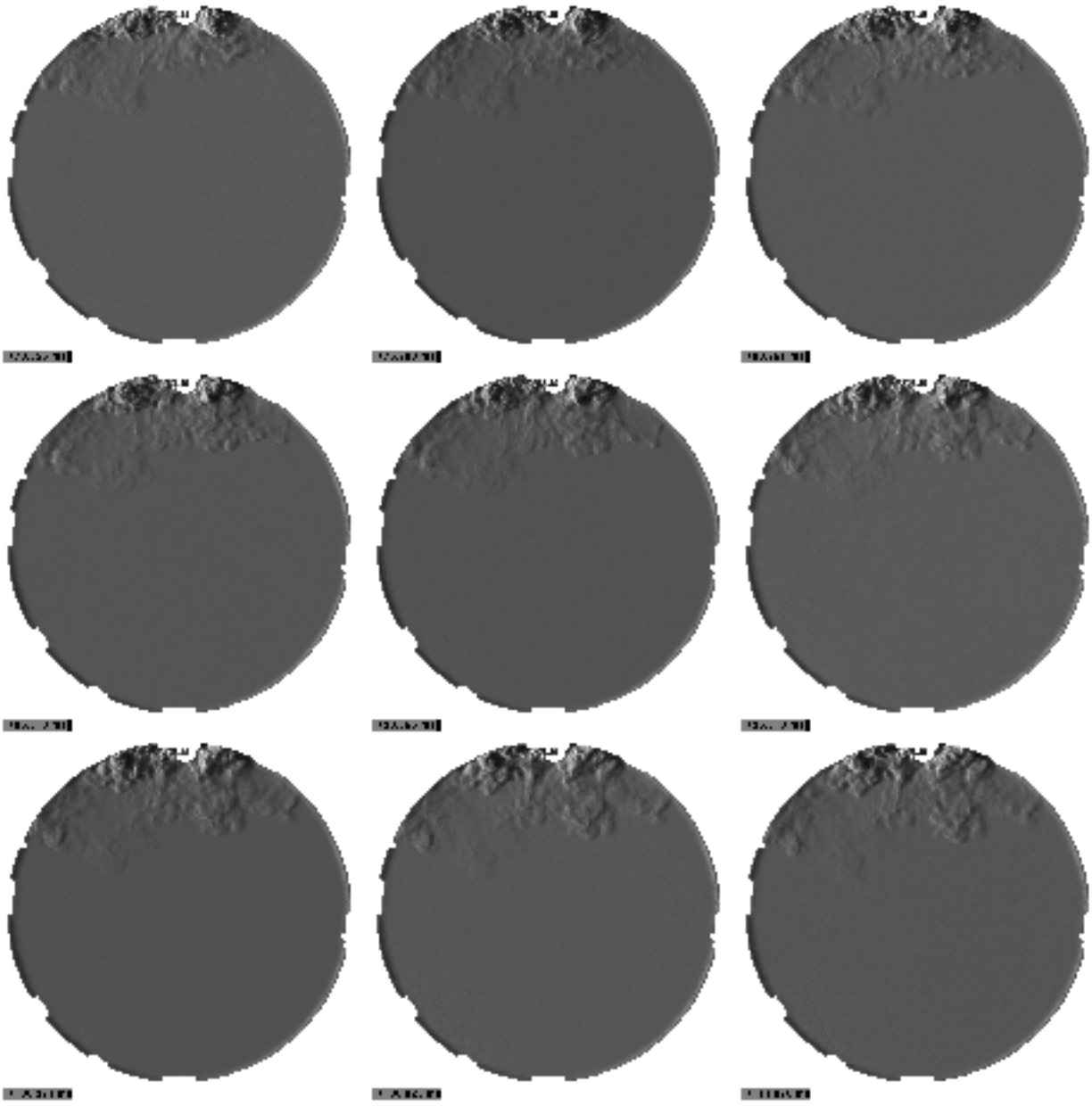

P_{RATIO} 3: First slide at **19.02 ms** after CSOI. The rest of the slides are shown at time intervals of **6.34 ms**.

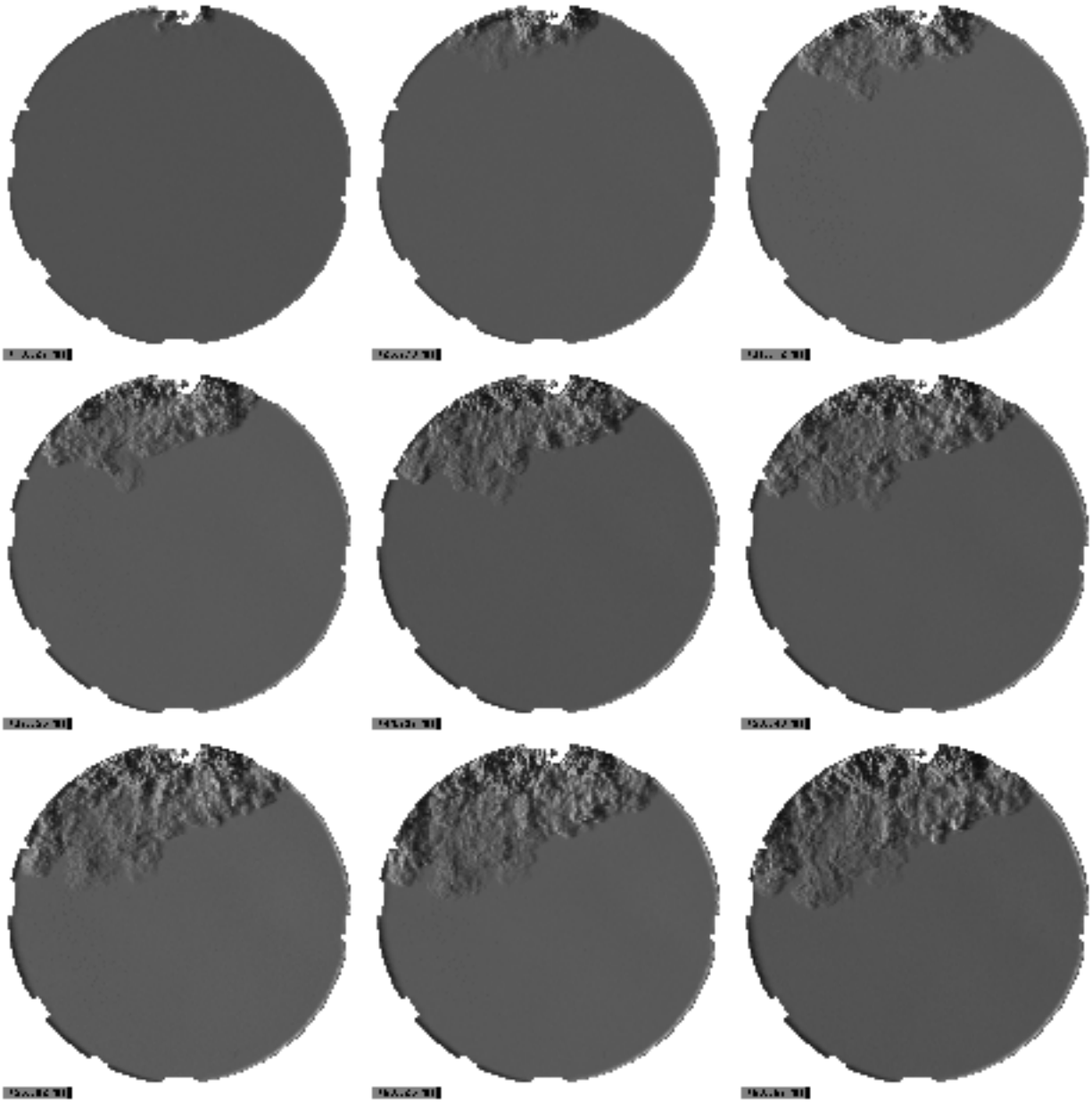

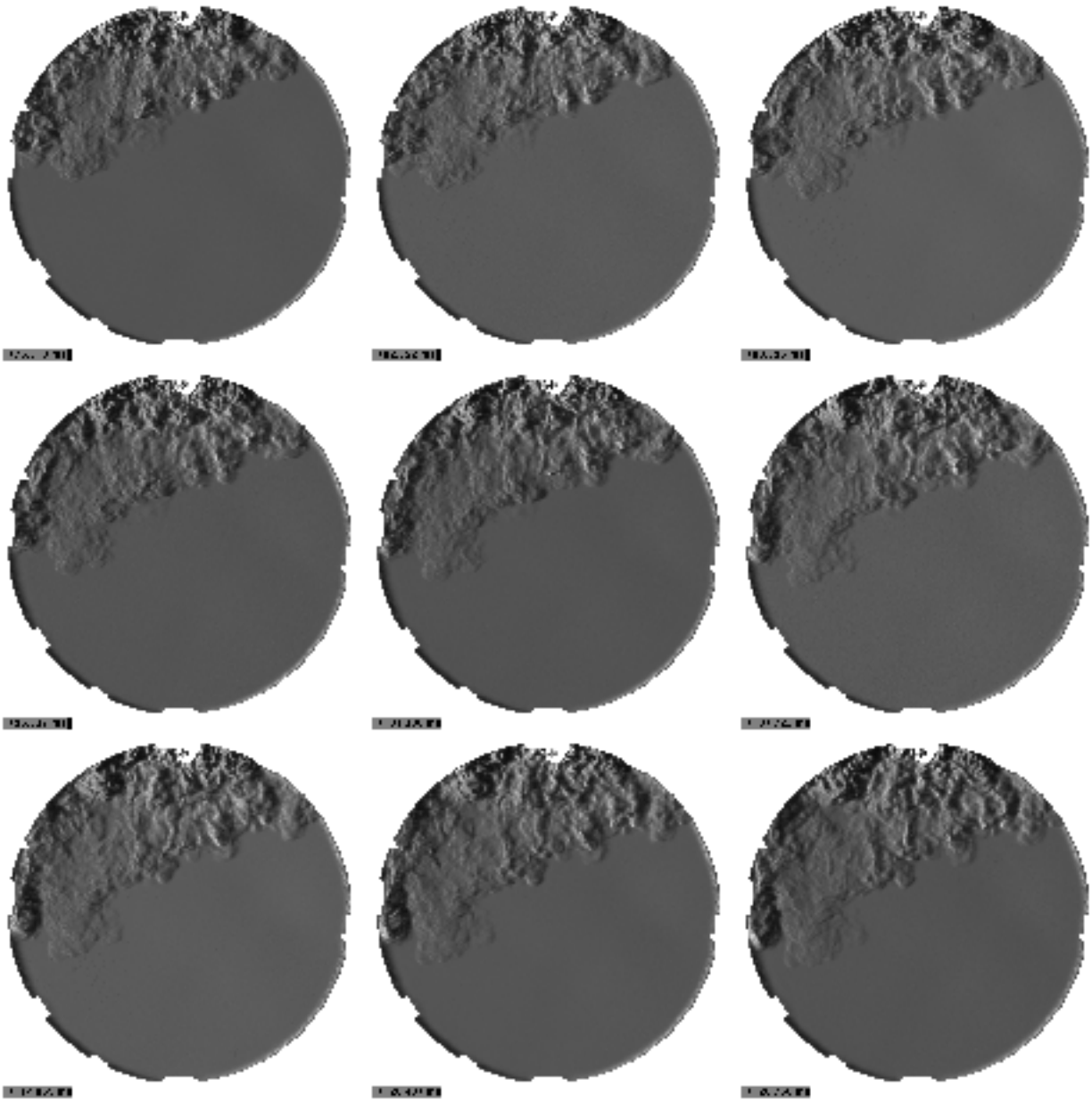

P_{RATIO} 4: First slide at **16.13 ms** after CSOI. The rest of the slides are shown at time intervals of **8.06 ms**.

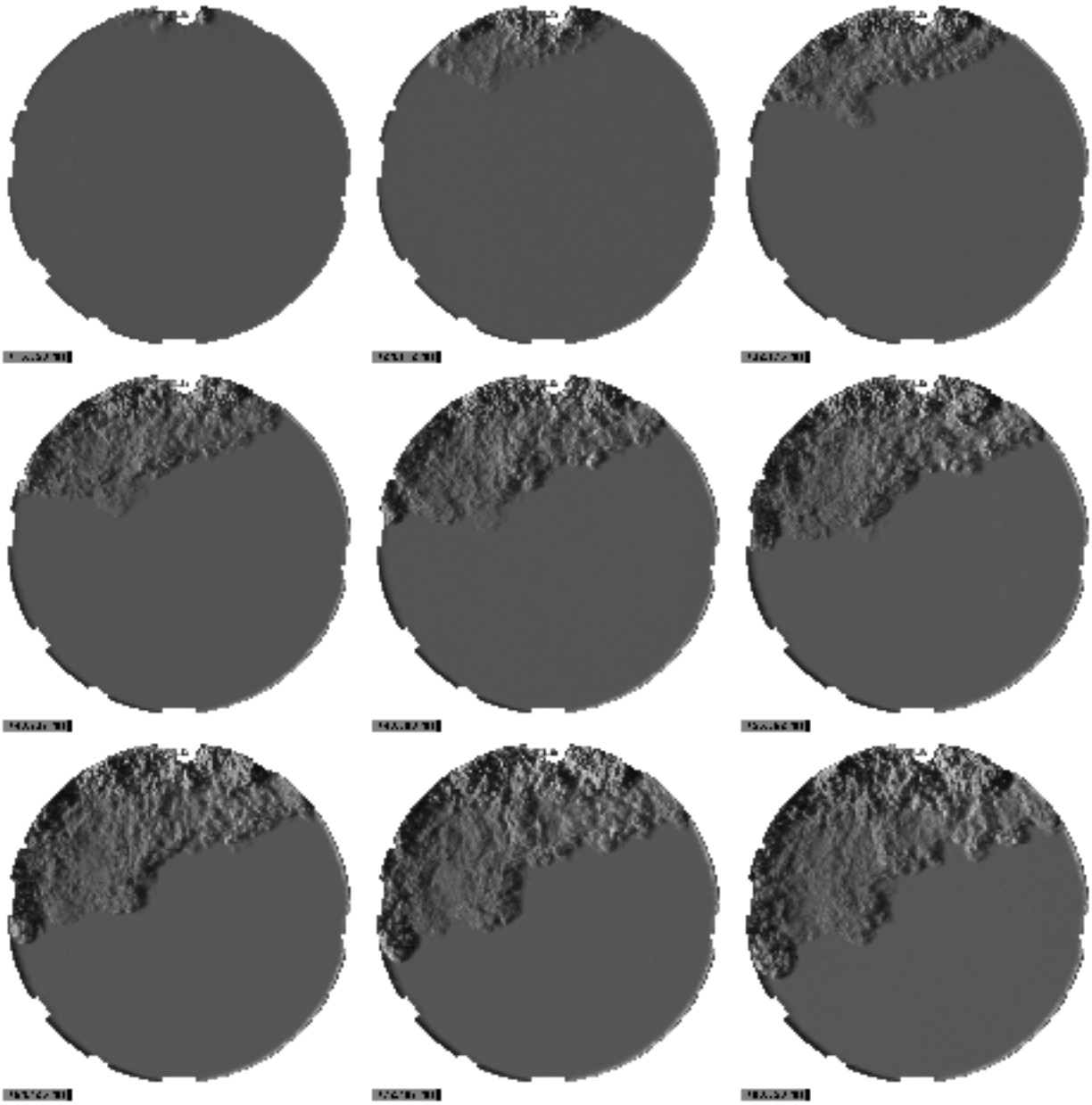

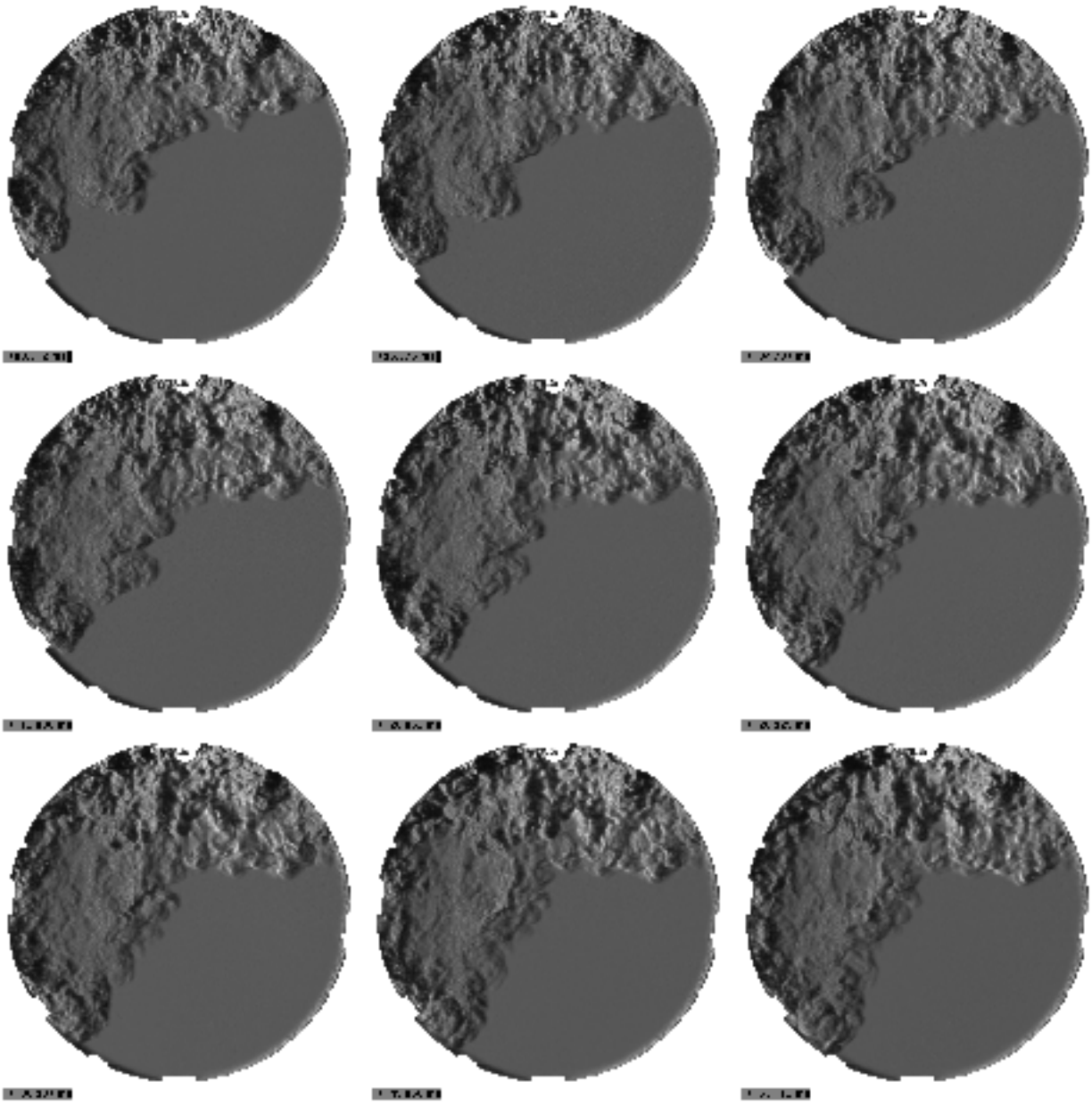

APPENDIX D: SELECT MATLAB PROCESSING CODE

The first subset of Matlab program code was used to conduct the combustion calculations. The second subset of code was used for image processing. The third subset was used for post-processing image binarization. For both combustion calculations and image processing a main routine called "*process.m*" was written which calls other functions as required. The important functions called by the main routine are also shown here.

PART I: COMBUSTION CALCULATION FUNCTIONS

MAIN FILE: "process.m"

```
% Zero the starting time based on camera trigger:
Z_DATA = zerodata(EXP_DATA);

% Look up initial temperature:
TEMP = mean(EXP_DATA(1:3,5));

clear EXP_DATA;

TIME = (Z_DATA(:,1));
PIEZO = filterdata(Z_DATA, 2, 2000);
%PIEZO_ERROR = abs(PIEZO - Z_DATA(:,2));

% Peg the Piezoelectric pressure:
PIEZO = PIEZO - P_INIT(1) + P_INIT(2);
Z_DATA(:,2) = Z_DATA(:,2) - P_INIT(1) + P_INIT(2);

% Subtract pressure rise due to injection for HR calculations:
INJECTION_PRESS = dlmread(['cold_flow_pratio_' num2str(P_RATIO)
'_PIEZO.txt']);
PIEZO_COMB = PIEZO(1:45001) - INJECTION_PRESS(1:45001, 10) - P_INIT(2);
clear INJECTION_PRESS;

% Calculate pressure derivatives for HR calculations:
DP_DATA(:,1) = TIME(1:(length(PIEZO_COMB)-1));
DP_DATA(:,2) = dp(PIEZO_COMB);

% Filter the pressure derivative data:
DPIEZO = filterdp(DP_DATA, 2, 300);

% Calculate heat release rate:
DH_PIEZO = hrr(DPIEZO);
DH_PIEZO_RAW = hrr(DP_DATA(:,2));

% Calculate net integrated heat release:
H_PIEZO = ihrr(DH_PIEZO);
```

```
H_PIEZO_RAW = ihrr(DH_PIEZO_RAW);

% Plot pressure values:
figure(3);
plot(TIME(FIRST:LAST), Z_DATA(FIRST:LAST,2), 'green', TIME(FIRST:LAST),
PIEZO(FIRST:LAST), 'blue');
title('Overall Pressure - Pegged and Zeroed for Camera Trigger');
ylabel('Pressure [PSI]');
xlabel('Time [s]');
legend('Raw pressure signal', 'FFT pressure');
%
figure(4);
plot(TIME(FIRST:LAST), PIEZO_COMB(FIRST:LAST), 'blue');
title('Combustion Pressure - Pegged and Zeroed for Camera Trigger');
ylabel('Pressure [PSI]');
xlabel('Time [s]');

% Plot net heat release rate:
figure(5);
plot(TIME(FIRST:LAST), DH_PIEZO_RAW(FIRST:LAST), 'r', TIME(FIRST:LAST),
DH_PIEZO(FIRST:LAST), 'b');
title('Heat Release Rate, Piezoelectric');
ylabel('HRR [kW]');
xlabel('Time [s]');
legend('Unfiltered', 'FFT Filtered');

% Plot net integrated heat release:
figure(6);
plot(TIME(FIRST:LAST), H_PIEZO_RAW(FIRST:LAST), 'r', TIME(FIRST:LAST),
H_PIEZO(FIRST:LAST), 'b');
title('Net Integrated Heat Release, Piezoelectric');
ylabel('IHRR [kJ]');
xlabel('Time [s]');
legend('Unfiltered', 'FFT Filtered');

Plot HRR and IHRR on the same plot:
figure(7);
plot(TIME(FIRST:LAST), H_PIEZO(FIRST:LAST), '. black', TIME(FIRST:LAST),
DH_PIEZO(FIRST:LAST), 'black');
title('Net Rate and Integrated Rate of Heat Release');
ylabel('HRR [kW]');
xlabel('Time [s]');
legend('Net Integrated HR', 'Net HR Rate');

% Compute combustion data:
POSN_SPARK = round(SPARK/(2e-05));

% Define new heat release vector starting from spark location:
H_PIEZO_RAW_SPARK = H_PIEZO_RAW(POSN_SPARK:length(H_PIEZO_RAW));

[H_MAX, POSN_H_MAX] = max(H_PIEZO_RAW);

H_COMB = H_MAX - H_PIEZO_RAW(POSN_SPARK);
FIVE_PERCENT_H_COMB = 0.05 * H_COMB;
TEN_PERCENT_H_COMB = 0.10 * H_COMB;
```

```
NINETY_PERCENT_H_COMB = 0.90 * H_COMB;
NINETYFIVE_PERCENT_H_COMB = 0.95 * H_COMB;

POSN_FIVE_PERCENT_H_COMB = find(H_PIEZO_RAW_SPARK > (FIVE_PERCENT_H_COMB +
H_PIEZO_RAW(POSN_SPARK)), 1) + POSN_SPARK;
POSN_TEN_PERCENT_H_COMB = find(H_PIEZO_RAW_SPARK > (TEN_PERCENT_H_COMB +
H_PIEZO_RAW(POSN_SPARK)), 1) + POSN_SPARK;
POSN_NINETY_PERCENT_H_COMB = find(H_PIEZO_RAW_SPARK > (NINETY_PERCENT_H_COMB
+ H_PIEZO_RAW(POSN_SPARK)), 1) + POSN_SPARK;
POSN_NINETYFIVE_PERCENT_H_COMB = find(H_PIEZO_RAW_SPARK >
(NINETYFIVE_PERCENT_H_COMB + H_PIEZO_RAW(POSN_SPARK)), 1) + POSN_SPARK;

T_FIVE = TIME(POSN_FIVE_PERCENT_H_COMB) - TIME(POSN_SPARK);
T_TEN = TIME(POSN_TEN_PERCENT_H_COMB) - TIME(POSN_SPARK);
T_NINETY = TIME(POSN_NINETY_PERCENT_H_COMB) - TIME(POSN_SPARK);
T_NINETYFIVE = TIME(POSN_NINETYFIVE_PERCENT_H_COMB) - TIME(POSN_SPARK);

[DH_MAX, POSN_DH_MAX] = max(DH_PIEZO_RAW);
T_DH_MAX = TIME(POSN_DH_MAX) - TIME(POSN_SPARK);

Write data to file:
dlmwrite('combustion_data.txt', [EXP_NO P_RATIO SPARK TEMP P_INIT(2)
max(PIEZO_COMB) DH_MAX T_DH_MAX FIVE_PERCENT_H_COMB ...
    TEN_PERCENT_H_COMB NINETY_PERCENT_H_COMB NINETYFIVE_PERCENT_H_COMB T_FIVE
T_TEN T_NINETY ...
    T_NINETYFIVE], '-append', 'roffset', 0, 'delimiter', '\t', 'precision',
6);

EXPORT(:,1) = TIME(1:45000);
EXPORT(:,2) = PIEZO_COMB(1:45000);
EXPORT(:,3) = DH_PIEZO_RAW(1:45000);
EXPORT(:,4) = DH_PIEZO(1:45000);
EXPORT(:,5) = H_PIEZO_RAW(1:45000);
EXPORT(:,6) = H_PIEZO(1:45000);
dlmwrite(['proc_data_' num2str(EXP_NO) '.txt'], EXPORT, 'delimiter', '\t',
'precision', 6);
```

FUNCTION: "loaddata.m"

```
function trace=loaddata(exp)
% Loads data based on experiment #
% Input by user

if exp < 10
    expstr = ['00' num2str(exp)];
elseif exp < 100
    expstr = ['0' num2str(exp)];
elseif exp < 1000
    expstr = num2str(exp);
else
    fprintf('Error in experiment number');
end

location = 'RawData\';
file = ['data' expstr '.txt'];

trace = dlmread([location file]);
%trace = dlmread(file);
```

FUNCTION: "init_press.m"

```
function P_INIT=init_press(EXP_DATA, NO_POINTS)

% Function averages inital pressure and returns value

for i=1:2
    INIT_PRESS_MEAN(i) = mean(EXP_DATA(1:100,(i+1)));
    INIT_PRESS_MEDIAN(i) = median(EXP_DATA(1:100,(i+1)));
    PERCENT_DIFF(i) = 100 * abs(INIT_PRESS_MEAN(i) - INIT_PRESS_MEDIAN(i)) /
(INIT_PRESS_MEAN(i) + INIT_PRESS_MEDIAN(i)) / 2;
    if (PERCENT_DIFF(i) > 5)
        fprintf('Error in initial pressure calculation!');
        fprintf('Revise averaging window extrema.');
        fprintf('Percent difference is:');
        PERCENT_DIFF(i)
    end

    P_INIT(i) = INIT_PRESS_MEDIAN(i);
end
```

FUNCTION: "zerodata.m"

```
function z_data=zerodata(exp)

% Function zeroes the time of the pressure trace to have it coincide with
% the camera trigger

N_points=length(exp);

% Find camera trigger and assign time and pressure vectors:
first_point=1;
while exp(first_point,4) < 5
    first_point=first_point+1;
end

z_data(:,1) = exp(first_point:N_points,1) - exp(first_point,1);
z_data(:,2) = exp(first_point:N_points,2);
z_data(:,3) = exp(first_point:N_points,3);
```

FUNCTION: "filterdata.m"

```
function data_rev=filterdata(raw_file, COL_DATA, CUTOFF_FREQ)
%%%%%%%%%%%%%%%%%%%%%%%%%%%%%%%%%%%%%%%%%%%%%%%%%%%%%%%%%%%%%%%%%%%%%%%%%%%%
%
% Edward C. Chan, Mechanical Engineering
% University of British Columbia
% 28 February, 2008
% Rev. B
% Modified by: Andrew Mezo
% Date: February 29, 2008
%
% This program basically removes ignition signal noise (low frequency,
% high amplitude) using a window median filter.  Then it applies
% a gaussian low-pass filter to get rid of the higher frequency
% noise components.  The difference between the raw and filtered
% signal is available for verification.
%
% User configurable Inputs
% ------------------------
%
% COL_TIME, COL_DATA - columns on data file denoting time and the
%       unfiltered data.
%
% MEDIAN_BOUND - size of the window for the median filter
%   (size = 2 x MEDIAN_BOUND + 1)
%
% PRUNE_THRESHOLD - if the noise-to-signal ratio of the median filter is
%   greater than this value, it gets replaced by the median
%
% NYQUIST_FACTOR - amount of zero padding required for the guassian
%   filter (new array size = # samples x NYQUIST_FACTOR)
%
% CUTOFF_FREQ - Cut off frequency of the guassian filter
%
```

```
% EXTEND_LENGTH - number of elements to extend the data on both ends of
%   the array
%
% Outputs
% -------
%
% time_raw - array of time
% data_raw - array of unfiltered data
% data_rev - array of filterd data
% delta    - abs. difference between filtered and unfiltered data sets
%
% Remarks
% -------
%
% (1) PRUNE_THRESHOLD should be at least 1 to prevent pruning of
%       otherwise meaningful data
%
% (2) NYQUIST_FACTOR should be at least 2 (10 is quite ideal) to
%       minimize aliasing
%
% (3) CUTOFF_FREQ should be high enough to avoid smearing of
%       important data.  It should be at least 200 Hz (I think)
%
%%%%%%%%%%%%%%%%%%%%%%%%%%%%%%%%%%%%%%%%%%%%%%%%%%%%%%%%%%%%%%%%%%%%%%%%%%%%

        %
        % some information about the data file
        %

COL_TIME = 1;

        %
        % configurations for the window median filter
        %

MEDIAN_BOUND = 10;
PRUNE_THRESHOLD = 1.1;

        %
        % configuations for the gaussian low-pass filter
        %

NYQUIST_FACTOR = 10;

        %
        % data extension length
        %

EXTEND_LENGTH = 1000;


%%%%%%%%%%%%%%%%%%%%%%%%%%%%%%%%%%%%%%%%%%%%%%%%%%%%%%%%%%%%%%%%%%%%%%%%%%%%
%
% DO NOT CHANGE BELOW THIS LINE
%
```

```
%%%%%%%%%%%%%%%%%%%%%%%%%%%%%%%%%%%%%%%%%%%%%%%%%%%%%%%%%%%%%%%%%%%%%%%%%%%%

        %
        % extract sample information
        %

N_LINES     = length (raw_file);
SAMPLE_TIME = raw_file (N_LINES, COL_TIME) - raw_file (1, COL_TIME);
SAMPLE_FREQ = N_LINES / SAMPLE_TIME;

        %
        % extract padding information
        %

N_PADDED = floor (N_LINES * NYQUIST_FACTOR);
N_FREQ   = floor ((N_PADDED + 0.5)/2);
MAX_FREQ = 0.5 * SAMPLE_FREQ * NYQUIST_FACTOR;

        %
        % extract data into arrays
        %

time_raw = raw_file (:,COL_TIME);
data_raw = raw_file (:,COL_DATA);
data_pad = zeros (N_PADDED, 1);
data_pad(1:N_LINES) = data_raw;

clear raw_file;

        %
        % perform running median filter
        %

INDEX_LO = MEDIAN_BOUND+1;
INDEX_HI = N_LINES - (MEDIAN_BOUND + 1);

for (i=INDEX_LO:INDEX_HI);

    LOWER_BOUND = i - MEDIAN_BOUND;
    UPPER_BOUND = i + MEDIAN_BOUND;

    window_median = median (data_pad (LOWER_BOUND:UPPER_BOUND));
    noise_signal_ratio = (abs(data_pad(i)) - abs(window_median)) /
abs(window_median);

    if (noise_signal_ratio > PRUNE_THRESHOLD)
        data_pad(i) = window_median;
    end

end

        %
        % extend data array (if not, data would for some reason
        % drop off)
```

```
        %

EXTEND_START = N_PADDED - EXTEND_LENGTH +1;
EXTEND_END   = N_LINES + EXTEND_LENGTH;

data_pad(N_PADDED:-1:EXTEND_START) = data_pad(1:EXTEND_LENGTH);
data_pad(N_LINES+1:1:EXTEND_END)   = data_pad(N_LINES:-1:N_LINES-
EXTEND_LENGTH+1);

        %
        % obtain FFT of data
        %

data_fft = fft (data_pad);

        %
        % generate filter
        %

SIGMA = CUTOFF_FREQ / sqrt (2.0 * log(2.0));

filter = zeros (N_PADDED, 1);
filter(1:N_FREQ) = exp ( -0.5*(((1:N_FREQ)-1)/SIGMA).^2.0 );
filter(N_FREQ+1:N_PADDED) = filter(N_FREQ:-1:1);

        %
        % apply filter
        %

data_fil = data_fft .* filter;

        %
        % recover filtered data
        %

data_ift    = ifft (data_fil);
data_rev = real (data_ift(1:N_LINES));
```

FUNCTION: “dp.m”

```
function proc_slope=dp(p)

for i=2:length(p)
    j=i-1;
    dt=2.0000e-005;
    proc_slope(j)=(p(i)-p(j))/dt;
end
```

FUNCTION: “hrr.m”

```
function DH=hrr(DP)

% Calculates heat release rate based on dp/dt

% *************** Constants ****************
GAMMA = 1.4;
CONV_UNIT = 6.894757; % 1 PSI = CONV_UNIT kPA
BOMB_VOLUME = 2.311e-004; %[m^3]
% ******************************************

DH = (1/(GAMMA-1)) * BOMB_VOLUME * DP * CONV_UNIT;
```

FUNCTION: “ihrr.m”

```
function H=ihrr(DH)

% Integrates the heat release rate

INC_VALUE = 0;
for i=1:length(DH)
    INC_VALUE = INC_VALUE + DH(i)*2.000e-005;
    H(i) = INC_VALUE;
end
```

PART II: IMAGE PROCESSING FUNCTIONS

MAIN FUNCTION: “process.m”

```
function process(exp)

%------CONSTANTS---------
start_image=56;
exposure_const=3;  %Divide by this number to get the gray scale exposure
bk_ave_last_image=50;
border_sensitivity = 12;
%------------------------

bk=loadimages(exp,1,bk_ave_last_image);
bk_ave=bkground(bk, bk_ave_last_image);
bk_ave=bk_ave+1;    %Eliminate divide by 0 possibility
bk_ave_dp=im2double(bk_ave);
clear bk;

end_image = filenum(exp);

border = frame_map(bk_ave_dp, border_sensitivity);

for i=start_image:end_image
    frame=loadimage(exp, i);
    frame_dp=im2double(frame);
    c_frame_dp=frame_dp./bk_ave_dp;
    c_frame=uint16(round(c_frame_dp*(65535/exposure_const)));
    c_frame = c_frame + border;

% Black out time increment pixels
    c_frame(461:476,6:97)=frame(461:476,6:97);

    writeimage(exp, c_frame, i, start_image);

end
```

FUNCTION: "loadimages.m"

```
function frame=loadimages(exp,first_image,last_image)
% Loads images based on experiment # and number of images
% Input by user

if exp < 10
    expstr = ['00' num2str(exp)];
elseif exp < 100
    expstr = ['0' num2str(exp)];
elseif exp < 1000
    expstr = num2str(exp);
else
    fprintf('Error in experiment number');
end

location = ['exp' expstr '\'];

for i=first_image:last_image

    if i < 10
        file = ['000' num2str(i) '.tif'];
    elseif i < 100
        file = ['00' num2str(i) '.tif'];
    elseif i < 1000
        file = ['0' num2str(i) '.tif'];
    else
        file = [num2str(i) '.tif'];
    end

        frame(:,:,i) = imread([location file]);

end
```

FUNCTION: "bkground.m"

```
function ave=bkground(exp, no_images)
% Computes arithmetic average of images

ave = exp(:,:,1)-exp(:,:,1);

for i=1:no_images
    ave = ave + exp(:,:,i)/no_images;
end
```

FUNCTION: "filenum.m"

```
function no_files = filenum(exp)

if exp < 10
    expstr = ['00' num2str(exp)];
elseif exp < 100
    expstr = ['0' num2str(exp)];
elseif exp < 1000
    expstr = num2str(exp);
else
    fprintf('Error in experiment number');
end

location = ['exp' expstr '\'];
dirOutput=dir(fullfile(location, '*.tif'));
no_files = length(dirOutput);
```

FUNCTION: "frame_map.m"

```
%
% A - pixel values for image
% MAGIC - arbitrary value for calculating cutoff threshold (8 is good)
%

function M = frame_map (A,MAGIC)
D = 3;
[R,C] = size(A);
blacklines = [ A(:,D)' A(D,:) A(:,C-D)' A(R-D,:) ]';
mu = mean(blacklines);
sigma = std(blacklines);
black_threshold = mu + MAGIC*sigma;

% Black background:
%M = uint16( max( sign (A - black_threshold) , 0.0) * 65535);

% White background:
M = uint16(max ( sign (black_threshold - A), 0.0) * 65535);
```

FUNCTION: “writeimage.m”

```
function writeimage(exp,cframe,i,start_image)
% exp -> experiment number
% cframe -> processed image matrix to be written
% i -> frame number

if exp < 10
    expstr = ['00' num2str(exp)];
elseif exp < 100
    expstr = ['0' num2str(exp)];
elseif exp < 1000
    expstr = num2str(exp);
else
    fprintf('Error in experiment number');
end

if i==start_image
    mkdir(['cexp' expstr]);
end

location = ['cexp' expstr '\'];

if i < 10
    file = ['000' num2str(i) '.tif']
elseif i < 100
    file = ['00' num2str(i) '.tif']
elseif i < 1000
    file = ['0' num2str(i) '.tif']
else
    file = [num2str(i) '.tif']
end

imwrite(cframe,[location file]);
```

PART III: IMAGE BINARIZATION FUNCTIONS

MAIN FILE: "process_calcsubfill.m"

```
% ---------------- CONSTANTS --------------------
inc_frame = 18;
cutoff_freq = 200;

least_frame2 = 1800; %frame number threshold Pratio 2
least_frame3 = 2200; %frame number threshold Pratio 3
least_frame4 = 2600; %frame number threshold Pratio 4

nonflammable2 = [1,2,3,7,31,32,33,39,40,61,62,63,68,69,70];
nonflammable3 = [11,12,13,14,41,42,44,45,71,72,74,75,103,113];
nonflammable4 =
[21,22,23,24,25,26,27,51,52,53,54,55,57,81,82,83,84,85,86,87,88,104,110,111,1
18];

flammable2 = [4,5,6,8,9,10,34,35,36,37,38,64,65,66,67];
flammable3 =
[15,16,17,18,19,20,43,46,47,48,49,50,73,76,77,78,79,80,101,102,107,108,109,11
4,115];
flammable4 = [28,29,30,56,58,59,60,89,90,105,106,112,116,117];

% -----------------------------------------------

exp(1:200,2,1:118) = 0;
cexp(1:200,2,1:118) = 0;

% Calculate area curves
for i = 1 : 95
    temp = calcsubfill(i);
    l_temp = length(temp);
    exp(1:l_temp,1:2,i) = temp(1:l_temp,1:2);
    i
end

for i = 101 : 118
    temp = calcsubfill(i);
    l_temp = length(temp);
    exp(1:l_temp,1:2,i) = temp(1:l_temp, 1:2);
    i
end

% Filter area curves to remove 120Hz noise
for i = 1 : 95
    exptemp = exp(:,:,i);
    filtemp = filterdata(exptemp,2,cutoff_freq);
    cexp(:,1,i) = exp(:,1,i);
    cexp(:,2,i) = filtemp;
end

for i = 101 : 118
```

```
    exptemp = exp(:,:,i);
    filtemp = filterdata(exptemp,2,cutoff_freq);
    cexp(:,1,i) = exp(:,1,i);
    cexp(:,2,i) = filtemp;
end

% Check that there are enough files to produce a good graph
index = 0;
for i = 1 : length(nonflammable2)
    if filenum(nonflammable2(i)) > least_frame2
        index = index + 1;
        i2(index) = nonflammable2(i);
    end
end

index = 0;
for i = 1 : length(nonflammable3)
    if filenum(nonflammable3(i)) > least_frame3
        index = index + 1;
        i3(index) = nonflammable3(i);
    end
end

index = 0;
for i = 1 : length(nonflammable4)
    if filenum(nonflammable4(i)) > least_frame4
        index = index + 1;
        i4(index) = nonflammable4(i);
    end
end

first = 0.0101;
inc = inc_frame/9302;
last = (199 * inc) + first;

% Calculate averages
ave2(1:200,1) = first:inc:last;
ave3(1:200,1) = first:inc:last;
ave4(1:200,1) = first:inc:last;
cave2(1:200,1) = first:inc:last;
cave3(1:200,1) = first:inc:last;
cave4(1:200,1) = first:inc:last;

ave2(1:200,2) = 0;
ave3(1:200,2) = 0;
ave4(1:200,2) = 0;
cave2(1:200,2) = 0;
cave3(1:200,2) = 0;
cave4(1:200,2) = 0;


for i = 1:length(i2);
    ave2(:,2) = ave2(:,2) + exp(:,2,i2(i))/length(i2);
    cave2(:,2) = cave2(:,2) + cexp(:,2,i2(i))/length(i2);
end
```

```
figure(1);
plot(ave2(:,1), ave2(:,2)); hold on
plot(cave2(:,1), cave2(:,2)); hold on

for i = 1:length(i3);
    ave3(:,2) = ave3(:,2) + exp(:,2,i3(i))/length(i3);
    cave3(:,2) = cave3(:,2) + cexp(:,2,i3(i))/length(i3);
end
%figure;
plot(ave3(:,1), ave3(:,2), 'r'); hold on
plot(cave3(:,1), cave3(:,2), 'r'); hold on

for i = 1:length(i4);
    ave4(:,2) = ave4(:,2) + exp(:,2,i4(i))/length(i4);
    cave4(:,2) = cave4(:,2) + cexp(:,2,i4(i))/length(i4);
end
%figure;
plot(ave4(:,1), ave4(:,2), 'g');
plot(cave4(:,1), cave4(:,2), 'g');
```

FUNCTION: “calcsubfill.m”

```
function data = calcsubfill(exp)

% ----------- Constants -----------
first_frame = 94; %(10 ms equivalent)
inc_frame = 18; %(2 ms equivalent)
bk_ave_first_image = 56;
bk_ave_last_image = 80;
% ---------------------------------

no_files = filenum(exp);

index = 0;

bk=loadcimages(exp, bk_ave_first_image, bk_ave_last_image);
bk_ave=bkground(bk, (bk_ave_last_image - bk_ave_first_image));
clear bk;

for frame_no = first_frame : inc_frame : no_files

    index = index + 1;

    im = subfill(exp, frame_no, bk_ave);

    data(index,1) = frame_no / 9302;

    data(index,2) = 0; % col 1 = time, col 2 = area.
    for j = 1 : 480
        for i = 1 : 480
            if im(i,j,1) == 0
                data(index,2) = data(index,2) + 1;
            end
        end
    end
end
```

FUNCTION: "subfill.m"

```
function fillim = subfill(exp, im_no, bk_ave)

% ------------Constants-------------
thresh = 7000;
bk_ave_first_image = 56;
bk_ave_last_image = 80;

% ---------------------------------

if bk_ave == 0
    bk=loadcimages(exp, bk_ave_first_image, bk_ave_last_image);
    bk_ave=bkground(bk, (bk_ave_last_image - bk_ave_first_image));
    clear bk;
end

frame = loadcimage(exp, im_no);
image = (frame - bk_ave) + (bk_ave - frame);
fillim(1:480,1:480,1) = image;

for i = 1 : 480
    for j = 1 : 480
        if image(i,j) > thresh
            fillim(i,j,1) = 0;
        else
            fillim(i,j,1) = 65535;
        end
    end
end

fillim(1:480,1:480,2) = image(1:480,1:480);

%Set time pixels:
fillim(461:476,6:97,1) = frame(461:476,6:97) + 40000;
fillim(461:476,6:97,2) = frame(461:476,6:97);
```

APPENDIX E: COMPRESSIBLE FLOW CALCULATIONS

The PSC capillary tube, which is connected downstream of the 1/4" fitting at the solenoid exit (**Figure 8**) has an internal diameter of 0.47 mm. It is assumed to be a constant area duct, connected at each end to a reservoir at constant temperature and pressure, as shown in the simplified diagram below:

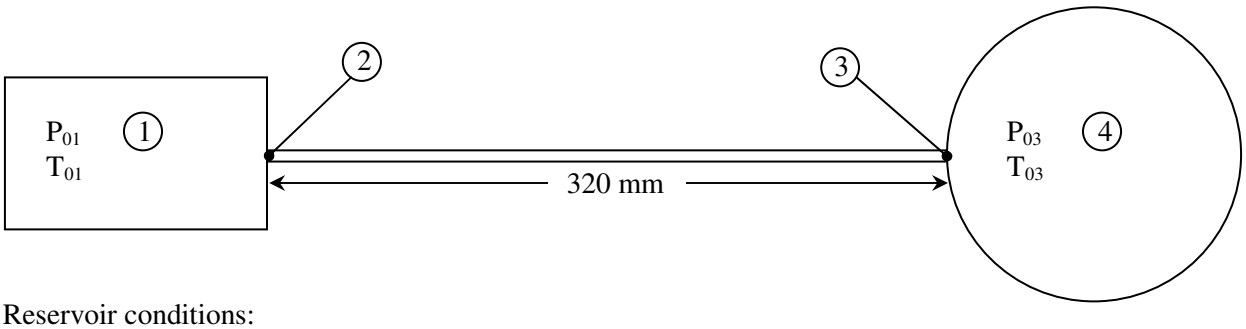

Reservoir conditions:

T_{01} = 288.15 K

P_{01} = 200 psi (1.38E6 Pa) @ P_{RATIO} 2, 300 psi (2.07E6 Pa) @ P_{RATIO} 3, 400 psi (2.76E6 Pa) @ P_{RATIO} 4

P_4 = 100 psi (689475.7 Pa)

Governing equations [Shapiro]:

$$\frac{\bar{f}L^*}{D} = \frac{1 - Ma_2^2}{k\,Ma_2^2} + \frac{k+1}{2\,k}\,ln\frac{(k+1)\,Ma_2^2}{2 + (k-1)\,Ma_2^2} \quad \text{(Eq. E.1)}$$

$$\frac{1}{\sqrt{f}} = -1.8\,log10\left[\left(\frac{\varepsilon/D}{3.7}\right)^{1.11} + \frac{6.9}{Re}\right] \quad \text{(Eq. E.2)}$$

$$Ma = v/a \quad \text{(Eq. E.3)}$$

$$a = \sqrt{kRT} \quad \text{(Eq. E.4)}$$

$$Re = \frac{\rho v D}{\mu} \quad \text{(Eq. E.5)}$$

Where $\bar{f}$ is the length mean coefficient of friction, $\mathbf{L}^*$ is the critical tube length required for a sonic exit condition, **D** is the internal diameter of the capillary tube, **a** is the local speed of sound and **Ma** is the local Mach number. The Reynolds number (**Re**) was determined based on average properties in the tube.

The following gas properties were used for the calculations:

k (ratio of specific heats, natural gas) = 1.31

R_{NG} (gas constant, natural gas) = 518 $m^2/(s^2K)$

μ_{NG} (dynamic viscosity, natural gas) = 1.34E-5 Ns/m^2

The following dimensions were used for the capillary tube:

L (length) = 320 mm

D (inner diameter) = 0.47 mm

ε (surface roughness) = 1.5E-6 m

Method of analysis for determination of critical tube length (L^*):

1) The flow between point (1) and (2) is assumed isentropic, as suggested by Shapiro
2) Initially, the flow is assumed to be choked at the exit (3), thus assume $L = L^*$
3) An initial velocity is guessed at point (2) → ex: 100 m/s
4) The Mach number, Reynolds number and friction factor are calculated based on the guessed velocity
5) The ratio in the left hand side of Equation E.1 is calculated based on the tube diameter, roughness and calculated friction factor
6) The ratio on the right hand side of equation E.1 is calculated based on the ratio of specific heats and calculated Mach number
7) The answers from steps 5 and 6 are compared and a percent difference value is calculated
8) Steps 4 to 7 are looped, until the percent difference value is smaller than 0.01%
9) Once the iteration loop converges, the calculated Mach number is used in Equations E.6 → E.9 to give the static and stagnation pressures at the capillary tube entrance (2) and exit (3)
10) At the sonic exit condition, where the length of the tube (L) is exactly equal to the critical length (L^*) the pressure at the tube exit (P_3) must equal the back pressure in the discharge reservoir (P_4). Thus, the left hand side of Equation E.10 equals 1. The ratios of P_{01} to P_4 and P_3 to P_{03} are calculated based on the values found from step 9. This gives a numerical value to the ratio of P_{03} to P_{01}

11) The ratio of P_{03} to P_{01} from step 10 is used in the Fanno Line Equation (E.10) to calculate the new Mach number which satisfies the equation
12) Finally, the Mach number calculated from step 11 is used in Equation E.1 to determine the value of the critical pipe length (L^*)

$$P_2 = \frac{P_{01}}{[1 + 0.5(k-1)Ma_2^2]^{\frac{k}{k-1}}} \quad \text{(Eq. E.6)}$$

$$P_{02} = P_2[1 + 0.5(k-1)Ma_2^2] \quad \text{(Eq. E.7)}$$

$$P_3 = \frac{P_2}{\frac{1}{Ma_2}\sqrt{\frac{k+1}{2+(k-1)Ma_2^2}}} \quad \text{(Eq. E.8)}$$

$$P_{03} = \frac{P_{02}}{\frac{1}{Ma_2}\sqrt{\left[\frac{2+(k-1)Ma_2^2}{k+1}\right]^{\frac{k+1}{k-1}}}} \quad \text{(Eq. E.9)}$$

Fanno Line Equation: $$\frac{P_{03}}{P_{01}} = \left(\frac{k+1}{2}\right)^{\frac{k+1}{2(k-1)}} \frac{Ma_2}{\left(1+\frac{k-1}{2}Ma_2^2\right)^{\frac{k+1}{2(k-1)}}} \quad \text{(Eq. E.10)}$$

Identity Equation: $$\frac{P_3}{P_4} = \frac{P_{01}}{P_4}\frac{P_{03}}{P_{01}}\frac{P_3}{P_{03}} \quad \text{(Eq. E.11)}$$

Steps 1 → 12 are repeated for each pressure ratio to give the following critical length values:

$P_{RATIO} = 2 \rightarrow L^* = 15.4$ mm

$P_{RATIO} = 3 \rightarrow L^* = 70.7$ mm

$P_{RATIO} = 4 \rightarrow L^* = 152.7$ mm

If the actual tube length (320mm) is longer than the critical tube length, the flow will be unchoked and remain subsonic all though the tube. Also, the tube exit pressure will be equal to the combustion bomb pressure. As demonstrated by the L^* values, the flow remains unchoked at all pressure ratios.